

**A STUDY OF OCEANIC RESPONSES  
TO MESOSCALE PROCESSES  
IN THE MIDDLE ATLANTIC BIGHT**

by

Jin Sha

A dissertation submitted to the Faculty of the University of Delaware in  
partial fulfillment of the requirements for the degree of Doctor of Philosophy  
in Oceanography

Fall 2015

© 2015 Jin Sha  
All Rights Reserved

ProQuest Number: 10014755

All rights reserved

INFORMATION TO ALL USERS

The quality of this reproduction is dependent upon the quality of the copy submitted.

In the unlikely event that the author did not send a complete manuscript and there are missing pages, these will be noted. Also, if material had to be removed, a note will indicate the deletion.



ProQuest 10014755

Published by ProQuest LLC (2016). Copyright of the Dissertation is held by the Author.

All rights reserved.

This work is protected against unauthorized copying under Title 17, United States Code  
Microform Edition © ProQuest LLC.

ProQuest LLC.  
789 East Eisenhower Parkway  
P.O. Box 1346  
Ann Arbor, MI 48106 - 1346

**A STUDY OF OCEANIC RESPONSES  
TO MESOSCALE PROCESSES  
IN THE MIDDLE ATLANTIC BIGHT**

by

Jin Sha

Approved: \_\_\_\_\_  
Mark A. Moline, Ph.D.  
Director of the School of Marine Science and Policy

Approved: \_\_\_\_\_  
Mohsen Badiey, Ph.D.  
Acting Dean of the College of Earth, Ocean, and Environment

Approved: \_\_\_\_\_  
Ann L. Ardis, Ph.D.  
Interim Vice Provost for Graduate and Professional Education

I certify that I have read this dissertation and that in my opinion it meets the academic and professional standard required by the University as a dissertation for the degree of Doctor of Philosophy.

Signed:

---

Xiao-Hai Yan, Ph.D.  
Professor in charge of dissertation

I certify that I have read this dissertation and that in my opinion it meets the academic and professional standard required by the University as a dissertation for the degree of Doctor of Philosophy.

Signed:

---

Young-Heon Jo, Ph.D.  
Member of dissertation committee

I certify that I have read this dissertation and that in my opinion it meets the academic and professional standard required by the University as a dissertation for the degree of Doctor of Philosophy.

Signed:

---

I. Pablo Huq, Ph.D.  
Member of dissertation committee

I certify that I have read this dissertation and that in my opinion it meets the academic and professional standard required by the University as a dissertation for the degree of Doctor of Philosophy.

Signed:

---

Ruoying HE, Ph.D.  
Member of dissertation committee

## ACKNOWLEDGMENTS

First and foremost I would like to thank my advisor, Dr. Xiao-Hai Yan for his support and guidance, leading me into the world of physical oceanography from an electrical engineer. So many times I became frustrated and it is my advisor that keeps on encouraging me to overcome the difficulties. I am very grateful to have worked with such a nice scientist and person.

Then I would sincerely thank Dr. Young-Heon Jo for his creative input, patience and encouragement. He helps me so much during my Ph.D. study in U.S. I also thank my whole committee including Dr. Ruoying He and Dr. Pablo Huq for helpful input, suggestions and sharing their knowledge and time. I also would like to thank Dr. Matthew Oliver and Dr. Josh Kohut for their support and patience in the revision process that I benefitted a lot in paper writing.

My colleagues in the 215 Robinson Hall helped me a lot, and they deserve special recognition: Feili, Weiwei, Xiangbai, Dr. Jiang, Wenfang, Enhui, and Autumn, as well as those in our college including Lin and Dong. I would like to thank all my friends in UD, particularly Yangang, Xuesong, Zheguang, Yunyun and Xinhui, for those happy memories in my life. Also special thanks to my roommates during those 2B days: Qingyang and Changgen.

Last, but not least, I would like to thank my parents and sister for their continuous support and encouragement through all of these years. Thanks to the financial support from the Chinese Scholarship Council and the NOAA Sea Grant.

*This work is dedicated to my family and friends who are always there for me.*

## TABLE OF CONTENTS

LIST OF TABLES .....	ix
LIST OF FIGURES .....	x
ABSTRACT .....	xv

### Chapter

1	INTRODUCTION .....	1
1.1	Background of the Middle Atlantic Bight .....	1
1.2	Inner Shelf: Phytoplankton Blooms .....	3
1.3	Mid- and Outer Shelf: the Cold Pool .....	5
1.4	MAB Ocean Heat Content .....	5
1.5	Dissertation Outline .....	7
2	A CASE STUDY OF LARGE PHYTOPLANKTON BLOOMS OFF THE NEW JERSEY COAST .....	9
2.1	Introduction .....	9
2.2	Data and Methods .....	10
2.2.1	Data .....	10
2.2.2	Bloom Area Identification .....	12
2.2.3	Simulation of the Bloom Advection .....	12
2.2.4	Simulated Centroid Trajectories under Ekman Drift .....	14
2.3	Horizontal Bloom Transport .....	14
2.3.1	Bloom Distribution Diagnostics .....	14
2.3.2	Bloom Advection Simulation .....	16
2.3.3	Roles of the Wind in the Horizontal Advection .....	17
2.4	Nutrient Delivery Mechanisms .....	18
2.4.1	Area A: Upwelling and the Eddy at the Estuary .....	18
2.4.2	Area B: Coastal Upwelling .....	20
2.4.3	Area C: Wind Stress Curl and Ekman Pumping .....	21
2.4.4	Long Time Perspective .....	22

2.5	Discussion.....	24
3	THE MODULATION OF THE SEASONAL CROSS-SHELF SEA LEVEL VARIATION BY THE COLD POOL IN THE MIDDLE ATLANTIC BIGHT .....	41
3.1	Introduction .....	41
3.2	Data and Methods.....	42
3.2.1	Data.....	42
3.2.2	Cross-shelf Transect and Harmonic Fitting.....	43
3.2.3	Ensemble Empirical Mode Decomposition.....	45
3.2.4	Steric Height Estimation.....	45
3.3	Temperature and Salinity Annual Cycles.....	48
3.4	Derived Steric Components.....	49
3.5	EEMD and the Application .....	51
3.6	Discussion.....	52
4	THE HORIZONTAL HEAT ADVECTION IN THE MIDDLE ATLANTIC BIGHT AND THE INTERACTIONS AMONG DIFFERENT TIME SCALES .....	70
4.1	Introduction .....	70
4.2	Data and Method .....	71
4.2.1	Data.....	71
4.2.2	Estimation of the Mixed Mayer Depth .....	73
4.2.3	Estimation of the Shelf Currents .....	74
4.2.4	Estimation of the Upper Ocean Heat Budget .....	75
4.2.5	Fast Multi-Dimensional Ensemble Empirical Mode Decomposition (FMEEMD).....	76
4.2.6	Temporal Decomposition of the Horizontal Heat Advection.....	76
4.3	The Role of the Horizontal Heat Advection in the Heat Budget.....	78
4.4	Components of the Horizontal Heat Advection .....	80
4.5	Temporal Components of the Heat Advection .....	81
4.6	Discussion.....	82
5	CONCLUSIONS .....	101
5.1	Mechanisms of the Phytoplankton Blooms.....	101
5.2	The Linkage between the Cross-Shelf Sea Level Variation and the Cold Pool.....	102

5.3 The Role and the Response of the Horizontal Heat Advection.....	103
REFERENCES .....	105
Appendixes .....	116
A PERMISSIONS FROM JOURNAL OF GEOPHYSICAL RESEARCH: OCEANS .....	116
B PERMISSIONS FROM CONTINENTAL SHELF RESEARCH .....	118

## LIST OF TABLES

- Table 4.1. The temporal decomposition of the horizontal heat advection associated with the surface geostrophic current. The percentages present the contribution of each component to the total energy. .... 99
- Table 4.2. The temporal decomposition of the horizontal heat advection associated with wind-induced Ekman currents. The percentages present the contribution of each component to the total energy. .... 100

## LIST OF FIGURES

- Figure 2.1. True color image of MODIS on Aug 17th. The bloom is divided into three subareas A, B and C, shown as white rectangle in the figure. Rectangle D is the area over which Chl are averaged in the long term time series comparison. ....28
- Figure 2.2. The bloom detection (using the Chl data on August 17, 2011). Black line: Detected bloom area varying with threshold P. Red line: the gradient of detected bloom area varying with P.....29
- Figure 2.3. Magnitude diagnostics of the bloom evolution processes. The results are averaged over the whole study area during August of 2011 (excluding the hurricane period). Corresponding to the four terms in Equation 3, LT (red) is the magnitude of the local temporal variation of Chl, HADV (black) is the horizontal advection, HDIF (blue) is the horizontal diffusion/mixing, and R (green) is the residual term.....30
- Figure 2.4. Advection simulation. (a) initial distribution observed by MODIS on Aug 12th, 2011; (b) final distribution observed by MODIS on Aug 17th; (c) advection simulation using sea surface current from HF radar measurements. Red points: initial positions; Green points: simulated bloom distribution pattern after 5 day derivation; (d) mean HF velocities from Aug 1st to Aug 24th.....31
- Figure 2.5. The role of the wind. (a) Correlation coefficient ( $p < 0.05$ ) between the magnitudes of sea surface current from HF radar and the magnitudes of sea surface wind stress. All areas with  $p > 0.05$  were set to be zero. (b) Comparison between the centroid trajectory and the simulated trajectory from current induced by wind. Black lines show observed trajectories from Aug 10th to Aug 23rd. Red lines represent the simulated trajectories during the same period. The dashed lines are calculated within the total study region, while solid lines are calculated only in the Area B.....32
- Figure 2.6. Chl over Area A. (a) Black lines are the transect location along the coast. The background image is the Chl data on Aug 17th. (b) Chl varies over time from only one transect (the second from coast). The black arrow is showing the low Chl water transporting south. (c) Chl time

	series averaged along one transect (the second one from the coast) within Area A. ....	33
Figure 2.7.	The condition comparison between 2011/08/06 and 2011/08/11. From top to bottom are the wind current from buoy station at Sandy Hook, daily averaged sea surface currents measured by HF radar, SST from G1SST/JPL, Chl from MODIS/Aqua. Left column (a to d) August 6th. Right column (e to h) August 11th. ....	35
Figure 2.8.	The freshwater discharge of Hudson River measured at Green Island, NY. The solid, dashed and dotted black lines represent the daily measurement, mean discharge record over 10 year and mean discharge record over 46 year. ....	36
Figure 2.9.	(a) Glider (RU16-221) locations. From Aug 10th to Aug 16th, the glider moves within Area A. From Aug 16th to Aug 23rd the glider is moving within Area B. (b) Salinity profile from the glider measurement. (c) Temperature profile from the glider measurement. (d) SST measured by AVHRR on Aug 12th of 2011 as a simultaneous compliant data, showing the surface temperature distribution along the coast of New Jersey. ....	37
Figure 2.10.	The offshore transport estimated from along shore wind component of Buoy data (Atlantic City). ....	38
Figure 2.11.	(a) Ekman pumping (anomaly) derived from the wind stress curl anomaly and averaged from Aug 13th to Aug 17th. Positive areas represent the location where upwelling occurs. (b) Sea surface temperature anomaly (SSTA) averaged from Aug 13th to 17th. Area I and Area II are showing cold water pattern corresponding to the pumping area in (a). ....	39
Figure 2.12.	Multi-year scale Chl time series. (a) Black: area-averaged 4km chlorophyll a concentration in the New Jersey coast; Red: time series of detected bloom spatial coverage. (b) Chl condition for each sub-region detected from the year 2002 to 2014. Red, blue and black lines represent the detected bloom area within each sub-region. The dashed lines represent the threshold (1.6 times of the median value) for each sub-region. ....	40
Figure 3.1.	Cold pool spatial distribution. A. the scattered bottom temperatures from CTD and PFL profiles from May to September during 1993~2012. The black line in the grey rectangle is the cross-shelf transect, averaging over the shadowed rectangle. B. the contour of the bottom temperatures	

	on the shelf indicating the location of the cold pool (with temperature <math><10^{\circ}\text{C}</math>). .....	56
Figure 3.2.	Temperature from harmonic fitting versus measured temperature at different offshore distance (0-120 km). Shown in each panel is the root-mean-square error (RMSE) and the correlation coefficients with $p<0.05$ . .....	57
Figure 3.3.	Temperature annual cycles along the transect. A. cross-section view of temperature (contour) in different months. B. temperature annual cycles at three locations: middle shelf surface (offshore distance = 60km, depth = 10m), middle shelf bottom (offshore distance=60km, depth = 50m), and outer shelf bottom (offshore distance =120km, depth = 50m). C. surface layer temperature annual evolution. D. Bottom temperature annual evolution. ....	60
Figure 3.4.	Salinity annual cycles along the transect. A. cross-section view of salinity in different months. B. salinity annual cycles at three locations: middle shelf surface (offshore distance = 100km, depth = 10m), middle shelf bottom (offshore distance=100km, depth = 50m), and outer shelf bottom (offshore distance =160km, depth = 50m). C. surface layer salinity annual evolution. D. bottom salinity annual evolution.....	63
Figure 3.5.	Annual evolution (contour) of different steric components and the monthly climatological altimetry SLA. From left to right: A. thermal steric height, B. haline steric height, C. total steric height and D. averaged altimetry SLA. The total steric height is the sum of thermal and haline steric components. The black rectangles in A, C and D are the central depressed pattern co-locating with the cold pool. ....	64
Figure 3.6.	The comparison between the thermal steric height (red stars) and haline steric height (black stars) annual cycle.....	65
Figure 3.7.	Derived thermal steric height versus altimetry SLA. The black line indicates the linear fitting. ....	66
Figure 3.8.	Comparison of altimetry SLA (A) and the seasonal components using EEMD (B) in 2010. ....	67
Figure 3.9.	The location comparison in the offshore direction. The red dots are the locations of altimetry SLA depression, and the black dots are the locations of the cold core identified from in-situ measurements. ....	68

Figure 3.10.	Comparison between the bottom temperature, corrected thermal steric height and altimeter SLA in August. The red line is the bottom temperature, black line is the derived thermal steric height, and the blue line is the SLA from altimeter. The error bar for each curve denotes the standard error of the mean. ....	69
Figure 4.1.	The heat budget in the Middle Atlantic Bight averaged over the mixed layer. ....	87
Figure 4.2.	The histogram of the correlation coefficients. A. the correlation coefficients between the temporal variation term and the advection term. B. The correlation coefficients between the temporal variation term and the residual term. Non-significant correlations ( $p>0.05$ ) are removed. ....	88
Figure 4.3.	Each component of the advection term. The red line is the advection corresponding to the sea surface slope (slope advection). The blue line is the advection corresponding to the subsurface density gradient (Shear Advection). The black line is the advection due to wind-driven Ekman transport (Ekman Advection). The abnormal values of Ekman Advection, which are larger than 2 standard deviation, have been removed. ....	89
Figure 4.4.	Comparison of the contribution in the upper ocean heat budget between the geostrophic currents and Ekman transport. A. the correlation coefficients between the composed advection and the slope advection. B. the correlation coefficients between the composed advection and the shear advection. C. the correlation coefficients between the composed advection and the Ekman advection. Those areas without significant correlation ( $p>0.05$ ) are masked out in the figures.....	92
Figure 4.5.	Comparison of the 16 (out of 25) advection temporal components. The blue lines are time series of the advection component (domain averaged). The red line is the sum of the components, computed using SST and absolute geostrophic currents. Components involving sub-seasonal and higher frequencies are not shown here.....	93
Figure 4.6.	The domain-averaged spectral distribution of the SST (A), surface geostrophic current speed (B) and depth-averaged Ekman current speed (C). The green area represents the 95% confidence level of the mean. The mean of each variable has been removed.....	95
Figure 4.7.	The spectral distribution of the advection. A. The advection from seasonal SST and seasonal surface geostrophic currents. B. The	

advection from seasonal SST and seasonal Ekman currents. The red line is the spatial mean averaging over the study area. The green area represents the 95% confidence level of the mean. ....97

Figure 4.8. Cross-comparison of the temporal heat variation with different choice of MLD and MLT. The mixed layers are insitu monthly climatological MLD, SODA time-varying MLD and SODA monthly climatological MLD respectively. The MLTs are SST and SODA. Note this is the vertical mean thus the unit is °C/s. ....98

## **ABSTRACT**

The responses of the ocean to several mesoscale processes in the Middle Atlantic Bight (MAB), including the phytoplankton blooms, the cold pool and the horizontal heat advection, are investigated on different time scales using multi-sensor data including in-situ measurements, satellite observations and reanalysis data.

Taking the 2011 summer bloom as a study case, we investigated the transport and nutrient delivery mechanisms are investigated for large phytoplankton blooms of the New Jersey coast. The horizontal advection of the chlorophyll is approximately one order larger than the horizontal diffusion averaging the whole study area. And the sea surface currents are found to correlate with the wind stress but only for part of the middle shelf. Based on the horizontal advection simulation driven by HF radar current, the bloom is divided into three sub-regions. The northern coastal section of the bloom shows high-low-high pattern in chlorophyll time series, which is related to coastal upwelling and an anticyclonic eddy. Coastal currents play an important role in the eddy formation and the southward transport of the bloom. The southern coastal section of the bloom is supported by the nutrients from coastal upwelling and driven offshore by wind. The northeast section of the bloom is fueled by nutrient source upwelled through Ekman pumping. The magnitude of Ekman pumping is of the same order as the magnitude of the upwelling along the coast. These identified mechanisms could also be applied to more than half of bloom events during 2002 to 2013. In the summer of 2011 off the coast of New Jersey, processes in different sub-regions worked together, leading to this large phytoplankton bloom.

The influence of the cold pool in the Middle Atlantic Bight (MAB) to cross-shelf sea surface slope is explored by fitting an annual harmonic to temperature and salinity profiles from 1993 to 2012, and comparing to the 20-year-averaged altimetry sea level anomaly (SLA). The consistency within bottom temperature, thermal steric height, total steric height and altimetry observation validates that the cold pool induces depressed sea level in the middle shelf overlapping with the dominant surface seasonal cycles. Temporally, the cold pool pattern is most apparent in July and August as a result of magnitude competition between the thermal and haline steric height. In addition, Ensemble Empirical Mode Decomposition (EEMD) is employed to reconstruct the altimetry SLA and reveals the middle-shelf depression pattern from single year's SLA data. The locations of the SLA depression from 1993 to 2012 agree with the cold pool locations identified from in-situ measurements, suggesting a promising application of altimetry SLA in the cold pool study. Conclusively the modulation of the cross-shelf sea level variation by the cold pool is revealed, which contributes to the understanding of the sea level response to water masses on the continental shelf.

Continuous satellite observations from 1992 to 2012 allow to investigate the contribution of the horizontal heat flux to the upper layer heat budget on different time scales over the middle and outer shelf of MAB. On the seasonal scale, the shelf averaged temperature variations are controlled by the vertical heat flux. On longer time scales, the temporal temperature variations are determined by the competition between the vertical heat flux and the horizontal heat advection. The horizontal heat diffusion is relatively small comparing to other terms in the heat budget. In the upper mixed layer, the heat advection due to the sloping sea surface is comparable to the

magnitude of the wind-induced Ekman transport, each of which has different spatial distribution over the shelf. The interactions among different time scales (the sub-seasonal, seasonal, interannual, long-term scales and the mean) of the heat advection are quantitatively evaluated. For the advection related to the geostrophic currents, the largest components are the seasonal temperature by the mean currents, the mean temperature by the sub-seasonal currents, and the seasonal temperature by the sub-seasonal currents. They together contributing 80% to the total energy of the heat advection. For the advection associated with the Ekman currents, the largest components are the seasonal temperature by the mean Ekman currents, and the seasonal temperature by the seasonal Ekman currents. The relative magnitudes of temporal components are determined by the spectral distribution of the temperature and currents. Spectral analysis on the temporal components also suggests that the variations of the horizontal heat advection on specific time scales are contributed from multiply time scale variations.

Through the detailed investigations on the mesoscale processes in the MAB, including the chlorophyll concentrations, the sea level and the heat advectons, my work improves the understanding of the coastal ocean variations on different time scales, facilitates better interpretation of the observations, and clarifies the linkage among different variables. Moreover, climate change and the varying ocean are placing new challenges to coastal researchers. This dissertation enables further investigations of the coastal ocean responses to the climate change.

## Chapter 1

### INTRODUCTION

#### 1.1 Background of the Middle Atlantic Bight

Middle Atlantic Bight (MAB) refers to the continental shelf of the eastern coast of United States spanning from Cape Cod and Nantucket Shoals in the northeast to Cape Hatteras in the southwest (Beardsley and Boicourt, 1981). There have been extensive studies on hydrodynamics in this region. The mean flow on the continental shelf is equatorward from northeast to southwest approximately along the isobath, which is an extension of the coastal current originating from Scotian shelf or even southern coast of Greenland, and is primarily driven by the alongshore pressure gradient (ASPG) (Aikman III et al., 1988; Beardsley et al., 1985; Beardsley and Boicourt, 1981; Chapman et al., 1986; Chapman and Beardsley, 1989; Fairbanks, 1982; Lentz, 2008a). The seasonal variations of alongshelf current is southwest during winters and northeast during summers, which are due to wind stress and cross-shelf density gradient (Dong and Kelly, 2003; Lentz, 2008b). A recent study (Xu and Oey, 2011) revealed that the mean ASPG is due to rivers and Coastal Labrador Sea Water (CLSW) while the seasonal and interannual variations of ASPG are due to Gulf Stream's shift and warm-core rings north of Gulf Stream. The currents in the south MAB will veer offshore and be entrained by the Gulf Stream (Bane et al., 1988; Churchill and Gawarkiewicz, 2014).

Using isotope tracer methods the water masses on the continental shelf are identified (Chapman et al., 1986; Chapman and Beardsley, 1989; Fairbanks, 1982).

The upstream water from Gulf of Maine is a mixture of freshwater, Scotian shelf water and slope water. The alongshelf flow remains mostly on the shelf, consisting of about 70-80 percent Scotian Shelf water, as well as local river runoff and slope water. The freshwater from local rivers is limited within the near-shore and near-surface band in the Middle Atlantic Bight.

A shelfbreak front separates the cooler, fresher shelf water from the warmer saltier slope water, associated with an alongshelf shelfbreak jet (Beardsley et al., 1985; Burrage and Garvine, 1988; He et al., 2011a; Houghton and Visbeck, 1998; Marra et al., 1990). The slope water is originated from “Slope Sea”, which is a narrow band between Gulf Stream and the Continental shelf from Cape Hatteras to the Grand Banks [Csanady and Hamilton, 1988] with features of: inflow of Coastal Labrador Sea Water across the Grand Banks, closed cyclonic gyre in the western slope sea. Though the cross-shelf mixing of slope water is relatively weak compared with downstream advection (Chapman et al., 1986), the intrusions of the water from slope water can still be observed at the intermediate depth termed as salinity maximum layer (Fairbanks, 1982; Gordon and Aikman III, 1981; Lentz, 2003).

There are numerous processes occurring in the MAB. In the inner shelf, there are freshwater plumes from coastal rivers, phytoplankton blooms associated with coastal upwelling. In the bottom of the mid- and outer shelf, the cold pool is one of important processes persisting every summer. For the upper layer of the mid- and outer shelf, variations of the water temperature are subject to seasonal and interannual variabilities. To better understand the response of the ocean, i.e., variation of oceanic variables, to different processes, several mesoscale processes, with spatial scales of 50km to 500km, are chosen and the detailed mechanisms are investigated.

## **1.2 Inner Shelf: Phytoplankton Blooms**

Large phytoplankton blooms off the coast of New Jersey could affect public human health, coastal ecosystems, and commercial fisheries (Hoagland and Scatista, 2006). The organic matter generated from the phytoplankton bloom could sink below the pycnocline, and result in oxygen depletion over the seafloor (Glenn et al., 2004; Stoddard et al., 1986). Regions of episodic recurrent hypoxia, associated with the decomposition of phytoplankton bloom, are documented along the shelf (Warsh, 1987). The 1976 oxygen depletion event in the New York Bight from decomposition of algae resulted in around \$569 million losses for commercial fisheries (Figley et al., 1976). A brown tide in Long Island between 1985 and 1986 caused mass mortality of the bay scallop (Bricelj and Kuenster, 1989). It is essential to understand the physical mechanisms related to the development of such large phytoplankton blooms in this region.

Many studies documented phytoplankton blooms occurred in the productive Middle Atlantic Bight during fall to winter and early spring (Ryan et al., 1999; Xu et al., 2011; Yoder et al., 2002). Several factors could contribute to the development of large blooms in this region. Along the southern New Jersey coast, upwelling events due to northeastward along shore wind were observed (Clemente-Colon and Yan, 1999; Jiang et al., 2010; Song et al., 2001; Yankovsky and Garvine, 1998), and were linked to the phytoplankton growth (Glenn et al., 2004) and community structure (Moline et al., 2004). These upwelling centers were also found to co-locate with recurrent hypoxia regions along the coast (Glenn et al., 1996).

For the northern New Jersey coast, the Hudson River (HR) are related to the forming of coastal phytoplankton blooms. The HR estuary is the most heavily nutrient loaded estuary in the world (Howarth and Levinton, 2006), and is potentially capable

of driving high phytoplankton growth rates (Cole and Caraco, 2006). Subjected to local winds, the HR discharge could form surface-advected river plumes (Yankovsky and Chapman, 1997). Depending on these local winds the fresh water flows into a coastal current moving south along the New Jersey coast (typically under downwelling wind) or a recirculation eddy just south of the river mouth (more commonly driven by upwelling wind) (R. J. Chant et al., 2008; Choi and Wilkin, 2007; Lentz, 2004; Zhang et al., 2010). The recirculation eddies are linked to large phytoplankton blooms formed over the New York Bight (Frazer et al., 2006; Moline et al., 2008; Schofield et al., 2013).

Moreover, the influences of stratification and wind forcing have been long studied in this region. The stratification results from warmer sea surface temperatures and increased freshwater runoff from March, and erodes during fall and winter, which is regulating the annual productivity (Castelao et al., 2010; Schofield et al., 2008). During the stratified season, nutrients in the euphotic zone are depleted by phytoplankton populations confined to the upper mixed layer, which explains less common blooms in the summer. Wind forcing, together with stratification, could play an important role in the offshore transport over the shelf (Chant et al., 2004; Dzwonkowski, 2009; Jiang et al., 2010; Kohut et al., 2004; Lentz, 2001). Despite of these studies focusing on different factors separately, the detailed roles of these mechanisms during the large phytoplankton blooms, and how they couples with each other, are still need to be further explored and identified. Such study can serve as a baseline for future prediction and advance warning of potential harmful algae blooms, and will also benefit similar studies of large phytoplankton blooms in other regions.

### **1.3 Mid- and Outer Shelf: the Cold Pool**

The MAB cold pool refers to a cold bottom water mass ( $<10^{\circ}\text{C}$ ) located in the MAB, which is one of the primary water masses of this region (Fairbanks, 1982). The cold pool was firstly recorded as a cold belt extending from 30m to 80m isobath with varying temperature and spatial coverage year by year (Bigelow, 1933). The cold winter water persists at the bottom in spring, becomes increasingly isolated from the surface warm water in summer, and disappears during the fall (Houghton et al., 1982; Ketchum and Corwin, 1964). The cold pool locates on the middle and outer shelf, differing from tidal and wind mixing inshore water and the warmer saltier offshore slope water (Churchill and Gawarkiewicz, 2014; Fairbanks, 1982; Houghton et al., 1982). The location of the cold pool in the alongshore direction is related to the cross-shelf section width (Houghton et al., 1982). The cold pool is part of a longer equatorward alongshelf coastal current system originating from Greenland/Labrador shelf (Chapman et al., 1986; Chapman and Beardsley, 1989). The cold pool has biological influences on the population dynamics of the phytoplankton, fish juvenile abundance, and the distribution of MAB benthic and demersal biota (Malone et al., 1983; Narváez et al., 2014; Sullivan et al., 2005). The cold pool water enters into the southern MAB, shifts offshore entrained by the Gulf Stream, playing an important role in the chlorophyll transport along the shelf and the carbon budget of the North Atlantic (Bignami and Hopkins, 2003; Churchill and Gawarkiewicz, 2014; Wood et al., 1996).

### **1.4 MAB Ocean Heat Content**

Variations of the ocean heat content are gaining increased attention in the context of the global climate change (Chen and Tung, 2014; Levitus et al., 2012). Studies suggested that the roles of the surface heat flux and ocean heat transport,

which are the major factors associated with ocean heat content variation, may vary in different season (He and Weisberg, 2003, 2002), on different time scales (Gulev et al., 2013; Kushnir, 1994) and are subjected to regional differences (Dong and Kelly, 2004; Halliwell, 1998). Halliwell (1998) revealed that the decadal and short-term interdecadal variabilities of the sea surface temperature (SST) anomaly are driven by the atmospheric air-sea fluxes in the North Atlantic open ocean while the oceanic horizontal advection and the entrainment heat flux dominant in the Gulf Stream region.

In the Middle Atlantic Bight (MAB), numerous studies on the ocean heat content and the associated heat budget are carried on different time scales and the contributions from the horizontal heat advection are identified. The temporal mean surface heat flux is balanced by the along-isobath heat advection, while the cross-shelf heat advection is small relative to the along-shelf heat advection (Lentz, 2009). On the time scale of days to weeks the heat advection drives the temperature variability (Lentz et al., 2010). On the seasonal scale, the ocean heat content is dominated by the surface net heat flux (Beardsley et al., 2003; Lentz et al., 2010; Mountain et al., 1996). The interannual variability of the temperature is related to the local air-sea heat flux (Mountain, 2003) though over the Long Island Sound it is the horizontal heat advection controlling the temperature variability (Lee and Lwiza, 2005). Shearman and Lentz (2009) suggested that the long-term temperature variability along the U.S. east coast is controlled by the along shelf transport. Moreover, studies focusing on the inner shelf of MAB found that the cross-shelf heat flux associated with the upwelling circulation is dominant in the ocean heat budget on time scales of weeks to months (Austin, 1999; Fewings, 2007; Fewings and Lentz, 2011; Wilkin, 2006), while the

interannual variability of the wintertime cooling is partially influenced by the alongshore heat advection (Connolly and Lentz, 2014). Connolly and Lentz (2014) also revealed that the alongshelf heat advection can modify the seasonal and interannual variability of the surface heat flux.

## **1.5 Dissertation Outline**

The focus of this dissertation is the response of the ocean to mesoscale processes on different time scales, using multi-sensor observations including in-situ measurements and satellite observations as well as ocean reanalysis data.

In Chapter 2 a large phytoplankton bloom is taken as a study case to investigate the involved transport and nutrient supplying mechanisms in the inner shelf on a time scale of days to weeks. In Chapter 3 the relationship between the cross-shelf sea level variation and the cold pool is investigated on seasonal scale. In Chapter 4 the role of the horizontal heat advection in the upper layer heat budget is investigated and the response of the heat advection to variables on different time scales is evaluated.

The purpose of this dissertation is to improve our knowledge regarding on how oceanic variables, including the chlorophyll concentrations, sea level variations and ocean heat content, response to different processes on different time scales. My study in this dissertation consists of three articles. Chapter 2 is an article published in *Continental Shelf Research* (J. Sha, Y.-H. Jo, M. J. Oliver, J. Kohut, M. Shatley, W. T. Liu and X.-H. Yan, 2015: A case study of large phytoplankton blooms off the New Jersey coast with multi-sensor data). Chapter 3 is an article published (in Press) in *Journal of Geophysical Research – Oceans* (J. Sha, Y.-H. Jo, X.-H. Yan and W. T. Liu, 2015: The modulation of the seasonal cross-shelf sea level variation by the cold pool in the Middle Atlantic Bight). Chapter 4 is a manuscript in preparation (J. Sha

and X.-H. Yan: The horizontal heat advection in the Middle Atlantic Bight and the interactions among different time scales). Hereafter the term “we” is used as referring to all authors.

## **Chapter 2**

### **A CASE STUDY OF LARGE PHYTOPLANKTON BLOOMS OFF THE NEW JERSEY COAST**

#### **2.1 Introduction**

In the summer of 2011, there was a large phytoplankton bloom off the New Jersey coast (Figure 2.1). It was first observed through Moderate Resolution Imaging Spectroradiometer (MODIS) true color image at the end of July, lasting until the middle of September. This bloom occurs in the summer in contrast to the more common spring and fall blooms, and expanding far beyond the typical scale of summer time upwelling centers (Ryan et al., 1999; Schofield et al., 2008; Xu et al., 2011; Yoder et al., 2002).

Previous studies have focused on different mechanisms involved with the phytoplankton blooms separately. However, the detailed roles of these mechanisms during the large phytoplankton blooms, and how they couple with each other, still requires further investigation. The present study can serve as a baseline for future prediction and advance warning of potential harmful algae blooms, and will also benefit similar studies of large phytoplankton blooms in other regions.

Taking the 2011 summer bloom as a study case, we used multi-sensor data including both satellite and in-situ measurements to gain insight into the development of the bloom and clarify involved nutrient delivery and bloom transport mechanisms. While the bloom lasted for more than one month, we focused our study on in August, when the bloom expanded rapidly and significantly. Since hurricanes can also

influence the Chl in the ocean (Shi and Wang, 2011), we limited our study period before the passing of the Hurricane Irene at the end of August. Moreover, we put this 2011 case in the context of the decadal scale to investigate how the mechanisms proposed could apply to other blooms in this area. The chapter is organized as follows. First we investigated the role of horizontal advection in the bloom distribution as well as the role of the wind in the horizontal advection. Then based on the horizontal advection simulation, different transport and nutrient delivery mechanisms, in terms of physical processes, were proposed for each sub-region.

## **2.2 Data and Methods**

### **2.2.1 Data**

Daily Chl at 1km spatial resolution are retrieved from MODIS Terra/Aqua product from the real time satellite station of University of Delaware (UD) (see Acknowledgements for the access link) from July to August in 2011. In addition, monthly Chl data at 4km resolution are collected from the Ocean Color website from 2002 to 2013. The 1km data are used for the 2011 bloom case analysis and 4km data are used to for longer time series. Routinely land masking criteria were applied to eliminate the land area and we excluded Chl values larger than  $50\text{mg/m}^3$  and less than zero. Although the uncertainty of the satellite derived Chl product could be 60%~170% for coastal regions (C. Zhang et al., 2006), it is still valuable for this study since we focused mainly on the flow pattern of the bloom rather than absolute Chl values.

The blended sea winds, containing 6-hour ocean surface current vectors on a global  $0.25^\circ$  grid, were obtained from National Climatic Data Center (NCDC). Wind stress can be derived from wind velocity based on the bulk formula (Smith, 1988). The hourly buoy wind data at coastal buoy stations (Atlantic City Marina) were from National Data Buoy Center (NDBC), as a complementary wind source for the satellite wind field.

Sea surface currents can be measured by 4.55MHz long range High Frequency (HF) radar in a spatial resolution of 6 km and temporal resolution of 1 hour. HF currents during 2011 August were provided by the Middle Atlantic Regional Association Coastal Ocean Observation System (MARACOOS), a regional component of the Integrated Ocean Observing System (Roarty et al., 2010). The radial vectors were averaged and mapped on a regular grid every 3 hours (Dzwonkowski, 2009; Kohut et al., 2006).

Temperature and salinity profile (measurements of every 3 minutes) from Aug 10<sup>th</sup> to August 23<sup>rd</sup> were obtained from a glider (RU16-221) of Rutgers University deployed along the New Jersey coast on a water quality monitoring mission supported by the Environmental Protection Agency and the New Jersey Department of Environmental Protection. Sea surface temperature (SST) are the daily 1km G1SST product from the JPL ROMS (Regional Ocean Modeling System) group. River discharge time series were obtained from U.S. Geology Survey (USGS) database. In

this study we used the daily gauge measurements at Green Island, NY to analyze the discharge condition of the Hudson River.

### 2.2.2 Bloom Area Identification

The bloom detection method we employed was modified from Siegel et al. (2002) as

$$Bloom = (Chl_{data} - P \times Chl_{median}) > 0 \quad (2-1)$$

where  $Chl_{data}$  is daily Chl product,  $Chl_{median}$  is the annual median value at each specific location, and P is a non-dimensional constant threshold. Siegel et al. (2002) chose  $P=1.05$  to define the initial location of the bloom over the whole North Atlantic. However the threshold can vary for coastal ocean. We investigated the sensitivity of the detected bloom area to P (Figure 2.2 a and b). The sensitivity test were carried for all available Chl data in the August of 2011 with similar results, and only one day (August 17<sup>th</sup>) is shown in Figure 2.2. We found that the gradient of the detected bloom area is less sensitive if  $P \geq 1.6$ . Thus we chose  $P=1.6$  for this study. The increasing of the threshold is consistent with the increased primary production from Open Ocean to the coastal area. The relative robust constant threshold above  $P=1.6$  suggests the high enough Chl gradient separating the bloom area from the ambient water.

### 2.2.3 Simulation of the Bloom Advection

The advective component can be estimated by releasing simulated drifters within the HF radar sea surface current fields. Similar methods using simulated drifters were applied on frontal boundary development (Oliver et al., 2004) and transport studies (Dzwonkowski et al., 2010). In detail, we chose the satellite Chl on August 12<sup>th</sup> and August 17<sup>th</sup>, which are the best available data with the least cloud

coverage during the bloom fast expanding period, as our initial and final bloom location. The 1km Chl data were interpolated to match the 6km HF radar currents. Simulated drifters representing the bloom parcels were released every 6km following the resolution of HF radar data at locations the same as the initial bloom distribution. Each parcel followed a trajectory driven by sea surface currents over the course of five days at hourly time steps. A random-flight model [Ullman *et al.*, 2006] was applied to address the velocity uncertainty associated with sub-grid scale variability and measurement uncertainty. The random flight parameters are consistent with previous studies on the New Jersey shelf (Gong *et al.*, 2010; Kohut *et al.*, 2012). At each location for each time step, simulated drifters were released 1000 times. We use centroids to describe the mean movement during each time step,

$$\begin{aligned} X &= \sum_1^N x_i / N \\ Y &= \sum_1^N y_i / N \end{aligned} \quad (2-2)$$

where  $x_i$  and  $y_i$  are the derived final location within this time step, and  $N=1000$  is the number of released drifters during each time step at each location. The centroid was then used as initial location for the next time step. A fourth order Runge-Kutta method can solve the differential equation when calculating trajectories (Dzwonkowski, 2009).

The uncertainties in the drifter simulation were well documented (Ullman *et al.*, 2006). Kohut *et al.* (2006) noted that the radial uncertainty of HF radar currents is on the order of 5 cm/s. Kaplan and Largier (2006) pointed out there are no strong directionality for the difference between real and pseudo-drifters. The mean separation distance between simulated trajectories and actual drifters are 9km at 24h and 14km at 48h (Kohut *et al.*, 2012). Since the bloom length scale in our study exceeds 200km, it is still valuable enough to use this trajectory derivation. We limited our analysis on the simulated drifters to the qualitative level in order to minimize the impact of this

uncertainty, and will introduce other data to verify our analysis based on the advection derivation in later sections.

#### **2.2.4 Simulated Centroid Trajectories under Ekman Drift**

The above simulation with HF data estimates the movement of the bloom under all forcing. Concerning the role of the wind in the advection, trajectory simulations driven by wind only could be a simple way to study the direction of the bloom transport induced by wind. We used centroids calculated within the detected bloom boundary to apply the trajectory simulation. The simulated trajectory can be compared to the “observed centroid trajectory” from satellite Chl time series. Gong et al. (2010) shows the coherent wind-current correlation angle at mid to outer shelf during the summer is consistent with a shallow Ekman layer with separate boundary (surface and bottom) layers. Since the summer phytoplankton are confined within the upper layer (Schofield et al., 2008), it is necessary to consider the total volume movement rather than only surface velocity. Thus the current velocity used in the simulation is estimated by averaging Ekman transport  $(\tau_y/(\rho_{water}f), -\tau_x/(\rho_{water}f))$  over the surface Ekman layer (Ekman, 1905; Gill, 1968), where  $(\tau_x, \tau_y)$  is wind stress,  $\rho_{water}$  is water density, and  $f$  is Coriolis parameter ( $9.35 \times 10^5 \text{ s}^{-1}$  at  $40^\circ\text{N}$ ). The surface Ekman layer scale is  $\delta \sim \sqrt{2A/f} \approx 13 \text{ m}$  (for a constant eddy viscosity  $A = 0.01 \text{ m}^2\text{s}^{-1}$ ), the same order as the upper mixed layer depth determined from in-situ measurements.

### **2.3 Horizontal Bloom Transport**

#### **2.3.1 Bloom Distribution Diagnostics**

The evolution of the bloom distribution involves the processes of horizontal advection, horizontal diffusion, vertical advection, vertical diffusion, and local

biological processes (source/sink) related to phytoplankton growth, mortality, zooplankton grazing. etc. A simplified tracer equation can describe the evolution processes as

$$\partial C/\partial t + \bar{u} \cdot \nabla C = \lambda \nabla^2 C + R \quad (2-3)$$

where C is the chlorophyll concentration,  $\bar{u}$  is the flow field over the bloom area,  $\lambda$  is horizontal eddy diffusivity estimated as (Smagorinsky, 1963)

$$\lambda = \Delta x \Delta y \sqrt{(\partial u/\partial x)^2 + (\partial v/\partial y)^2 + \frac{1}{2}(\partial u/\partial x + \partial v/\partial y)^2} \quad (2-4)$$

where  $\Delta x, \Delta y$  are the horizontal length scale. The term  $\partial C/\partial t$  is the local temporal variation of Chl,  $\bar{u} \cdot \nabla C$  is the horizontal advection,  $\lambda \nabla^2 C$  is horizontal mixing. Due to the lack of vertical Chl profiles, we use the term R to denote the combined effects of biological source or sink, vertical advection, and vertical diffusion. The magnitudes of each term in Equation 2-3 can be estimated based on daily Chl time series (using linear interpolation for gap days) and HF currents. Figure 2.3 shows the comparison of the estimated magnitude averaged over our study area (  $333km \times 298km$  ). Similar diagnostics were also carried out for each sub region and were showing consistent patterns. The horizontal advection is much larger than the diffusion term (i.e., large Peclet number). The local temporal variation is also small while steadily increasing. This suggests the importance of the advection in the horizontal distribution of the bloom, which is consistent with previous literature results (Abraham, 1998; Bracco et al., 2009) that horizontal advection is the dominant processes in generating the observed distributions of planktonic tracers at scales of few hundreds of kilometers or larger. The diagnostic result will be further discussed in Section 2.5.

### 2.3.2 Bloom Advection Simulation

The detailed bloom horizontal evolution could be further simulated with the sea surface currents as explained in the method section. These results were then used to interpret the satellite time series to separate out the local processes. Figure 2.4. is the advection of simulated drifters from August 12<sup>th</sup> and August 17<sup>th</sup>. Although only the simulation of 5 days was shown, the flow pattern is consistent with the averaged sea surface currents in August (Figure 2.4. d, excluding the hurricane period). Since different areas of the bloom behave differently, we organized our analysis of the entire bloom into three section Area A, B and C.

Area A (39.75~40.625°N, 74.25~73.25 °W) covers the northern coastal area including the estuary of HR. The bloom in Area A first emerged at the estuary of the Hudson River along the coast of Long Island, then moved to the south along the New Jersey coast and merged together with the existing southern portion of the bloom at around 39.75°N. Area B (38.75~39.75°N, 74.5~72.75°W) is the southern area off New Jersey, where most upwelling centers documented previously are located (e.g. [Glenn *et al.*, 1996]). The majority of simulated water parcels within Area B were advected offshore, and converged between the 30m and 70m isobaths from Aug 12<sup>th</sup> to Aug 17<sup>th</sup>. Area C (40~40.5°N, 73.25~72°W) is an area away from the coast. In our simulation there was almost no position shift for the water parcels within this area. The mean current field between Aug 1<sup>st</sup> and Aug 24<sup>th</sup> from HF radar (Figure 2.4. d) shows consistent flow patterns that prevail all through August until the hurricane. These currents were moving southward in the north coast (Area A), moving offshore in the south coast (Area B), and forming an eddy-like anti-clockwise flow in Area C with the velocity minimum zone at 40.08°N, -73.25°W.

Since only advection is accounted in the simulation, the difference between the simulated advection pattern and the observation represents local variations of the bloom given that the diffusion can be neglected. If the assumption is made that the Chl vertical advection and diffusion are small under the condition of well mixed surface layer, the local variations could be mainly the result of biological processes. For Area A, separation between the simulation and the observation mainly occurs in the southern edge. Area B shows the most agreement between the observed pattern and our derived pattern in the offshore area (west of 74°W), with differences between coastline and 74°W, co-locating with previously identified upwelling centers (Glenn et al., 2004). For Area C, the observation shows little agreement with simulated results. There is no significant simulated advection in this area. But high Chl was observed on satellite images. Biological processes such as growth of phytoplankton are more possible explanations for these deviations rather than surface advection.

### **2.3.3 Roles of the Wind in the Horizontal Advection**

Previous investigations (Gong et al., 2010; Jiang et al., 2010) revealed the importance of the wind in the cross-shelf transport. It is necessary to investigate how much the transport of the bloom could be attributed to the wind. Figure 2.5 A shows the correlation coefficients between the magnitude of the sea surface currents derived from HF radar measurements and that of the sea surface wind stress. For the areas where p-values (of null hypothesis) are larger than 0.05, we set the values to be 0 in the figure. The magnitude of sea surface currents are mostly correlated with the wind stress around the 50m isobath to the south of the Hudson Valley (within Area B), with the correlation coefficient ranging from 0.38~0.77. While for the middle shelf north to the Hudson Valley, inner shelf and outer shelf, there is no significant correlation. This

is suggesting that the wind driven circulation could explain the horizontal advection within Area B but not the whole bloom area.

In addition, the general direction of the wind transport could be determined simply using the centroid trajectory simulation. The simulated drifters were released (Section 2.2.4) at the initial location of the centroid of the bloom (Figure 2.5 b) and the result are compared with the bloom centroids calculated from satellite images. The wind-driven simulation within Area B agrees well with observation. The simulated trajectory separated from the observed trajectory by 5.04 km in distance and 4° in direction. Thus the offshore transport in Area B is predominately driven by wind-induced currents. However, if we include the whole bloom area (Area A, B and C) in the simulation, the separation between simulation and observation will significantly increase to 8.03 km in distance and 32.7° in direction. Thus wind driven transport is not valid for the whole bloom area. The driving force within Area A is probably the entrainment of the coastal current from east of the Long Island (Figure 2.4. d). We also noticed the sea surface currents and wind are correlated in Area C, where cyclonic flow is observation. That means the anti-clockwise flow in Area C is very likely due to the wind stress curl, which will be further investigated in Section 2.4.3.

## **2.4 Nutrient Delivery Mechanisms**

### **2.4.1 Area A: Upwelling and the Eddy at the Estuary**

In order to analyze how the Chl evolved in Area A, we made a set of transects (Figure 2.6 a) parallel to the coastline. The interval between each transect is around 10km. Chl along each transect is plotted over time (e.g., Figure 2.6 b) and a one-dimensional Chl time series was generated by averaging over each transect (Figure 2.6

c). All five transects have similar features thus only one is shown here. The Chl level is low in the beginning and middle of July. The Chl started to increase from the end of July, reached its first peak at Aug 6<sup>th</sup>, and decreased significantly to normal level at around August 11<sup>th</sup>. From August 12<sup>th</sup> to Aug 20<sup>th</sup>, the Chl increased again, reaching its second peak and kept high until the hurricane. Explanations for the high-low-high pattern will be provided based on observation data.

Persisting northward wind (Figure 2.7) was observed at Station Sandy Hook, NJ from Aug 5<sup>th</sup> to Aug 8<sup>th</sup>, with wind speed as high as 10m/s. And the sea surface currents was moving in the offshore direction. Cold temperature pattern could also be viewed close to the coast between 40°N to 40.5°N. Thus there was upwelling occurring in Area A, which was collocated with the high Chl area observed on Aug 6<sup>th</sup>. Based on model simulations (Choi and Wilkin, 2007), a freshwater plume is not likely to form an alongshore coastal current under northward wind condition, thus the influence of Hudson River for this period could be excluded.

The wind on Aug 11<sup>th</sup> is relatively weak (4m/s) compared to Aug 6<sup>th</sup> (10m/s), with direction changing from northward to eastward and southward. The sea surface currents also changed direction. And no strong cold temperature pattern was found along the New Jersey shelf. The coastal upwelling in Area A, if still existing, should be very weak. This explains the trough of Chl on Aug 11<sup>th</sup> in Area A.

Meanwhile a clockwise eddy was observed in the estuary along the Long Island coast from HF radar currents, occurring on around Aug 10<sup>th</sup> and persisted for at least three days. This eddy consisted of two components: the Hudson River outflow moving eastward and the cold coastal current from east of the Long Island moving westward. In contrast to the decreasing Chl in the northern New Jersey coast, we

observed a new bloom section at the eddy's location expanding rapidly from coastal area at 40.5°N on Aug 10<sup>th</sup> to 40.1°N on Aug 11<sup>th</sup>. There were recirculating eddy events and the subsequent increased phytoplankton biomass recorded in 2005 (Frazer et al., 2006). Discussions on the dynamic of the eddies at the Hudson River estuary (Chant et al., 2008; Moline et al., 2008; Schofield et al., 2013) suggested that the increased residence time and mixing rates in the eddy could facilitate the build-up of the biomass. The high Chl area were revealed to propagate southward in our advection simulation, and were simultaneously co-located with the southward coastal currents observed in HF radar data (Figure 2.7).

It is necessary to mention the influence of the Hudson River discharge. Previous studies have shown that low freshwater discharge from Hudson River could increase water residence time (Zhang et al., 2010) and stratification and thus deepen the photic zones, all of which could increase the primary production in the Hudson River estuary (Howarth et al., 2000). The discharge was high during the end of June and kept on being lower than historical mean since the middle of July (Figure 2.8). Thus the low discharge condition can also contribute to the biomass increase for our case. However, we did not find direct correlation between the gauge measurement of the discharge and the biomass time series. The influence of the discharge to the downstream biomass is not direct and explicit (e.g., through stratification etc.).

#### **2.4.2 Area B: Coastal Upwelling**

The bloom in Area B is co-located with previous identified upwelling centers. The in-situ measurements from glider data on Aug 16 (Figure 2.9 a, b, and c) show upwelling condition in the region with an elevated thermocline and decreased surface temperature. The thermocline depth was around 15m in the north coast of New Jersey

but reduced to less than 5m on Aug 16<sup>th</sup>. The upwelling locations were also close to the area which denotes the separation between the observation and advection simulation (Section 2.2.3). This suggests biological processes associated with strong upwelling could occur within Area B and be indicated by the differences between the advection simulation and the observation. In addition, we decomposed the buoy wind vectors into alongshore and offshore components (Dzwonkowski, 2009) and calculated the related Ekman transports with the alongshore component (Figure 2.10). Upwelling favorable wind conditions dominated in the coastal area from July through August.

### 2.4.3 Area C: Wind Stress Curl and Ekman Pumping

So far there are several features found in Area C in August 2011. (1) There were anti-clockwise flow patterns as identified from mean HF radar currents (Figure 2.4. d) with weak currents in the center and strong currents rotating around (i.e., divergence); (2) The sea surface currents were correlated with wind stress; (3) The bloom in Area C had the most significant difference between our advection simulation and observation: there was almost no position shift in simulation in contrast to the expanding bloom in satellite images. These features suggest that there could be strong Ekman pumping induced by wind stress curl, and thus results in biological processes separating the advection simulation and the observation.

The Ekman pumping velocity is derived from the wind field (Smith, 1968)

$$w_E = (\partial\tau_y/\partial x - \partial\tau_x/\partial y)/(\rho_{water}f) \quad (2-5)$$

The monthly wind stress curl climatology in August has been subtracted from the results to give Ekman pumping anomaly. The anomaly can show how our case deviated from the mean condition, though patterns are the same as the original data

without subtracting the climatology. Corresponding to the rapid expanding bloom in Area C, there were positive wind stress curl areas and thus positive upward velocities (Figure 2.11 a) in the area of  $73^{\circ}\text{W}\sim 72.5\text{W}$ , around  $40^{\circ}\text{N}$ . This upwelling event lasted for 4 to 5 days beginning from Aug 13th. While for the downwelling area centered on  $73.25^{\circ}\text{W}$ ,  $39.75^{\circ}\text{E}$ , Chl gradually decreased. Also this Ekman pumping area corresponded to the cold water pattern observed in the SST anomaly data in the middle of August (Figure 2.11 b, rectangle area).

The magnitude of the Ekman pumping due to wind stress curl and that of coastal upwelling due to alongshore wind were compared. Previous studies in California Current Systems concluded that both Ekman pumping from wind stress curl and Ekman transport from alongshore winds can work synchronously to provide nutrients to surface water and are of the same order (Macías et al., 2012; Pickett, 2003). For our case, the pumping velocity was converted into the vertical transport by integrating the velocity over the Ekman pumping area (approximately 58km in width). The converted result is  $0.11\text{ m}^2/\text{s}$ . The coastal Ekman transport from alongshore wind is approximately  $0.16\text{ m}^2/\text{s}$ . The transport from Ekman pumping is of the same order, though smaller, than the Ekman transport induced by the alongshore wind.

#### **2.4.4 Long Time Perspective**

So far we took the case of the 2011 summer bloom off New Jersey as an example to investigate factors influencing summer bloom development. Different nutrient delivery mechanisms and transport driving forces have been proposed for each sub-area. Here we show how this bloom compares to the conditions over the recent decade (2002~2013).

Both spatially averaged Chl and detected bloom area were calculated (Figure 2.12) for the decadal scale off New Jersey coast (74.5~72°W, 38.75~40.6°N, red rectangle in Figure 2.1). In 2011, the summer bloom has the area-averaged Chl value as  $4.2\text{mg/m}^3$ , and covers approximately  $2.9 \times 10^4 \text{km}^2$  of coastal ocean ranging from coastline to the 70m isobath. For other blooms occurring only during summers from 2002 to 2013, the highest Chl value occurred in 2010 with  $2.7\text{mg/m}^3$ , and the largest area occurred in 2006 with  $2.5 \times 10^4 \text{km}^2$ . The 2011 case is one of the largest summer blooms in the past decade. If we include blooms from all seasons, the highest Chl values occurred in the spring of 2013 with  $3.9\text{mg/m}^3$ , and the largest bloom area occurred in the spring of 2012 with  $7.0 \times 10^4 \text{km}^2$ . The 2011 summer case is still among the highest Chl blooms.

It is necessary to investigate various conditions leading to blooms for each sub-region in the longer time scales. In order to do that, bloom detection thresholds for each sub-region have to be determined. If the Chl exceed the threshold, we consider the event as a bloom. The bloom thresholds (1.6 times the median values) are the same as we used to detect the bloom (Section 2.2.2) but it is area-averaged values here. Area A has the highest bloom threshold ( $5.97\text{mg/m}^3$ ). This is reasonable since it is close to the estuary of the Hudson River and the metropolitan area thus it is more eutrophicated. The threshold of Area B ( $2.49\text{mg/m}^3$ ) is close but higher than that of Area C ( $1.77\text{mg/m}^3$ ). This is consistent with our magnitude estimation that coastal upwelling is stronger than Ekman pumping but still of the same order.

The bloom events in these three sub-regions were not synchronized. It is more frequent for the Chl of Area A to exceed the threshold but less for the other two. All three sub-regions are showing threshold-exceeding Chl values in the summer of 2011.

This could explain why there was the highest Chl in 2011. Similar situations happened in other years which also generated either high Chl or large bloom coverage.

It would then be necessary to check whether the mechanisms identified in the case of 2011 could apply for the other years. Possible mechanisms of blooms include eddy formation, Hudson River discharge, upwell and Ekman pumping. 85% of bloom events in Area B are coupled with upwelling prevailing condition (upwelling occurs longer than 15 days during one month). 68% of the bloom events in Area C are with the Ekman pumping prevailing condition (positive curl occurs longer than 15 days during one month). Due to lack of decadal time series of HF radar currents, we were not able to examine the eddy condition in Area A. However, we found 75% of bloom events in Area A are accompanied by the low-discharge conditions, which is not the case for the summer of 2011. Bloom processes are complex and other factors (grazing, sinking, and light) may also be influencing the bloom. That's why the conditions proposed here could not explain 100% of the events.

## **2.5 Discussion**

In the summer of 2011, a large phytoplankton bloom occurred over the New Jersey shelf. The decadal Chl time series reveals that this bloom is one of the largest summer blooms occurring in this area. Compared with the more common spring and fall bloom, the 2011 case is within the highest Chl events. Recalling that in 1976 combined factors resulted in a large scale phytoplankton bloom and the consequent hypoxia events, as well as the fact that relatively large blooms could occur every season in this area, it is important to understand the physical mechanisms involving the development of large blooms and the 2011 summer bloom can be taken as a study case.

Through surface advection simulation from Aug 12<sup>th</sup> to Aug 17<sup>th</sup> in 2011, the flow patterns revealed through the simulation are consistent with the monthly mean sea surface currents. During this period the bloom experienced the most rapid expanding, with the coverage increased by 128% in Area B and 588% in Area C (though decreased by 47% in Area A as we discussed in Section 2.4.1). Thus Aug 12~17, 2011 is a representative period of bloom expanding stage to start from, although our data and analysis covers most of the month.

Different transport and nutrient delivery mechanisms are proposed for sub-regions in this study. (1) The sub-bloom within Area A experienced a high-low-high pattern in Chl time series. The first Chl peak is due to the upwelling along the New Jersey coast and the second Chl peak is the result of the clockwise eddy at the Long Island shore. The Hudson River outflow moving eastward encountered the strong coastal current moving westward and formed a clockwise eddy at the Long Island shore. The subsequent bloom is entrained by the coastal current flowing southward and merged into the southern bloom section. All these occur within the low-discharge condition of the Hudson River. (2) For the bloom section in Area B, upwelling events in the southern New Jersey coast induced the phytoplankton blooms. Correlations between the sea surface currents and wind stress are mostly limited within the middle shelf of Area B, while wind induced currents are the dominant factor for the offshore bloom transport. (3) For Area C, deviation found between advection simulation and the observation indicates that biological growth in this area. The estimated Ekman pumping in this area has the same magnitude as the costal upwelling, suggesting the Ekman pumping could also be one of the important nutrient supporting mechanisms. The wind data resolution is only 25-km, while at least 10-km data is required to solve

small scale wind patterns (Winant and Dorman, 1997). Thus the order of magnitudes of the results, rather than the absolute values, are more meaningful.

Detailed roles of the wind in the bloom are revealed in this study. Along the coast, the alongshore components could induce coastal upwelling events. In the middle shelf, the wind stress are correlated with the sea surface currents, though this correlation is limited within specific area not the whole continental shelf. In addition, the wind stress curl can induce Ekman pumping and support the expanding of the phytoplankton bloom, which was never documented off the New Jersey coast except in the shelfbreak region (He et al., 2011b). The essential role of the wind in the bloom events may suggest the relationship between the phytoplankton blooms off the New Jersey and atmospheric forcing such as North Atlantic Oscillation.

Concerning the diagnostic result (Section 2.3.1 and Figure 2.3), we have noticed the local temporal variation term and horizontal diffusion term are relatively small compared with the horizontal advection term and the residual term. In the case when the horizontal advection and the residual are one order larger than the other two, the equation is basically the balance between the horizontal advection and the residual term (source/sink and vertical exchange). This explains the bloom expansion process: the phytoplankton bloom grows where plenty of nutrients are supplied, and is transported along with currents. In this process the local Chl concentration will keep relatively steady due to the replenishment of local source/sink/vertical exchange. On the other hand, if the equation balance is between the local temporal term and the advection, it then means the local Chl variation is solely due to the horizontal advection. That is, the bloom is generated remotely, and is transported to the spot. Moreover, obviously there could be cases (for specific smaller areas and during

specific time frame) that all of the four terms are of the same order, which then will be a more complicated situation beyond the scope of our case here.

We have identified different transport and nutrient delivery mechanisms, in terms of physical processes, for each sub-region in the case study of 2011 summer bloom. By checking with the longer time series of the Chl, we found that bloom conditions in all three sub-region occurred simultaneously, leading to the high Chl concentration in the summer of 2011. The proposed mechanisms could apply to most of bloom events from 2002 to 2013. Our study investigated detailed influences of different factors in blooms, and could provide a baseline with possible explanations for all large blooms, especially summer blooms, off the New Jersey coast.

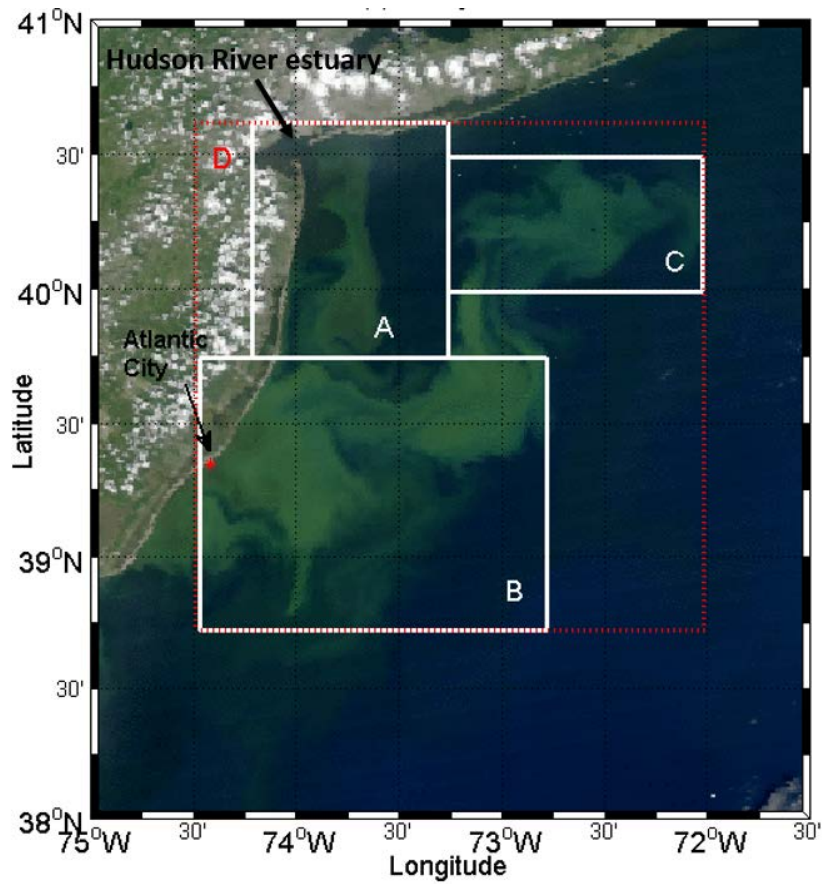


Figure 2.1. True color image of MODIS on Aug 17th. The bloom is divided into three subareas A, B and C, shown as white rectangle in the figure. Rectangle D is the area over which Chl are averaged in the long term time series comparison.

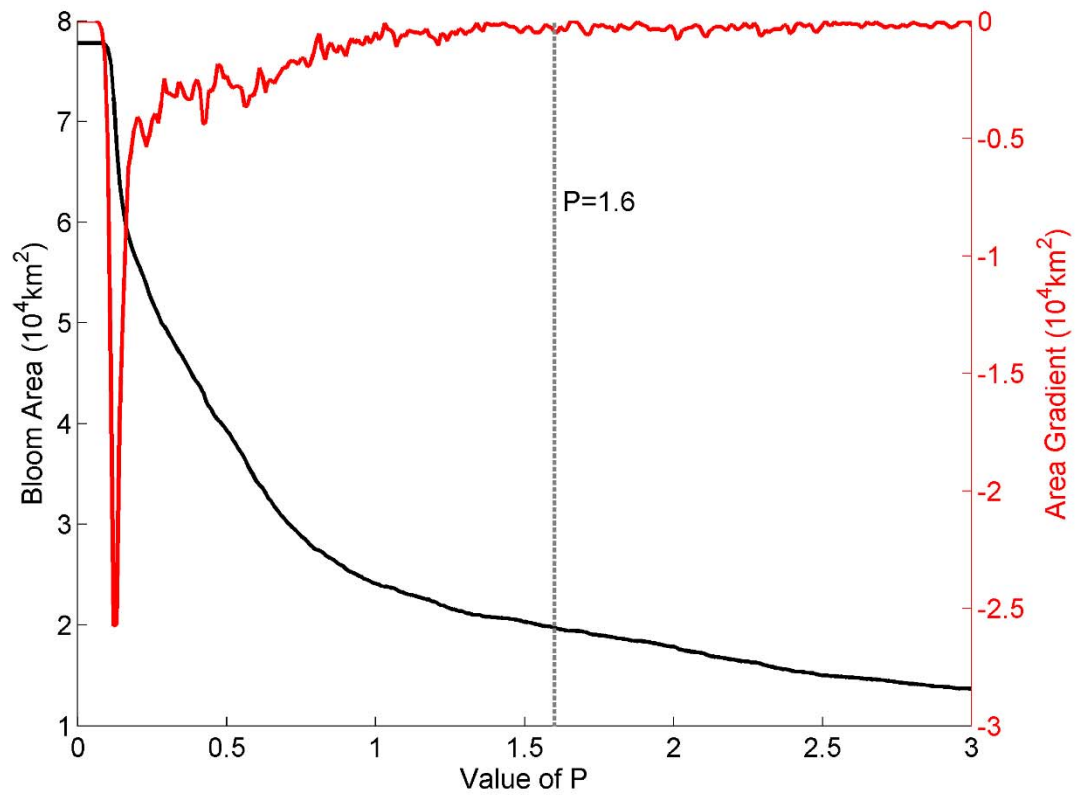


Figure 2.2. The bloom detection (using the Chl data on August 17, 2011). Black line: Detected bloom area varying with threshold P. Red line: the gradient of detected bloom area varying with P.

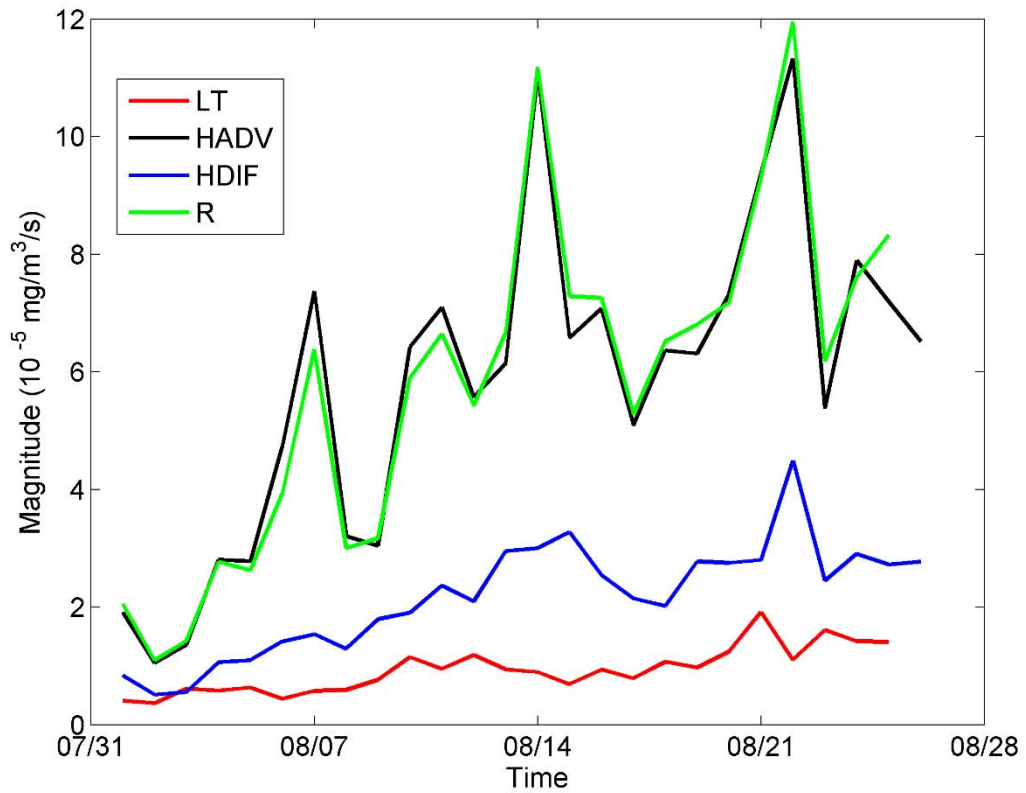


Figure 2.3. Magnitude diagnostics of the bloom evolution processes. The results are averaged over the whole study area during August of 2011 (excluding the hurricane period). Corresponding to the four terms in Equation 3, LT (red) is the magnitude of the local temporal variation of Chl, HADV (black) is the horizontal advection, HDIF (blue) is the horizontal diffusion/mixing, and R (green) is the residual term.

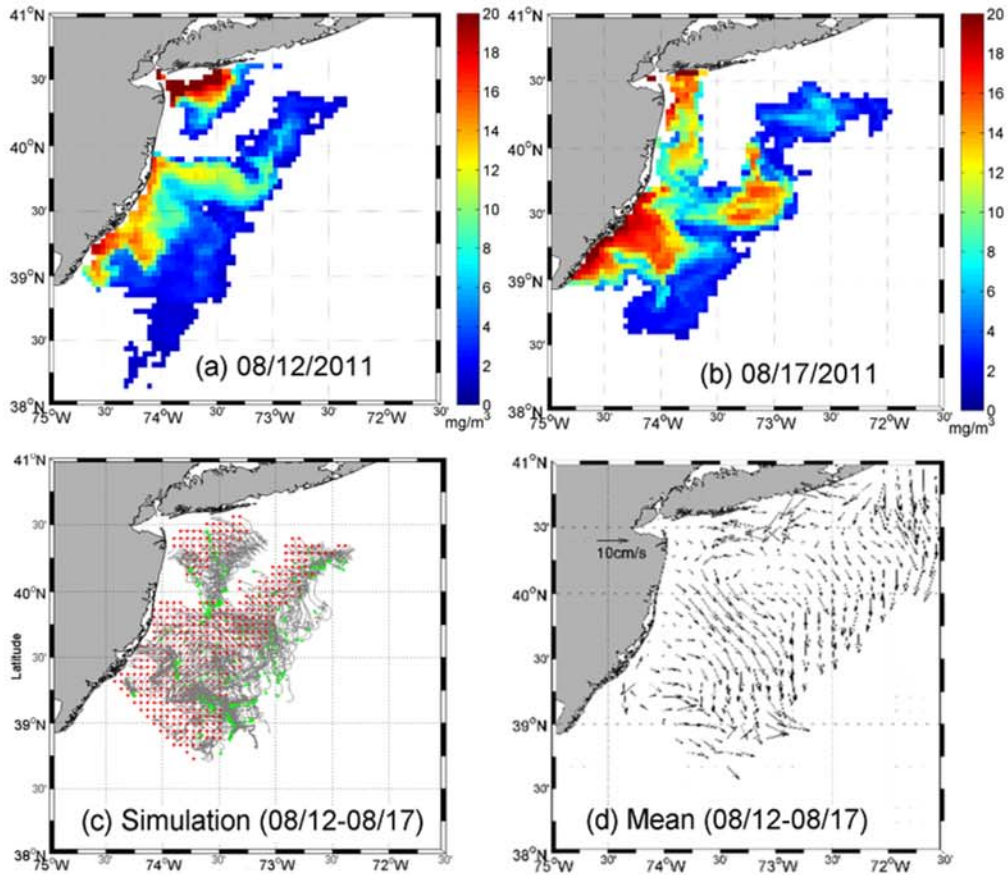


Figure 2.4. Advection simulation. (a) initial distribution observed by MODIS on Aug 12th, 2011; (b) final distribution observed by MODIS on Aug 17th; (c) advection simulation using sea surface current from HF radar measurements. Red points: initial positions; Green points: simulated bloom distribution pattern after 5 day derivation; (d) mean HF velocities from Aug 1st to Aug 24th.

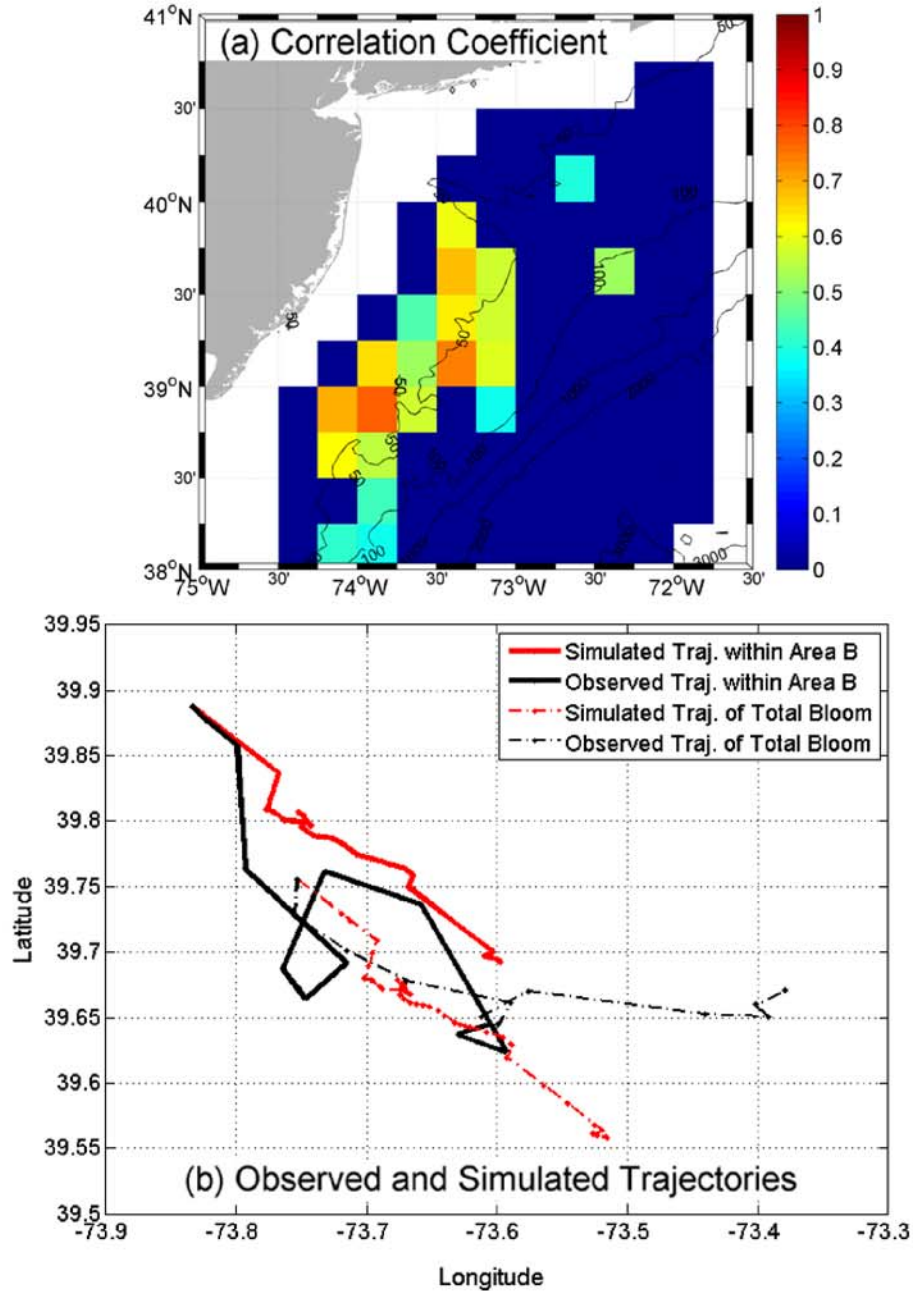


Figure 2.5. The role of the wind. (a) Correlation coefficient ( $p < 0.05$ ) between the magnitudes of sea surface current from HF radar and the magnitudes of sea surface wind stress. All areas with  $p > 0.05$  were set to be zero. (b) Comparison between the centroid trajectory and the simulated trajectory from current induced by wind. Black lines show observed trajectories from Aug 10th to Aug 23rd. Red lines represent the simulated trajectories during the same period. The dashed lines are calculated within the total study region, while solid lines are calculated only in the Area B.

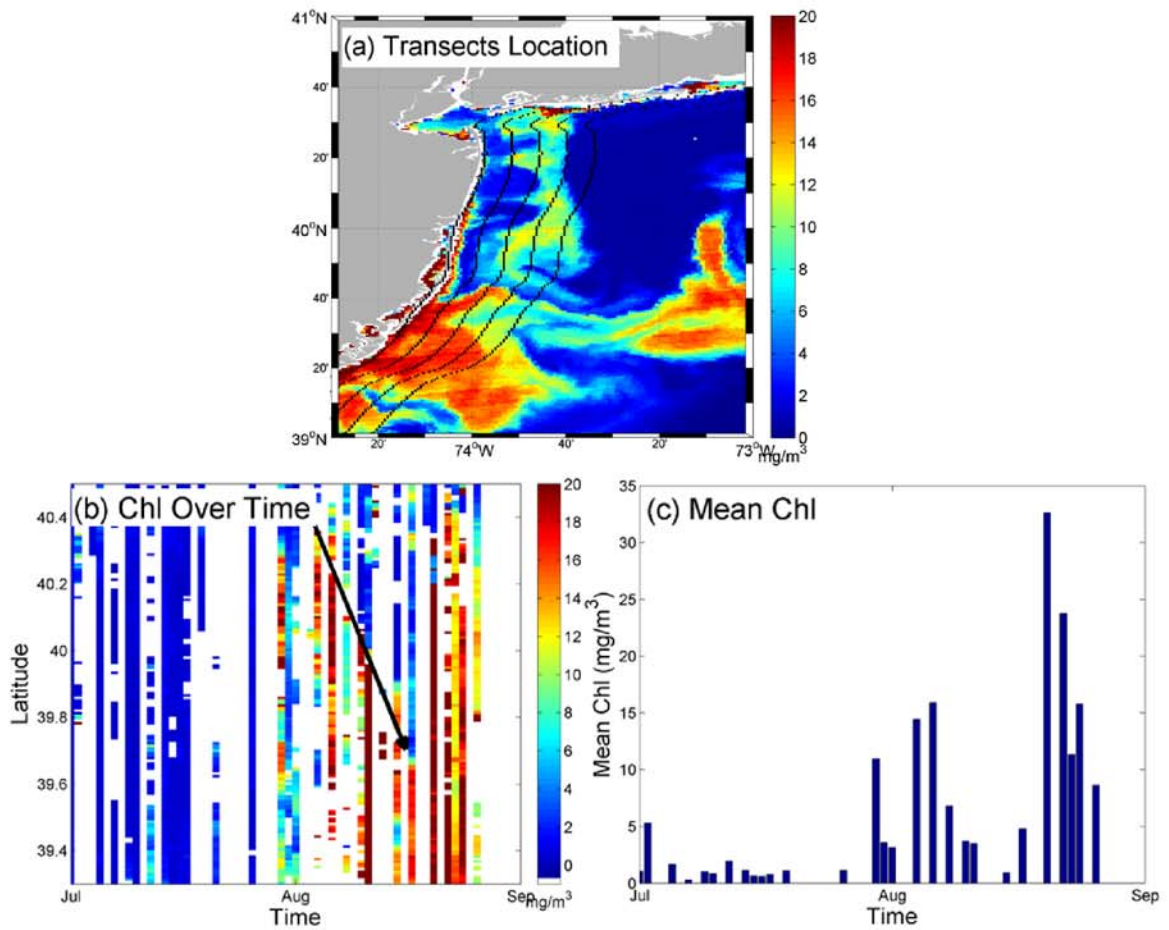


Figure 2.6. Chl over Area A. (a) Black lines are the transect location along the coast. The background image is the Chl data on Aug 17th. (b) Chl varies over time from only one transect (the second from coast). The black arrow is showing the low Chl water transporting south. (c) Chl time series averaged along one transect (the second one from the coast) within Area A.

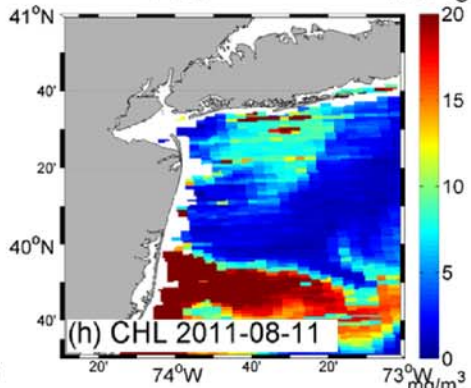
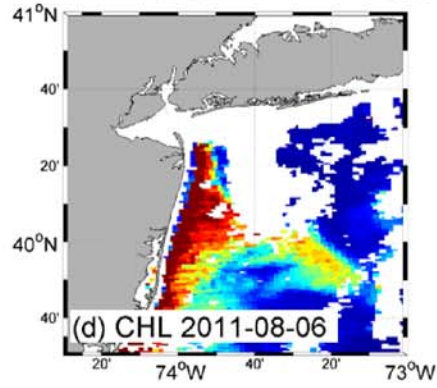
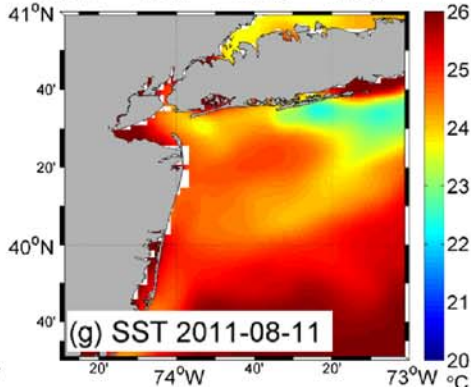
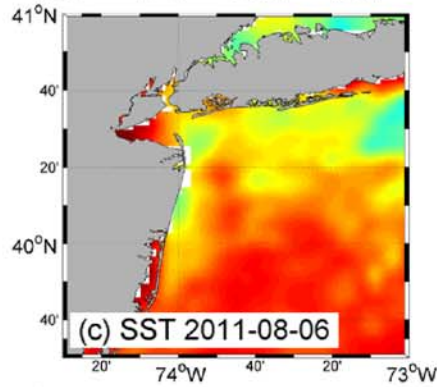
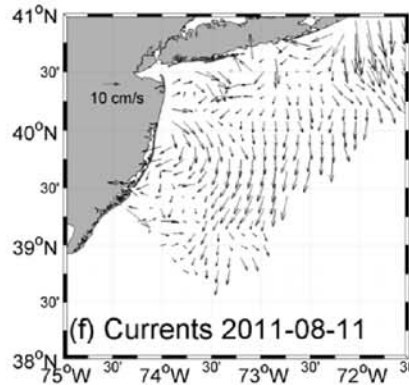
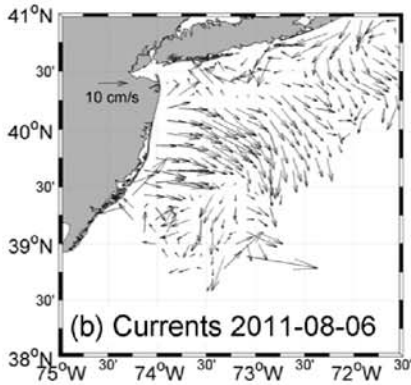
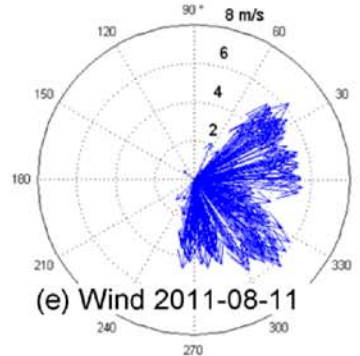
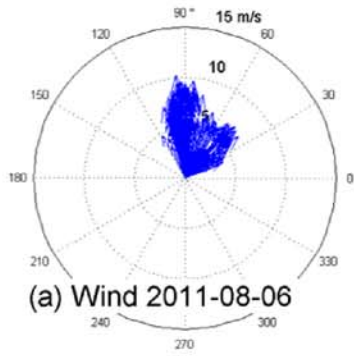


Figure 2.7. The condition comparison between 2011/08/06 and 2011/08/11. From top to bottom are the wind current from buoy station at Sandy Hook, daily averaged sea surface currents measured by HF radar, SST from G1SST/JPL, Chl from MODIS/Aqua. Left column (a to d) August 6th. Right column (e to h) August 11th.

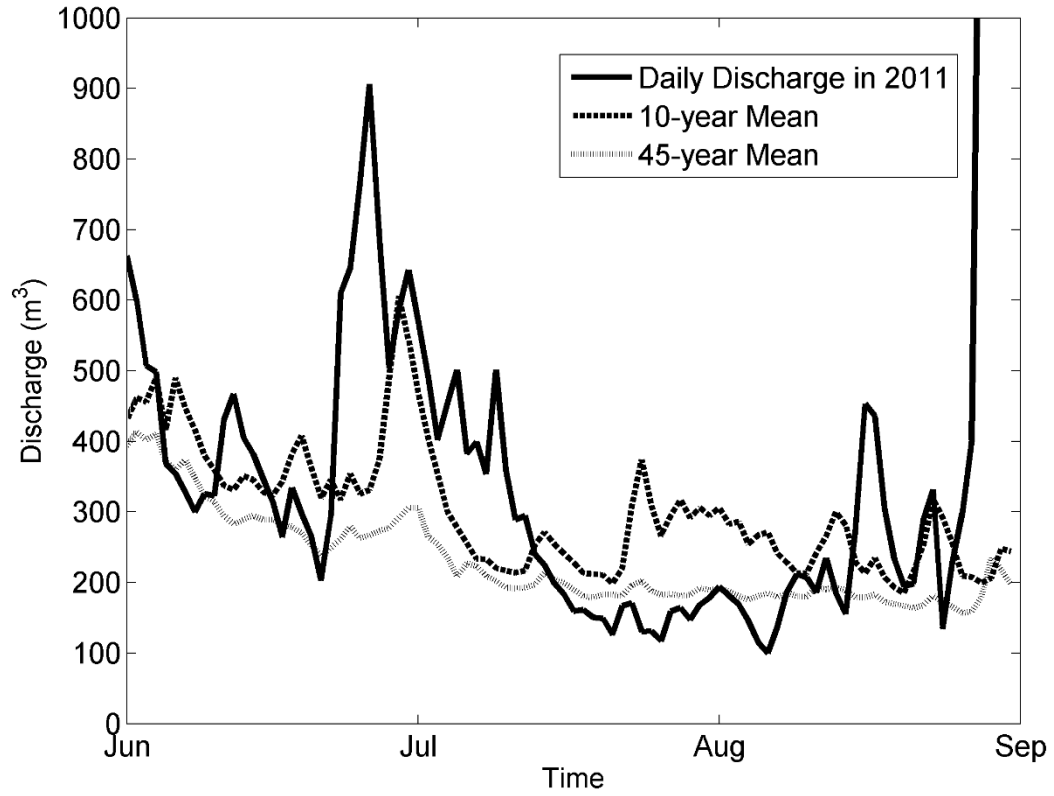


Figure 2.8. The freshwater discharge of Hudson River measured at Green Island, NY. The solid, dashed and dotted black lines represent the daily measurement, mean discharge record over 10 year and mean discharge record over 46 year.

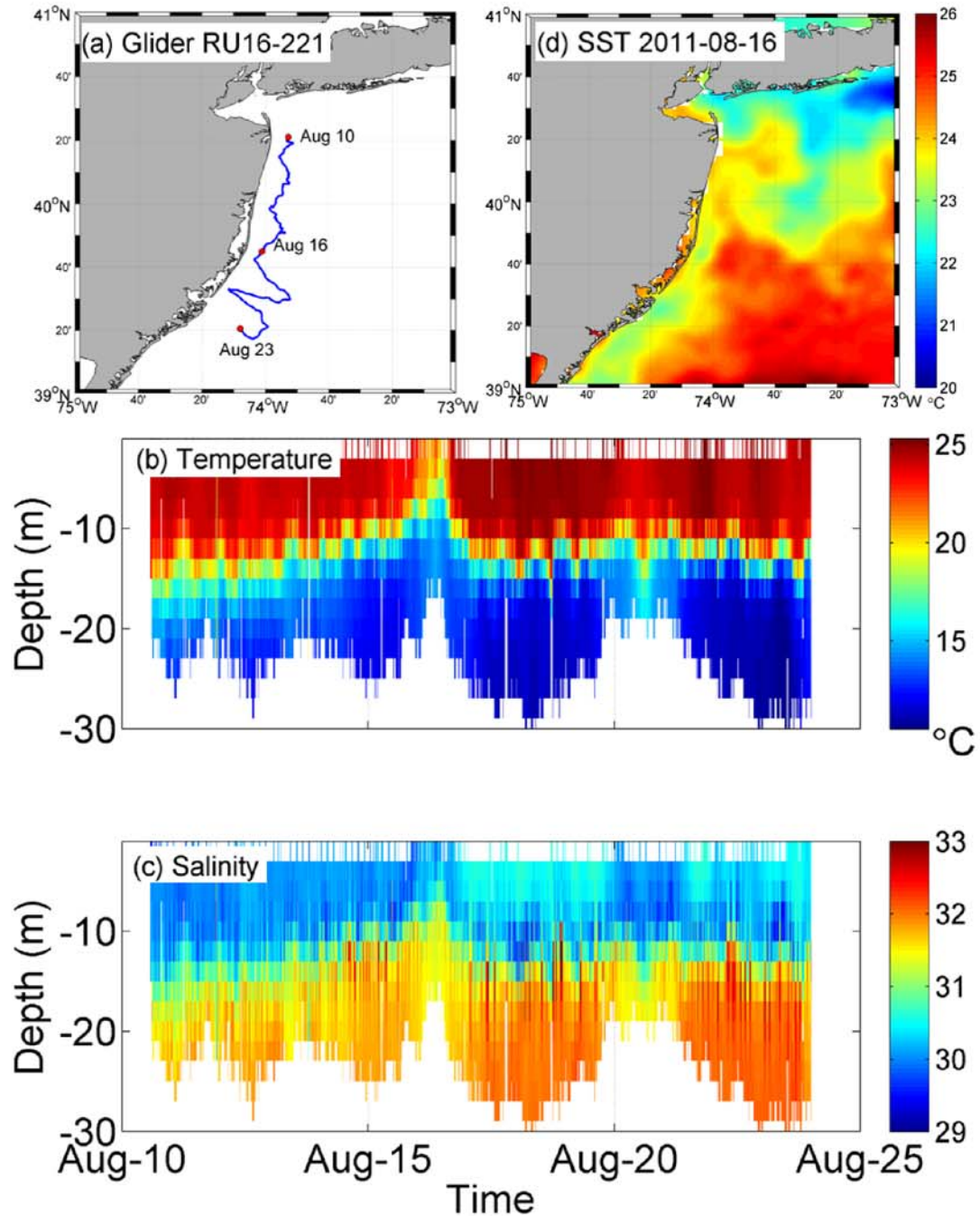


Figure 2.9. (a) Glider (RU16-221) locations. From Aug 10th to Aug 16th, the glider moves within Area A. From Aug 16th to Aug 23rd the glider is moving within Area B. (b) Salinity profile from the glider measurement. (c) Temperature profile from the glider measurement. (d) SST measured by AVHRR on Aug 12th of 2011 as a simultaneous compliant data, showing the surface temperature distribution along the coast of New Jersey.

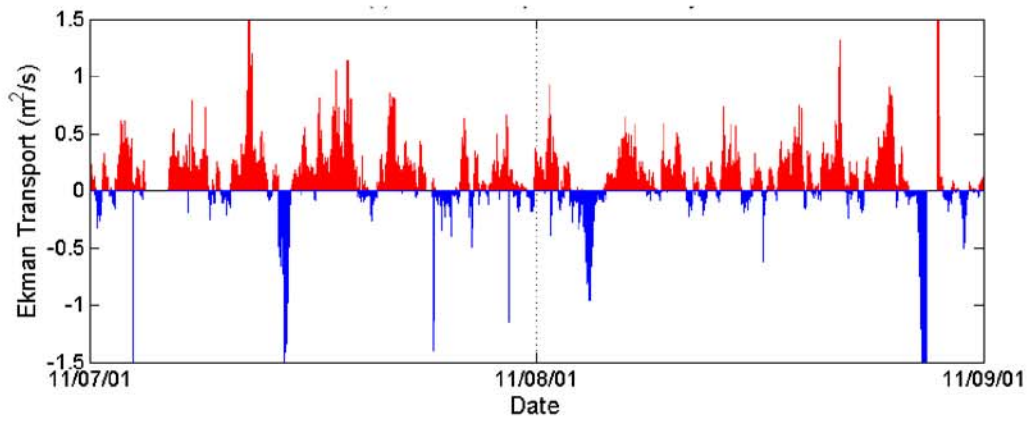


Figure 2.10. The offshore transport estimated from along shore wind component of Buoy data (Atlantic City).

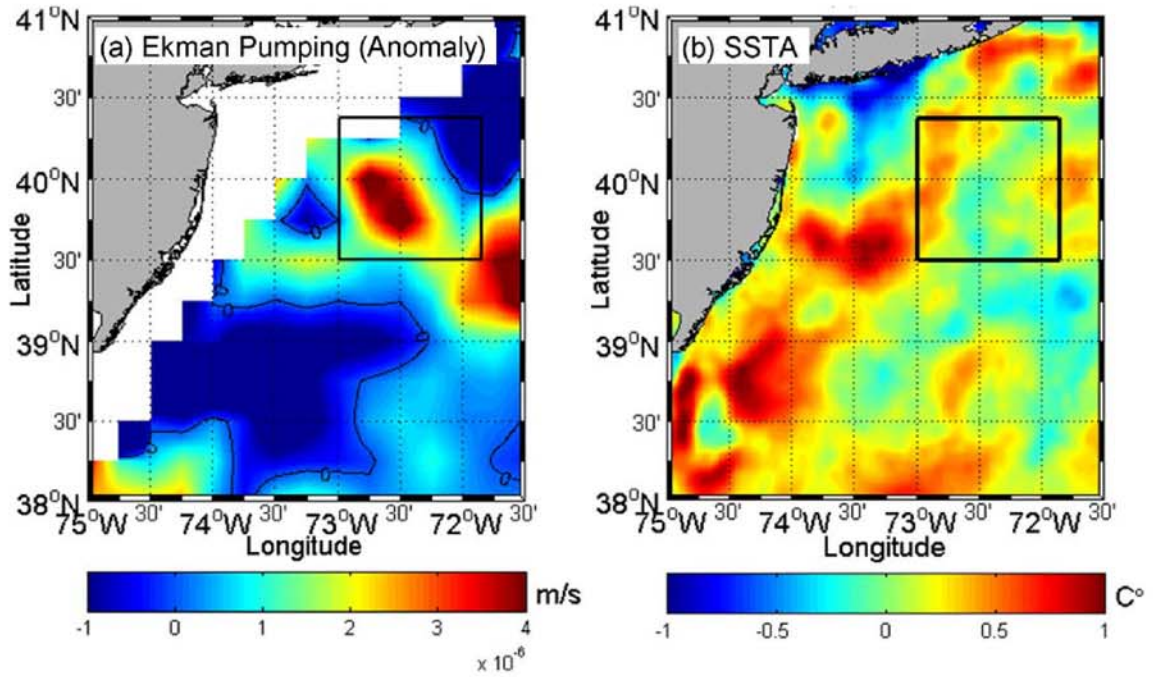


Figure 2.11. (a) Ekman pumping (anomaly) derived from the wind stress curl anomaly and averaged from Aug 13th to Aug 17th. Positive areas represent the location where upwelling occurs. (b) Sea surface temperature anomaly (SSTA) averaged from Aug 13th to 17th. Area I and Area II are showing cold water pattern corresponding to the pumping area in (a).

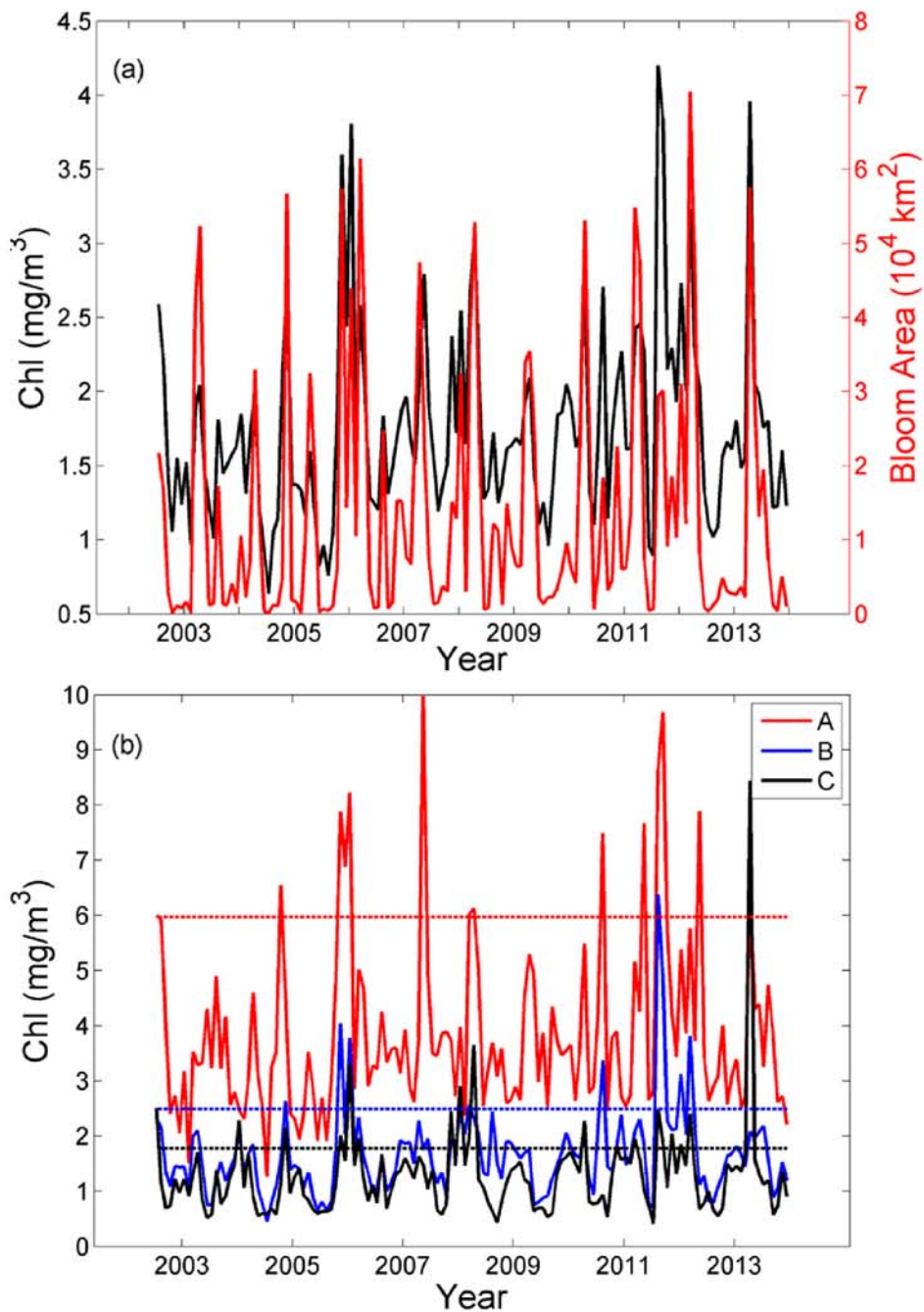


Figure 2.12. Multi-year scale Chl time series. (a) Black: area-averaged 4km chlorophyll a concentration in the New Jersey coast; Red: time series of detected bloom spatial coverage. (b) Chl condition for each sub-region detected from the year 2002 to 2014. Red, blue and black lines represent the detected bloom area within each sub-region. The dashed lines represent the threshold (1.6 times of the median value) for each sub-region.

## Chapter 3

### THE MODULATION OF THE SEASONAL CROSS-SHELF SEA LEVEL VARIATION BY THE COLD POOL IN THE MIDDLE ATLANTIC BIGHT

#### 3.1 Introduction

Previous studies on the cold pool were based on the in situ measurements and model results. However, the sparse nature of in situ measurements limited further investigation of the cold pool because no continuous time series are available. Moreover, remote sensing data with large spatial coverage and long time series were seldom used in the cold pool study because the cold pool water locates under the thermocline. However, recent studies revealed the possibility of studying subsurface processes with surface variables retrieved from satellite data (Klemas and Yan, 2014), such as the application of sea level anomaly (SLA) from altimeter on Mediterranean Eddies tracking (Ienna et al., 2014; Yan et al., 2006), by removing surface layer steric components from SLA. Based on previous studies of the steric height (Gill and Niller, 1973), the cold pool with lower than ambient temperature generates the depressed thermal steric height and thus induce depressed sea level anomaly. The cold pool can possibly have surface expressions in the sea level anomaly observation. It is necessary to investigate the relationship between the cold pool and altimetry SLA, not only for a baseline of cold pool studies utilizing remote sensing data, but also for a better understanding of the response of the sea level variations to mesoscale features on the continental shelf.

This chapter focused on how the cold pool feature in the thermal and haline annual cycles influence the cross-shelf SLA. The work is organized as follows. Firstly, we applied single annual harmonic fitting to obtain the 20-year mean annual cycles containing the cold pool feature from in-situ measurements. Secondly, different steric components are derived from the measurements and compared. Finally, attempts were made to extract seasonal components from altimetry SLA data to reveal the cold pool pattern, and the locations of SLA depression are compared to the bottom temperature.

## **3.2 Data and Methods**

### **3.2.1 Data**

Temperature and salinity profiles of Conductivity-Temperature-Depth (CTD), Profiling Floats (PFL), Expendable Bathythermograph (XBT), and Mechanical Bathythermographs (MBT) are collected from World Ocean Database (WOD/NOAA) during 1993-2012 in MAB. CTD and PFL measurements have coupled temperature and salinity (TS) profiles and are used in the derivation of the steric components (Gill and Niller, 1973). Most measurements within 1000-m isobath come from CTD. XBT and MBT do not provide salinity profiles and thus are used in the cold pool location determination together with CTD and PFL. Following criterion are applied at each location to make sure the profiles are “acceptable” (as of (Lentz, 2003)): more than 5 samples are available within one vertical profile; the measured temperature values are within  $-2\sim 35$  °C; salinity values are within  $0\sim 40$ ; the deepest samples do not exceed the water depth by 10m. A subset of 24225 TS couples are available from a total of 26702 within MAB ( $35\text{-}42^{\circ}\text{N}$ ,  $76\text{-}68^{\circ}\text{W}$ ).

We use the gridded Sea Level Anomaly (SLA), which is one of Ssalto/Duacs multi-mission altimeter products released on April 15<sup>th</sup>, 2014 by AVISO. This dataset contains daily maps from 1993 to 2012 on a 1/4 degree Cartesian grid referring to a 20 year mean (1993-2012) with tidal and inverse barometer corrections. All data points within 25km from the coastline, though shown as part of our figures, should be excluded or analyzed with caution to avoid the contamination from land in altimeter data. The along track SLA measurements (e.g., track 50 of Jason 1 and 2) are also available from AVISO but are not used in this study based on the concerns mentioned in Section 3.2.2. The daily gridded SLA was first interpolated to a transect, as described in Section 3.2.2, so that we got the daily time series of SLA over a transect line. Moreover, the daily time series were averaged over 20 years for each month resulting in a monthly climatology or the mean annual cycle of SLA.

### **3.2.2 Cross-shelf Transect and Harmonic Fitting**

Previous literature sources reveal that the cold pool persists from late spring to early fall. By composing all available bottom temperatures of CTD and PFL from April to September during the past two decades (1993 to 2012), we obtained the “footprint” of the cold pool with bottom temperature  $<10^{\circ}\text{C}$  (Figure 3.1 A). In the cross-shelf direction, the cold pool locates within 100-m isobath over the middle and outer shelf. In this study we follow the definition of *Csanady* [1982] that the middle shelf is around 48m isobath and outer shelf is around 96m isobath. In the along-shelf direction, the cold pool distributes from Nantucket Shoals in the northeast to Cape Hatteras in the southwest with the coldest core locating around the Hudson Valley (Figure 3.1 B). We made a cross-shelf transect to investigate the influence of the cold pool on the cross-shelf sea surface height. The transect location is chosen based on

several concerns: the transect is made into the cold core of the cold pool to obtain the largest temperature gradient; the transect is outside the Hudson Valley to avoid possible anomalous features (Lentz et al., 2014). This transect has an offshore resolution of 15km and a vertical resolution of 1m (by linear interpolation). The interval of 15km was chosen to make sure the cold pool feature could be fully described but without a data gap. Ambient area within alongshore distance of 20km from the transect (grey rectangle in Figure 3.1 A) is also included to reduce the uncertainty of the sparse measurements. As we essentially focus on the annual cycles, single annual harmonic fitting (Lentz, 2008b) is applied to estimate the annual cycle at each location. The fitted data time series are described as:

$$y = a + bt + c \sin(\omega t) + d \cos(\omega t) \quad (3-1)$$

where  $t$  is time,  $\omega$  is the annual frequency. Using available CTD and PFL measurements as  $y$ , the coefficients of  $a, b, c, d$  are determined based on the least square theorem. The term  $a + bt$  denotes the linear trend, and  $c \sin(\omega t) + d \cos(\omega t)$  denotes the annual cycle. The value of  $b$  is on the order of  $10^{-4} \text{C} / d$  being consistent with the estimation of Forsyth et al. [2015]. The root-mean-squared deviation/error (RMSE) and the correlation coefficient  $R$  between the fitted and measured values were assessed (Figure 3.2). For the middle shelf within 90km offshore distance the RMSEs are less than  $2^\circ\text{C}$  with  $R > 0.8$  ( $p < 0.05$ ). The fitted annual cycle explains more than 64% of the temperature variations. Concerning the linear trend term in Equ. 1, approximations of different orders (using only the mean  $a$ , the first order approximation  $a + bt$ , and the second order approximation  $a + bt + ct^2$ ) were tested. The domain-averaged RMSE using the first order approximation is  $0.06^\circ\text{C}$  lower than using the mean while being  $0.01^\circ\text{C}$  higher than using the second order approximation.

We used  $a+bt$  as the linear trend approximation as a balance between the computational expenses and the accuracy. The data were finally averaged over 20 years to obtain the mean annual cycle. These steps are applied to TS profiles and the corresponding steric components.

### **3.2.3 Ensemble Empirical Mode Decomposition**

We applied Ensemble Empirical Mode Decomposition (EEMD) (Wu et al., 2009; Wu and Huang, 2009) to decompose the gridded SLA. The original Empirical Mode Decomposition (EMD) (Huang et al., 1998) is a useful tool for the nonlinear, nonstationary time series, separating the dataset into a finite number of intrinsic mode functions (IMFs). The method identifies different oscillation cycles based on their characteristic temporal scales. The number of IMFs is determined by the length of the dataset. EEMD (Wu and Huang, 2009) is an improved approach by adding white noise into the data and treating the mean of a sufficient number of trials as the final result. EEMD is believed to eliminate the mode-mixing problem of the original EMD algorithm. In this study, we used EEMD to extract the annual cycles (with above 90% significance level) of SLA data.

### **3.2.4 Steric Height Estimation**

There have been discussions on different components contributing to the sea surface height variation in open oceans (Fu and Davidson, 1995; Gill and Niller, 1973; Stammer, 1997; Vivier et al., 1999; Yan et al., 2006, 2004). Most are basin scale where the influence of the thermal field is dominant (e.g., (Yan et al., 2006)). Our essential interest are regions of the continental shelf and slope where the influences of freshwater and the sloping topography need to be assessed. The discussion on the

determination of velocities on the shelf and the reconstruction of coastal sea levels has a long history (Bingham and Hughes, 2012; Csanady, 1979, 1997; Sheng and Thompson, 1996; Helland-Hansen, 1934). In a right-handed coordinate system with positive  $z$  vertically up,  $x$  offshore direction along the transect and  $y$  alongshore direction perpendicular to the transect, the barometrically corrected sea level anomaly (Gill and Niller, 1973) can be expressed as

$$\eta'_{Alt} = \eta'_{steric} + \frac{p'_b}{\rho_0 g} \quad (3-2)$$

where the steric height anomaly

$$\eta'_{steric} = \int_{-H(x,y)}^0 [\varepsilon(x, y, z, t) - \bar{\varepsilon}(x, y, z)] \rho_0 dz, \quad (3-3)$$

and  $H(x, y)$  is the water depth,  $p'_b$  is the time variable part of bottom pressure,  $\rho_0$  is a representative seawater density (a constant),  $\varepsilon$  is the density defect

$$\varepsilon = \rho(x, y, z, t)^{-1} - \rho_0^{-1} \approx \frac{\rho_0 - \rho(x, y, z, t)}{\rho_0^2} \quad (3-4)$$

and  $\bar{\varepsilon}$  is the corresponding temporal mean. Furthermore, the steric height deviation is be decomposed into the contribution of temperature and salinity, as

$$\begin{aligned} \eta'_{steric} &= \eta'_T + \eta'_S \\ &= \int_{-H(x,y)}^0 \alpha [T(x, y, z, t) - \bar{T}(x, y, z)] dz - \int_{-H(x,y)}^0 \beta [S(x, y, z, t) - \bar{S}(x, y, z)] dz \\ &= \int_{-H(x,y)}^0 \alpha T' dz - \int_{-H(x,y)}^0 \beta S' dz \end{aligned} \quad (3-5)$$

with the thermal and haline expansion coefficients

$$\alpha(x, y, z, t) = -\frac{1}{\rho_0} \frac{\partial \rho}{\partial T} \quad (3-6)$$

$$\beta(x, y, z, t) = \frac{1}{\rho_0} \frac{\partial \rho}{\partial S}. \quad (3-7)$$

$\bar{T}$  and  $\bar{S}$  are the temporal mean of the  $T$  and  $S$  at each location. Moreover, we are concerned as well with the steric height difference between two locations. Taking the horizontal gradient ( $\nabla$ ) of (3-3) in the  $x$ - $z$  plane, gives

$$\frac{\partial \eta'_{steric}}{\partial x} = \frac{1}{\rho_0} \int_{-H}^0 \frac{\partial \rho'}{\partial x} dz + \frac{\rho'_b}{\rho_0} \frac{\partial H}{\partial x} \quad (3-8)$$

and  $\rho'_b$  is the density variation over the seafloor in the offshore direction. The steric height difference is the sum of two parts. The first term on the right of Eq. (8) is the contribution of horizontal density gradient, and the second term is the influence of the bottom density along the varying topography. The second term is generated because we integrate the steric height over varying water depths. In the open ocean, a common reference level assumed with no geostrophic flow (say 3000m depth) is chosen thus the second term is negligible. For the continental shelf and slope, the first term decreases as the decreasing water depth and the second term cannot be neglected. For coastal areas where tidal gauges locate, the contribution from the first term almost vanishes, leaving only the contribution from bottom density and topography (Bingham and Hughes, 2012). The integration of the second term over the  $x$  direction can be considered as a correction under the assumption of no geostrophic flow on the sea floor, by extending isopycnals horizontally under the sea floor (Helland-Hansen, 1934; Sheng and Thompson, 1996), to address the calculated steric height over the sloping bottom. That gives the “topography corrected” steric height at location  $x_1$  with water depth  $-H_1$  referring to location  $x_0$  with a common water depth  $-H_0$

$$\eta'_{TC} = \int_{-H_1}^0 \alpha T'(x, y, z, t) dz - \int_{-x_0}^{-x_1} \alpha T'_b \frac{\partial H}{\partial x} dx \quad (3-9)$$

$$\eta'_{SC} = -\int_{-H_1}^0 \beta S'(x, y, z, t) dz + \int_{-x_0}^{-x_1} \beta S'_b \frac{\partial H}{\partial x} dx. \quad (3-10)$$

The above equations are equivalent to the steric setup adopted by *Csanady* [1979] that the path of integration is first along the sea floor from a reference depth to a given location then vertically up to the surface. The topography correction term, as pointed out by (Bingham and Hughes, 2012), is considered as an approximation to the bottom stress.

### 3.3 Temperature and Salinity Annual Cycles

The annual cycles of temperature and salinity were obtained using the method described in Section 3.2.2. In the thermal field (Figure 3.3A), the surface temperature shows strong seasonal pattern related to the annual heat flux cycle. The water column is well mixed in winter, and highly stratified in summer. The persistence of the cold bottom water at the middle shelf forms the cold pool in the process of stratification from April, and is gradually eroded as thermocline deepens around October and November. Besides the temperature difference within the same month, we also noticed different phase in the cycle (Figure 3.3B). The middle shelf surface layer water, at 10m depth with 60km offshore distance, reaches its peak in August. Whereas the bottom water gains highest temperature in October. The largest vertical temperature difference on the middle shelf occurs in August (~12°C). Our annual fitted temperature distribution show consistent pattern with one recent study (Forsyth et al., 2015) using the *Oleander* XBTs cross the shelf at a nearby location. The temporal evolution of the bottom temperature (Figure 3.3C) indicates the location of the cold pool water from April to September in the middle shelf.

In the salinity field (Figure 3.4A) the dominant feature is the nearshore and near surface freshwater from the shelf flow and local rivers (Chapman et al., 1986; Chapman and Beardsley, 1989; Fairbanks, 1982), with the summer offshore surface advection and dispersion (Sanders and Garvine, 2001; Yankovsky and Chapman, 1997). The surface and bottom salinity in the middle shelf are showing same pace leading the outer shelf (Figure 3.4B), which are probably related to the freshwater advection from the mean flow upstream. For the bottom salinity there is a steady salinity gradient from the coast to the outer shelf through all the season. Although the cold pool is sharing the same boundary in both thermal and haline fields with the slope water (shelf break front), the cold pool pattern is found mainly only in the thermal field. Thus we consider the surface expression of the cold pool, if it exists, comes from the thermal field.

### **3.4 Derived Steric Components**

The topography-corrected thermal steric height variation (Figure 3.5A) is derived as Section 3.2.4. Lower temperature generates depressed thermal steric height. Temporally, the thermal steric height is high in summer and low in winter, being consistent with the distribution of surface water temperature (Figure 3.3C), and thus is mostly controlled by the seasonal cycle of heat flux. A “wedge” pattern is remarkable with depressed height in the middle shelf around 50km offshore distance spanning from May to September, which co-locates with the cold pool revealed in the bottom temperature (Figure 3.3D). The forming of this wedge is possibly explained by the retention of the cold water in the middle shelf.

The salinity presents a seasonal pattern as well with lower haline steric height during the spring and summer (Figure 3.4C). Moreover, the distribution of the haline

steric height presents an elevated height in the middle shelf comparing with the inner and outer shelf, which is opposite to the “wedge” pattern in the thermal steric height distribution. Thus the haline pattern compensates the imprints of the thermal feature of the cold pool when further considering the total steric height. However, within the annual cycle (Figure 3.6) the thermal steric height ranges from -0.04m to 0.09m, while the haline steric height ranges from -0.03 to 0.02m. The lowest haline steric height and highest thermal steric height in summer (say, August) comes from shelf break front, related to the shelf/slope water exchange (Chapman et al., 1986; Fairbanks, 1982; Csanady and Hamilton, 1988). In the shelf, the haline steric height varies much less than the thermal steric height. Concerning the magnitude in each month, the thermal steric height is smaller than the haline steric height during May and June, suggesting that during these months the thermal features could be damped by the salinity distribution. While in July and August, especially the latter month, the thermal steric plays a major role in the total steric height (Figure 3.5 C). Moreover, the retrieved thermal steric height is also compared to the altimetry SLA, which is the 20-year averaged mean SLA annual cycle, with  $R^2 = 0.87$  suggesting that the thermal steric height explains 87% variation of the SLA. Considering this is a spatial-temporal comparison including all the transect locations, the high correlation coefficient between the thermal steric height and SLA indicates that these two variables are not only roughly temporally in phase but also spatially coherent. The cold pool feature, which exists in the thermal field with the depressed height in the middle shelf, can also be found in the SLA especially during July and August when the thermal steric height is much larger than the haline steric height.

### 3.5 EEMD and the Application

As analyzed in previous sections the cold pool feature is found in the 20-year mean altimetry SLA (Figure 3.5D). The altimetry SLA is the combination of components of different time scales, containing oscillations with spectrum ranging from one cycle per month to interannual. These components are damped out in the process of taking the 20-year average. One remaining question is whether and how the cold pool feature could be found from single-year altimetry data. Taking the year 2010 (Figure 3.8A) as an example, short time scale (1 to 2 month) disturbances are mixed with the cold pool feature, and causes the sea level anomaly to be elevated (March and November) or depressed (July). This makes the cold pool identification impossible. As the cold pool is an annual signal, we employ EEMD (Section 3.2.3) to decompose the SLA data into different frequency components and extract components with dominating annual signals to reconstruct the SLA field. Figure 3.8B shows the reconstructed SLA of 2010, which is one of many years that the middle shelf depressed height can be found in the reconstructed SLA.

Furthermore, the locations of SLA middle-shelf depression in the cross-shelf direction are identified year by year. Correspondingly, the cold core location can also be determined from in-situ measurements for those years with enough TS profiles (Figure 3.9). Temperature profiles from XBT and MBT are included for better spatial and temporal coverage. The location uncertainty of in-situ measurements is determined by the transect offshore resolution (15km), while the locations of SLA depression have an uncertainty around 25km considering both the original SLA 0.25° resolution ( $22.2km \times 21.3km$  at 40°N) and the inclined angle of the transect. We found general agreement between the SLA depression and the cold core locations. The cold core locations coincide with the SLA depression locations in 1993 and 1996. For the

years 1994, 2002, 2003, 2004 and 2009, the cold core locations are next to the SLA trough location within the uncertainty range. The inter-annual variation of the SLA depression locations show consistent pattern with the cold core locations during 1993~1996 and 2002~2004. These results suggest a promising application of the SLA data indicating the location of the cold pool. It should be noted that the SLA data within 25km offshore are subjected to land contamination thus the identified results should be treated with caution (e.g., the year 2007).

### **3.6 Discussion**

This study investigated the relationship between the cross-shelf sea level variation and the cold pool in the Middle Atlantic Bight for the first time. The persistence of the cold pool water generates depressed thermal steric height in the middle shelf. Co-located depression features are found in the annual evolution of the thermal steric height, total steric height and satellite observed SLA. The modulation of the sea level variations by the cold pool is revealed that the small variation induced by the cold pool overlies with the major seasonal cycle dominated by the solar heat flux.. This study provides insights into the composition of the sea level variations on the continental shelf, and thus contributes to the understanding of the response of the sea level variations to mesoscale water masses on the continental shelf.

Concerning the altimeter accuracy, the uncertainty of altimetry SLA is about 2cm (Cheney, 1994). In this study the altimetry data is averaged over 20 years with the standard error of the mean around 5mm (in August) as shown in Figure 3.10. The bottom temperature difference between 45km offshore and 120km offshore is around 4°C. The estimated thermal steric height over the same offshore distance is about 3.6 cm. The corresponding SLA difference is approximately 1.2 cm but the sea level

difference increases consistently by 3cm at 150km offshore and 5~6cm at 180km offshore. Thus the coherent pattern in the altimetry SLA data is not within the error bounds.

The contribution from the salinity field is investigated. The freshwater forms a narrow near surface band (Figure 3.4), expanding offshore in the surface layer in the summer time (Chapman et al., 1986). The annual variation of the haline steric height is much smaller than that of the thermal steric height (Figure 3.6), which explains the high correlation between the thermal steric height and the SLA (Figure 3.7). Concerning the magnitude of the haline and thermal steric heights in specific months, the haline steric height is of the same magnitude in the early summer (around June). This explains why cold pool features forms from May (Figure 3.3A) but the middle shelf depressed height is found after June especially in August in SLA (Figure 3.5). It should be noted that the influence of the haline field is location-specified. We also made transects downstream (figures are not shown here), which passes through the transport pathways of the Hudson River (R. Chant et al., 2008; Zhang et al., 2009). The annual variations of the haline steric height along those transects are of the same magnitude as the thermal steric height, and the squared correlation coefficients between the thermal steric height and SLA decreases correspondingly.

Processes of different temporal and spatial scales such as wind forcing (Li et al., 2014) could also influence the sloping sea level. Our primary interest is the influence of the cold pool, which occurs as one cycle per year. Thus we focus on the annual cycle of temperature and salinity, and adopt several data processing methods to eliminate oscillation signals of other time scales. The single annual harmonic fitting is applied to the TS profiles, and the fitted results are averaged over 20 years together

with the SLA data. EEMD, which can extract both seasonal and interannual variability from non-stationary signals, is not applicable to the TS profiles because the in-situ measurements are not continuous. Moreover, the influence of the cold pool to the thermal steric height and SLA is considered as a static effect (thermal expansion) in this study although the sea surface slope and cross-shelf density gradients are associated with an alongshelf geostrophic flow. Under our data processing steps (harmonic fitting, 20-year average and EEMD) the thermal steric height explains 87% variations of SLA. The dynamic processes including wind and waves could still contribute to the sea surface slope but are out of the scope of this study.

Our study investigates the cold pool modulation to the sea level slope and builds up a relationship between them. EEMD is applied to altimetry SLA to extract the annual cycle components so that the middle shelf depression can be found for single year's data without average. The locations of SLA depression (Figure 3.9) are consistent with the in-situ cold core locations, suggesting the linkage between these two variables and a promising application of altimetry SLA to the cold pool study, despite of large uncertainties due to the sparse of the in-situ measurements, SLA resolutions and coastal SLA errors. We noticed the locations of both the cold pool and SLA depressions show an agreement with the variation of the Labrador Current (LC) transport (Han et al., 2010): during the period 1993-1996, the Labrador Current transport anomalies first increased then decreased along with NAO index, while the cold pool locations moved offshore and then onshore. Similar pattern also occurred during 2002-2004. In the year 2000, the SLA trough moved further offshore around 140km, while the LC transport is not available but NAO index peaked. The cold pool variations are subjected to further investigation, but the linkage with LC transport and

NAO are possible recalling that the cold pool water is the retention of the cold shelf water coming from further north (Chapman et al., 1986; Fairbanks, 1982; Shearman and Lentz, 2009).

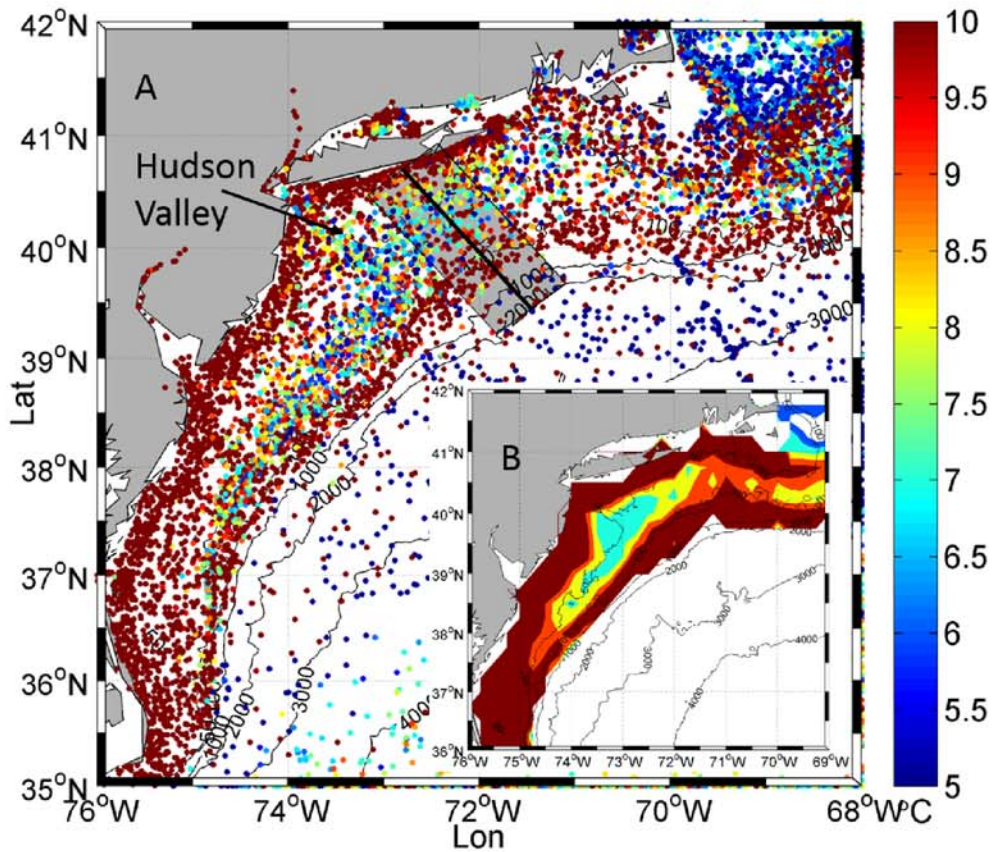


Figure 3.1. Cold pool spatial distribution. A. the scattered bottom temperatures from CTD and PFL profiles from May to September during 1993~2012. The black line in the grey rectangle is the cross-shelf transect, averaging over the shadowed rectangle. B. the contour of the bottom temperatures on the shelf indicating the location of the cold pool (with temperature  $< 10^{\circ}\text{C}$ ).

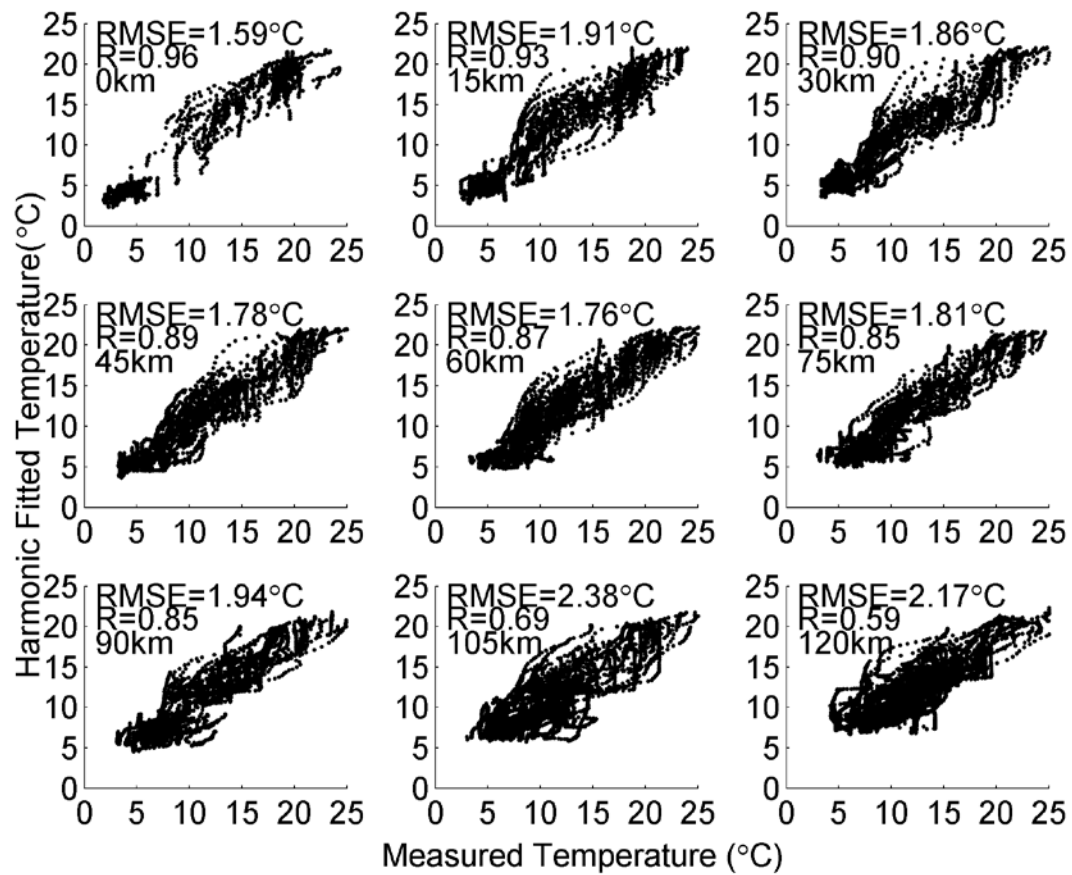
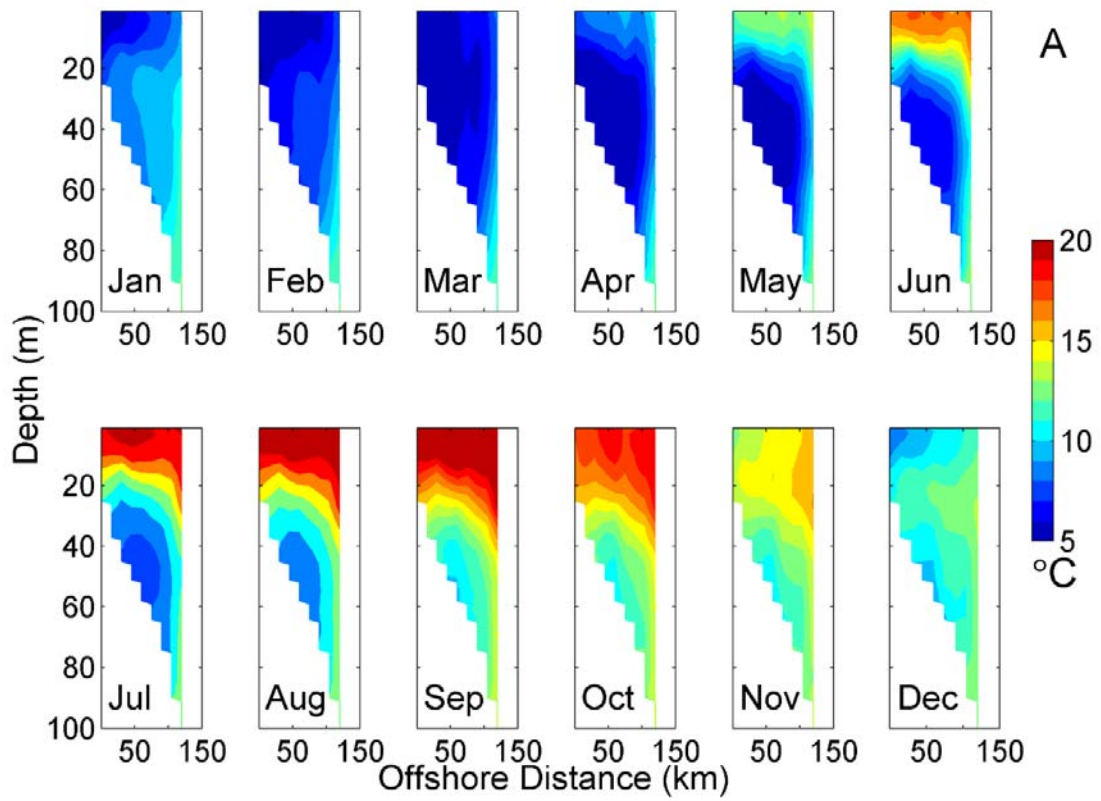
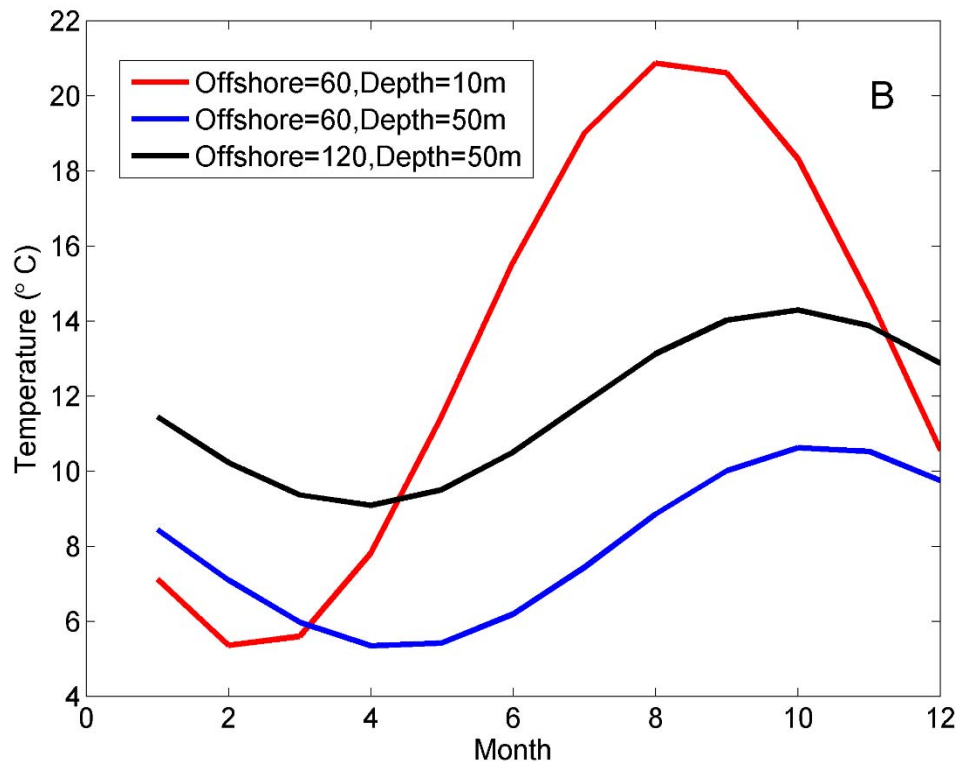


Figure 3.2. Temperature from harmonic fitting versus measured temperature at different offshore distance (0-120 km). Shown in each panel is the root-mean-square error (RMSE) and the correlation coefficients with  $p < 0.05$ .





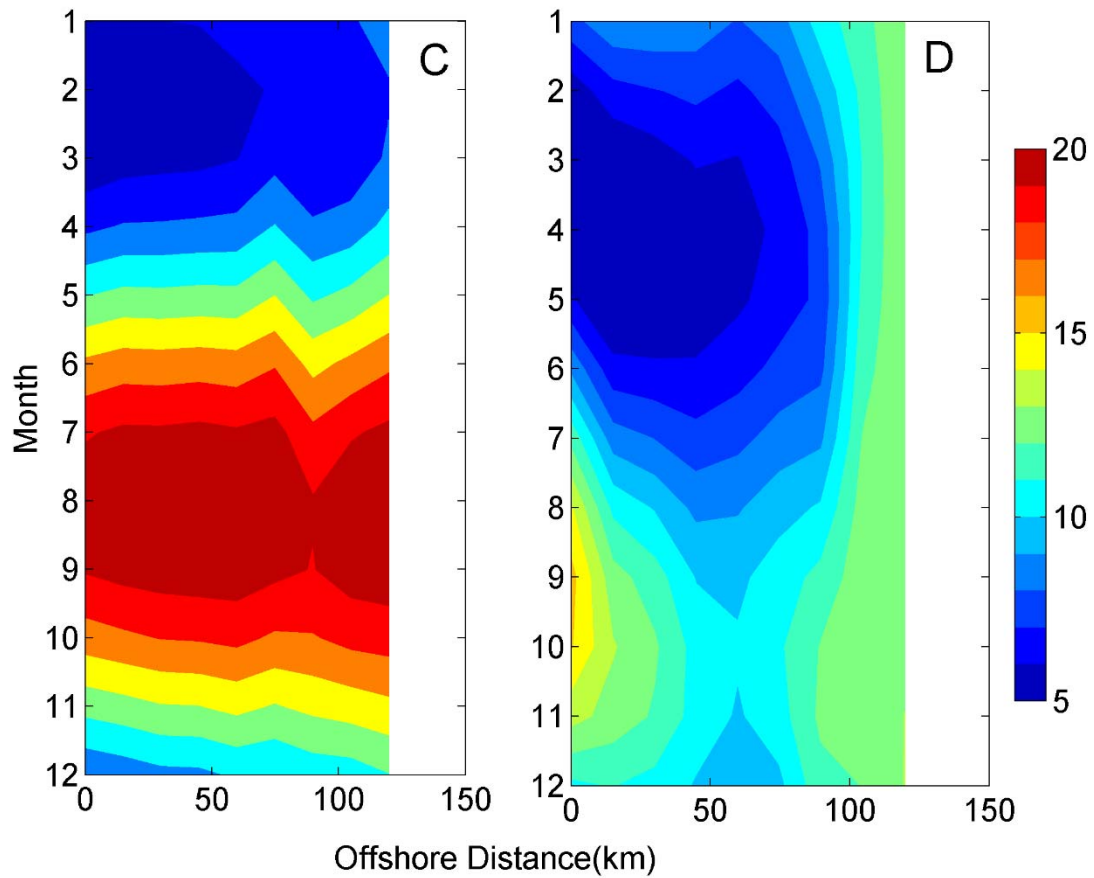
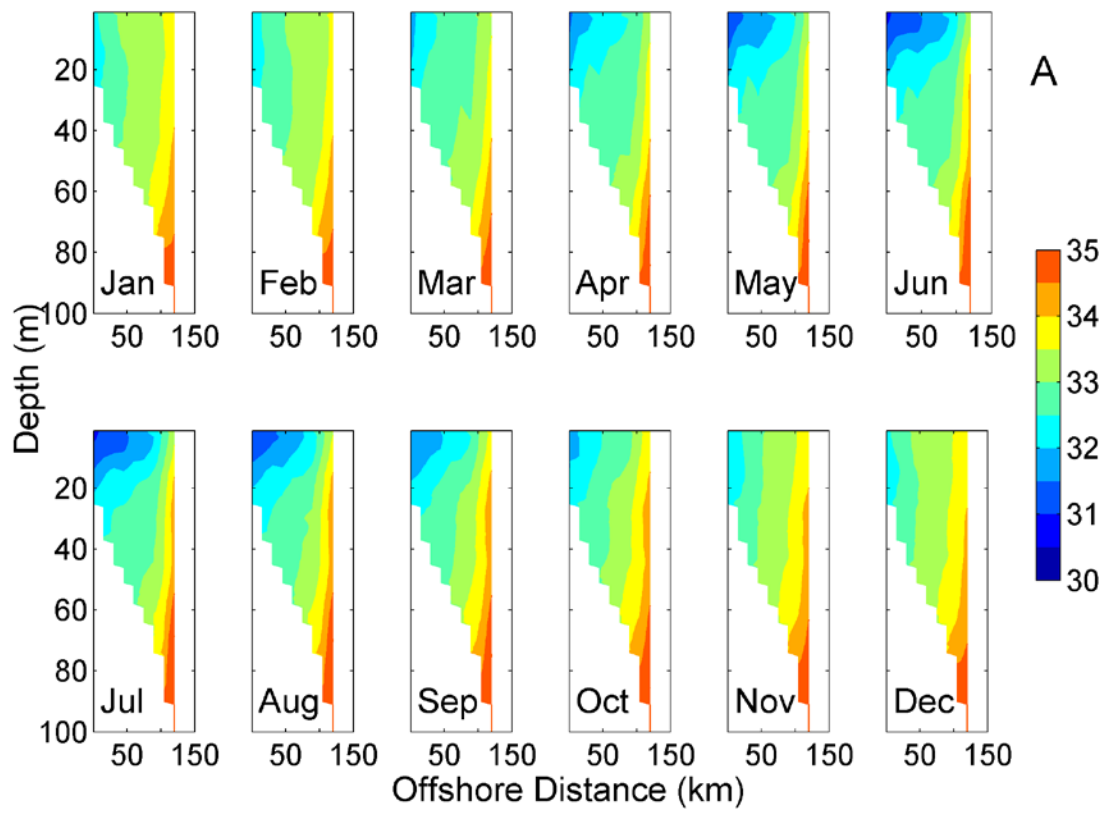
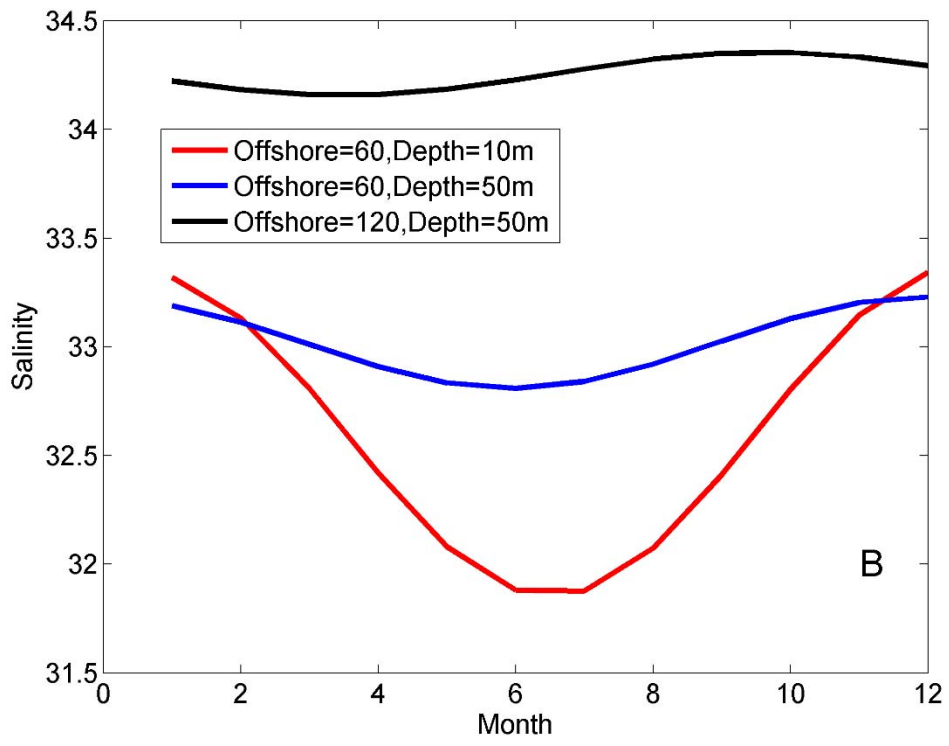


Figure 3.3. Temperature annual cycles along the transect. A. cross-section view of temperature (contour) in different months. B. temperature annual cycles at three locations: middle shelf surface (offshore distance = 60km, depth = 10m), middle shelf bottom (offshore distance=60km, depth = 50m), and outer shelf bottom (offshore distance =120km, depth = 50m). C. surface layer temperature annual evolution. D. Bottom temperature annual evolution.





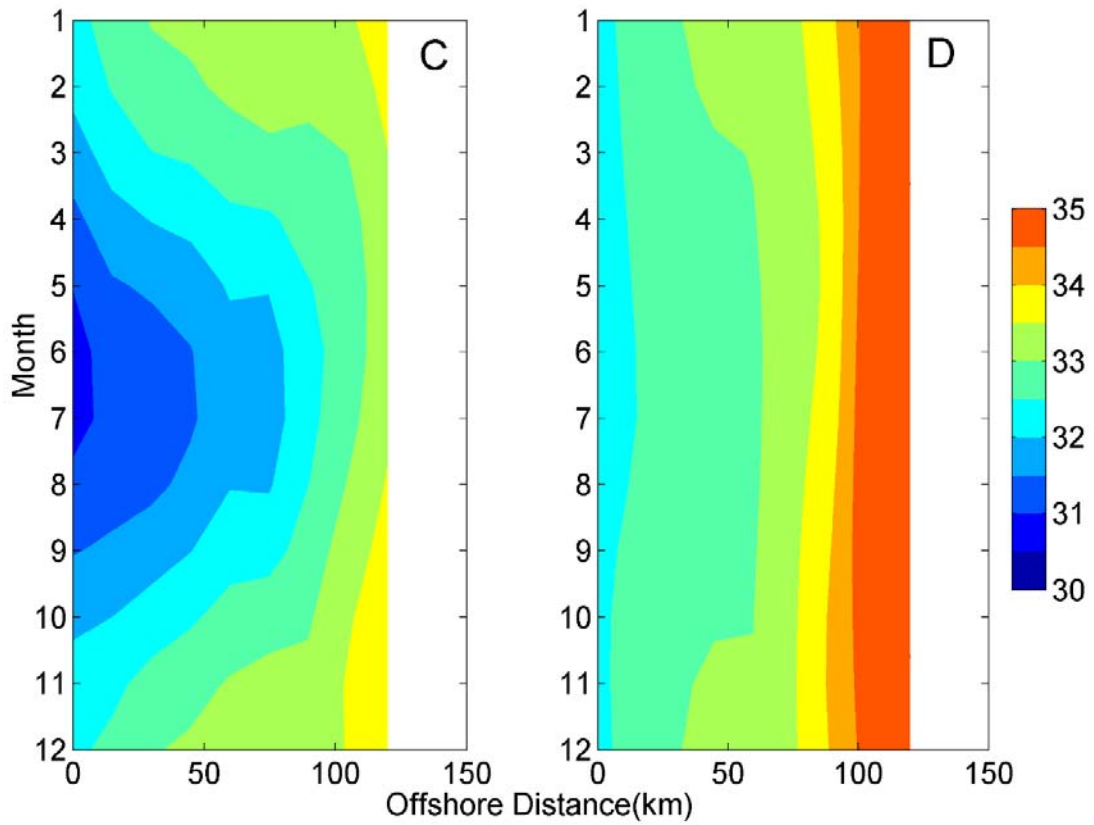


Figure 3.4. Salinity annual cycles along the transect. A. cross-section view of salinity in different months. B. salinity annual cycles at three locations: middle shelf surface (offshore distance = 100km, depth = 10m), middle shelf bottom (offshore distance=100km, depth = 50m), and outer shelf bottom (offshore distance =160km, depth = 50m). C. surface layer salinity annual evolution. D. bottom salinity annual evolution.

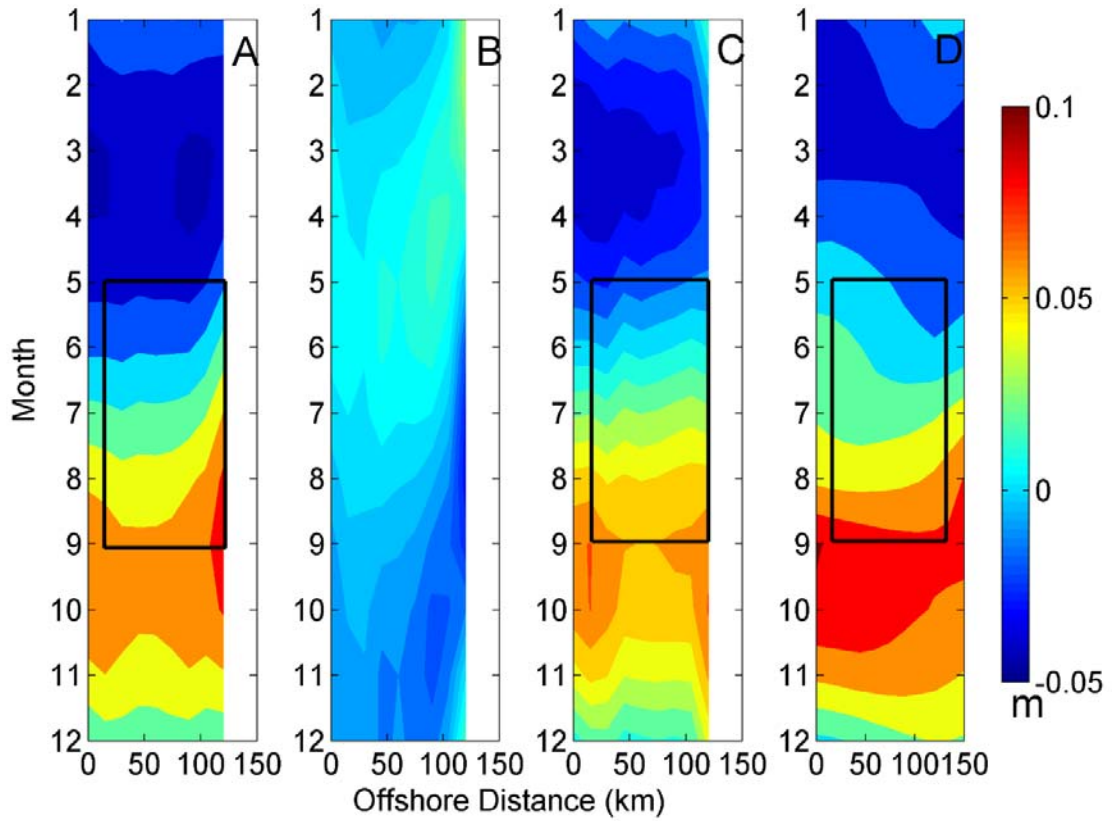


Figure 3.5. Annual evolution (contour) of different steric components and the monthly climatological altimetry SLA. From left to right: A. thermal steric height, B. haline steric height, C. total steric height and D. averaged altimetry SLA. The total steric height is the sum of thermal and haline steric components. The black rectangles in A, C and D are the central depressed pattern co-locating with the cold pool.

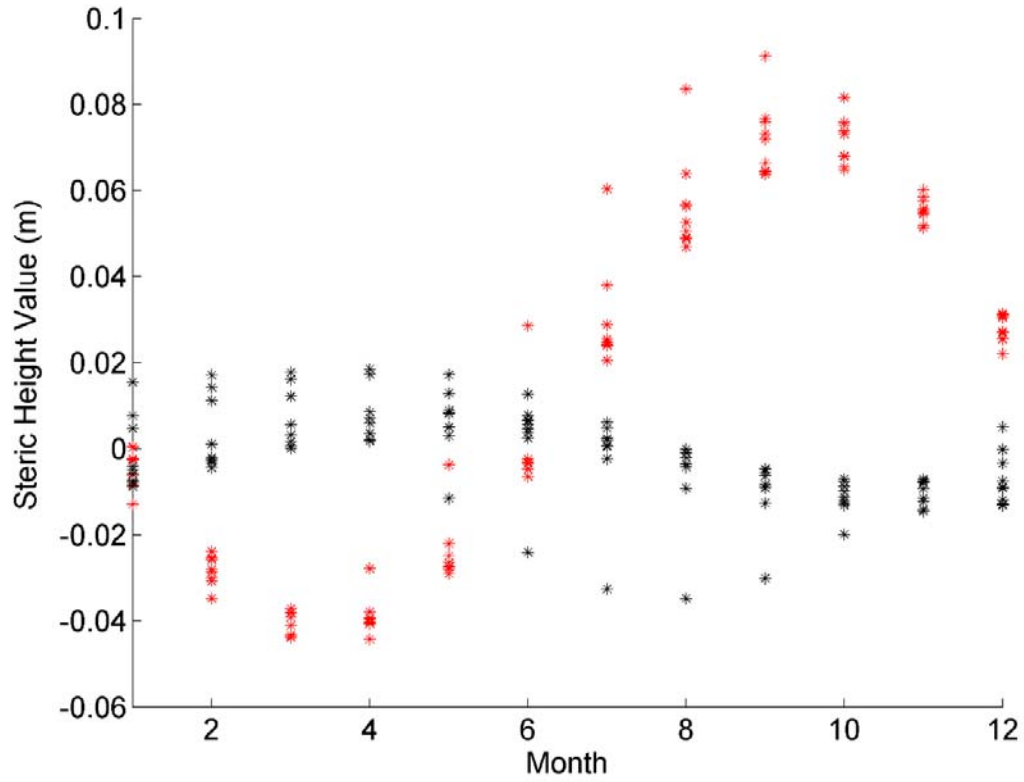


Figure 3.6. The comparison between the thermal steric height (red stars) and haline steric height (black stars) annual cycle.

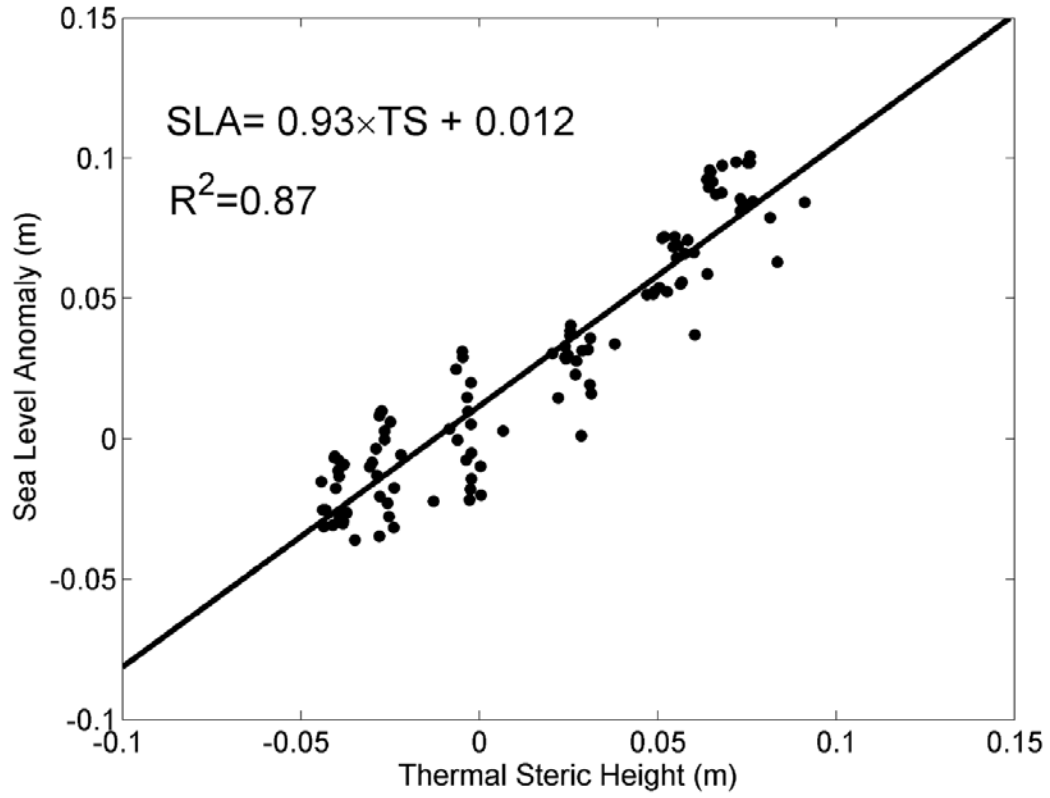


Figure 3.7. Derived thermal steric height versus altimetry SLA. The black line indicates the linear fitting.

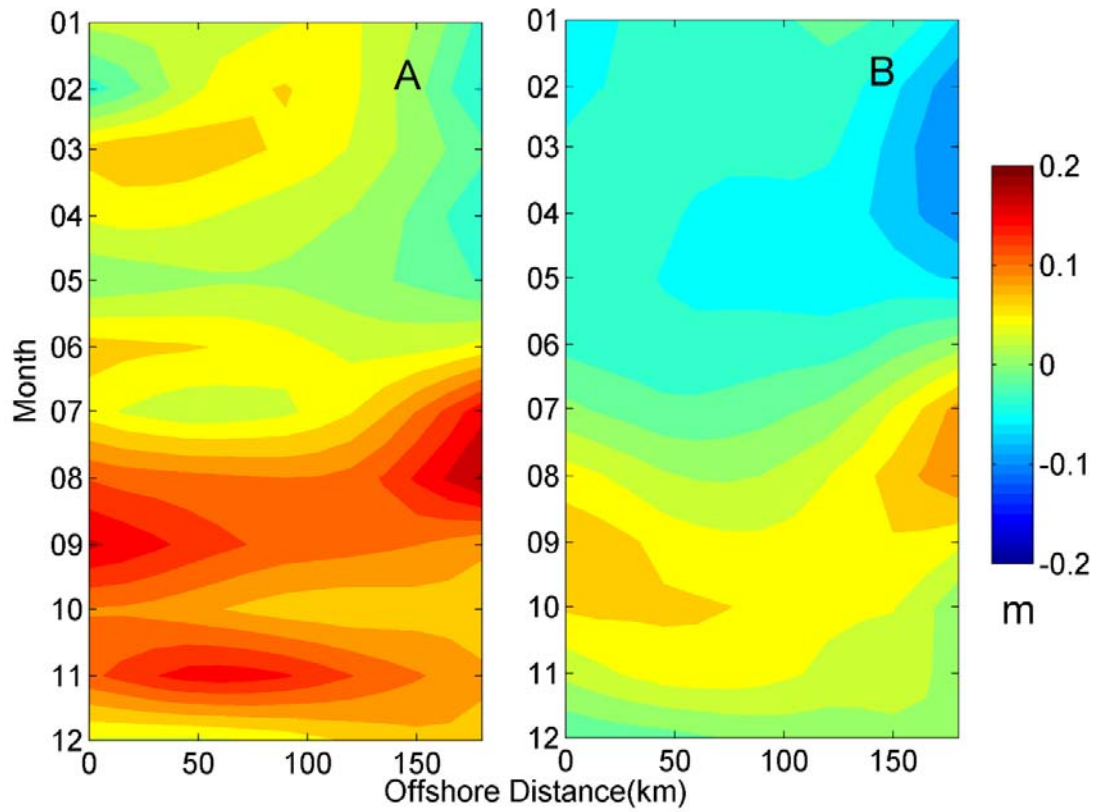


Figure 3.8. Comparison of altimetry SLA (A) and the seasonal components using EEMD (B) in 2010.

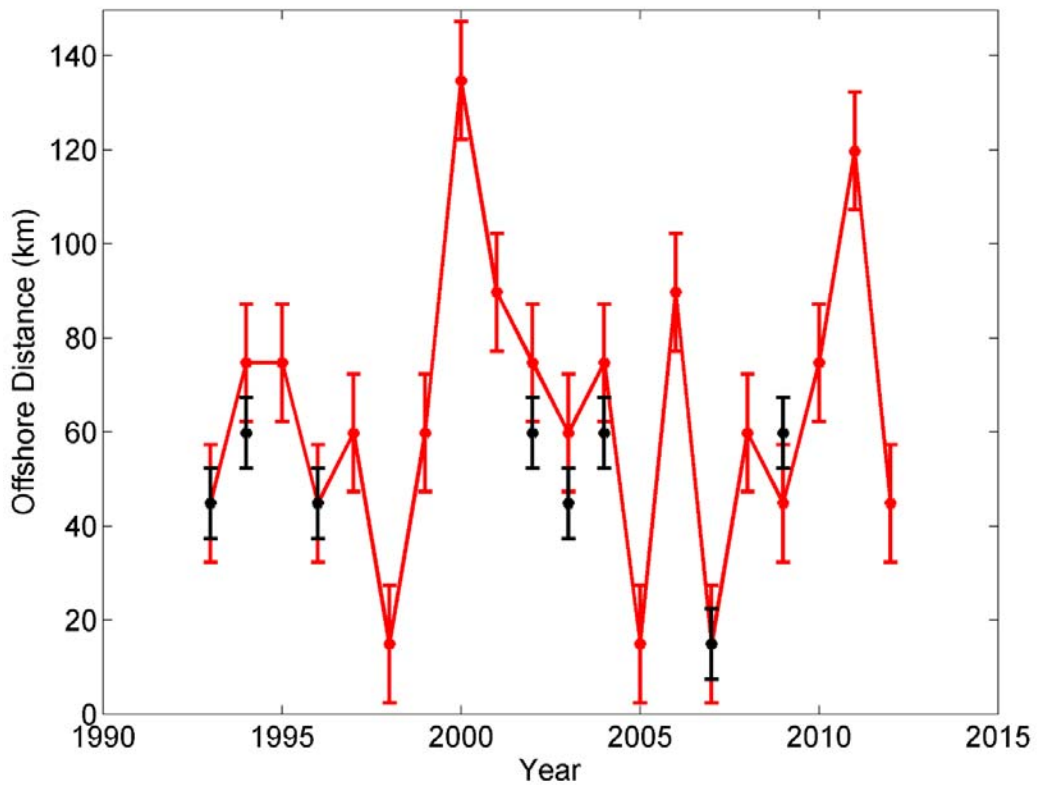


Figure 3.9. The location comparison in the offshore direction. The red dots are the locations of altimetry SLA depression, and the black dots are the locations of the cold core identified from in-situ measurements.

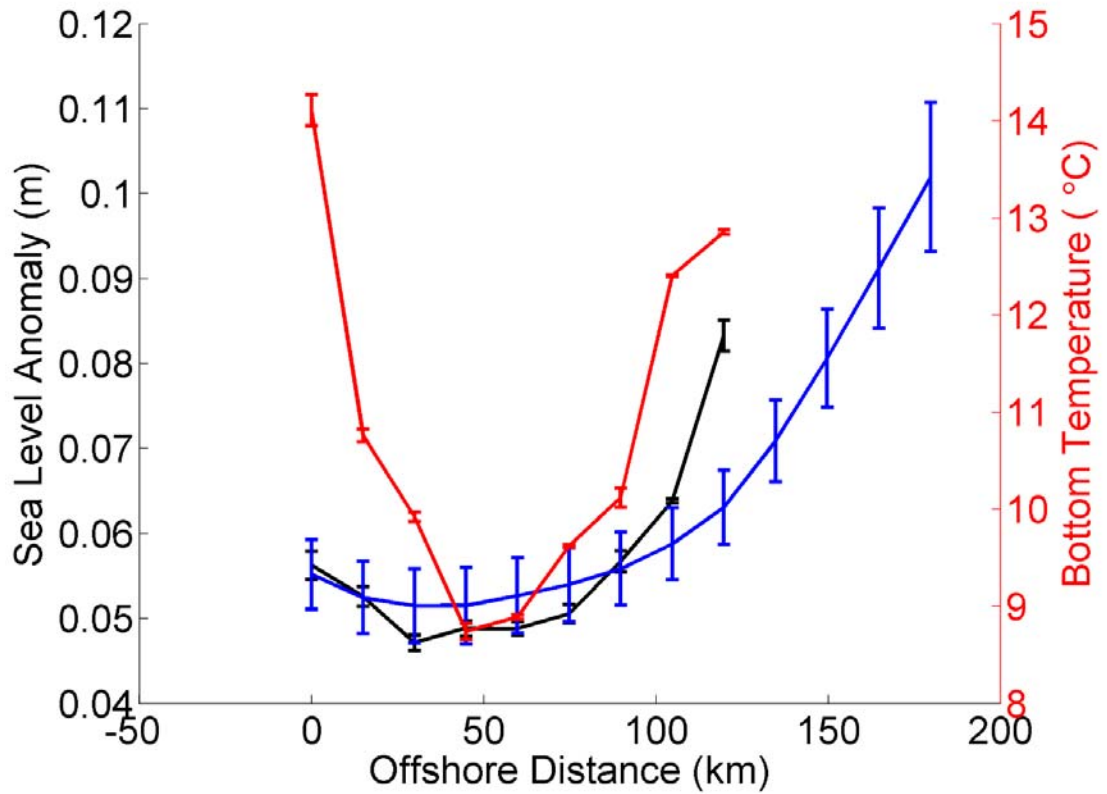


Figure 3.10. Comparison between the bottom temperature, corrected thermal steric height and altimeter SLA in August. The red line is the bottom temperature, black line is the derived thermal steric height, and the blue line is the SLA from altimeter. The error bar for each curve denotes the standard error of the mean.

## Chapter 4

### **THE HORIZONTAL HEAT ADVECTION IN THE MIDDLE ATLANTIC BIGHT AND THE INTERACTIONS AMONG DIFFERENT TIME SCALES**

#### **4.1 Introduction**

The heat advection plays important but different roles in the heat budget on different time scales. However, few studies discussed the interactions of different temporal components within the advection term. One exception is the study of Dong and Kelly (2004) in the Gulf Stream region. They found that the heat advection of the anomalous temperature by the mean current are the largest in the western Gulf Stream, and the advection of the mean temperature by the anomalous current are the largest elsewhere. If we can further decompose the SST and currents into components of different time scales, the response of the horizontal heat advection to the temperature and ocean currents, as well as the interactions among different temporal components, can be revealed in the Middle Atlantic Bight (MAB). In the context of the global climate change involving interannual, decadal and long term time scales, it is essential to understand the response of advection to different temporal variabilities, which is a contribution to the study of the ocean heat content in the continental shelf.

Measurements from satellite remote sensing, providing more than 20 years' continuous observations over the middle and outer shelf of MAB, give us a chance to investigate the variabilities within the horizontal heat advection on different time scales including sub-seasonal, seasonal, interannual and long-term variations and their relative contributions. Since satellite measurements adopted in this study (such as sea

level anomaly) are not appropriate for the inner shelf due to the land contamination and strong tidal currents thus our study area is the middle and outer shelf ranging from 30m isobath to 150m isobath with the inner shelf excluded. In this chapter firstly we calculated the heat budget in the shelf, and then decomposed the horizontal heat advection term into different time scales. Spectral analysis is applied to the decomposed modes. A summary and discussion are given in end.

## **4.2 Data and Method**

### **4.2.1 Data**

The high resolution Optimum Interpolation Sea Surface Temperature (OISST ver.2) is used, with a spatial grid resolution of  $0.25^\circ$  and a daily temporal resolution (Reynolds et al., 2007). Two SST analysis products can be obtained from National Oceanic and Atmospheric Administration/National Oceanographic Data Center (NOAA/NCDC). One product uses Advanced Very High Resolution Radiometer (AVHRR) infrared satellite SST data, from September of 1981 to present. The other uses AVHRR and Advanced Microwave Scanning Radiometer (AMSR) satellite SST data, from June 2002 to present. The coverage of SST products retrieved from IR instruments (AVHRR) are limited by the cloud, while SSTs from MW instrument (AMSR) have higher global coverage except within 75 km of land and during precipitation events. Thus the AMSR-AVHRR product have improved spatial resolution of SST gradient features compared with the AVHRR-only product. However, since our study area is mainly the continent shelf, and the AVHRR-only product can provide longer time series, we use AVHRR-only product. The total error

(standard deviation) for the AVHRR-only product close to the east coast of U.S. is around 0.4-0.6 °C (Reynolds et al., 2007).

To derive the sea surface absolute geostrophic velocities, we use the Maps of Absolute Dynamic Topography (MADT) data, one of Ssalto/Duacs multi-mission altimeter products released by AVISO/CNES. MADT is the sum of the sea level anomaly (SLA) and the mean dynamic topography (MDT) with a reference period of 20 years (1993 to 2012). This dataset contains daily maps from 1993 to 2014 on a 0.25° Cartesian grid with tidal and inverse barometer corrections. To avoid contamination from land, all data points within 25km from the coast should be excluded or analyzed with caution. The time-varying sea level are generally considered with an error of 2~3 cm (Cheney, 1994). As discussed by Han et al. (2014), this error translates to a root-sum-square error of  $0.042 \times g / f$  in the geostrophic transport anomalies with  $g$  being the gravitational acceleration and  $f$  being the Coriolis parameter.

To quantify the contribution of the wind-induced Ekman transport and the associated heat advection, we use the blended sea winds (Zhang et al., 2006) obtained from National Climatic Data Center (NCDC/NOAA), which contain monthly ocean surface wind currents and wind stresses on a global 0.25° grid from 1987 to 2011. The wind speeds were generated from multiple satellites while the wind directions came from NCEP Reanalysis 2.

The in-situ measurements used in this study come from the World Ocean Database (WOD 13), including the monthly temperature climatology and temperature profiles of Conductivity-Temperature-Depth (CTD), Profiling Floats (PFL), Expendable Bathythermograph (XBT), and Mechanical Bathythermographs (MBT)

from 1980 to 2014. As a comparison, the gridded subsurface temperatures of Simple Ocean Data Assimilation (SODA, (Carton et al., 2005)) from 1990 to 2010 are also employed. The SODA data is in version 2.2.4 and is obtained from Asia-Pacific Data Research Center (APDRC, University of Hawaii), which is a monthly data on  $0.25^{\circ} \times 0.25^{\circ} \times 40$  level incorporating WOA and satellite SST measurements. It should be noted that all above datasets are subjected to different temporal coverage and spatial grids. Thus in our study all the datasets (except in-situ temperature profiles) are linearly interpolated into monthly datasets with a spatial resolution of  $0.25^{\circ} \times 0.25^{\circ}$ .

#### **4.2.2 Estimation of the Mixed Layer Depth**

Different integration depth can be adopted when calculating the ocean heat content. Lentz (2009) used the whole water column in the shelf to evaluate the depth averaged heat balance. Dong and Kelly (2004) used time-varying mixed layer depth from a mixed layer depth model over the Gulf Stream region. Buckley et al. (2014) used a fixed-in-time depth from the maximum mixed layer depth in the open ocean. In our study, the upper ocean heat content is calculated by integrating from the surface to the climatological monthly mixed layer depth (MLD) determined from the in-situ measurements. By adopting such MLD we can use SST as the approximation of the mixed layer temperature (MLT) assuming that the water is vertically well mixed in the mixed layer. Grodsky et al. (2008) made a comparison between the SST and the MLT, showing that globally and time-averaged MLT is cooler than SST by approximately  $0.1^{\circ}\text{C}$  with extreme values of  $0.8^{\circ}\text{C}$  at eastern equatorial Pacific. The MLD is determined as the shallowest depth where the potential density increases by  $0.0125 \text{ kg/m}^3$  from the surface (Christensen and Pringle, 2012; Deser et al., 2003; Dong and Kelly, 2004). The surface density is defined as the shallowest available measurements

within 10m at each location. The differences of using SST and SODA as MLT and using different mixed layer depth are further discussed in Section 4.6.

### 4.2.3 Estimation of the Shelf Currents

The ocean currents are the combination of several components (Dong and Kelly, 2004; Han et al., 2010). The sea surface geostrophic currents corresponding to the sloping sea surface can be derived from the geostrophic balance. In the interior of the water column, the density gradient, which influences the pressure gradient, generates the velocity shear. Following Han et al. (2010), we use the sea surface as the reference level, thus the total geostrophic current at any depth  $z$  is given by

$$\begin{aligned}\vec{u}_g(x, y, z, t) &= \frac{g}{f} \vec{k} \times \nabla_h \eta(x, y, t) + \frac{g}{\rho_0 f} \int_{-z}^0 \nabla_h \rho(x, y, z, t) dz \\ &= \vec{u}_{slope} + \vec{u}_{shear}\end{aligned}\quad (4-1)$$

where  $\eta$  is the sea surface slope from the altimeter,  $g = 9.8m/s^2$ ,  $f = 9.35 \times 10^{-5} s^{-1}$  and reference density  $\rho_0 = 1025kg/m^3$ . We divide the geostrophic current into the depth-independent (barotropic) component  $\vec{u}_{slope}$ , which is corresponding to the sloping sea surface slope, and depth-dependent (baroclinic) component  $\vec{u}_{shear}$ , which is associated with the subsurface density gradient. Moreover, we take the wind-induced Ekman current into consideration. It should be noted that the wind can also setup sea level variation (Li et al., 2014) to influence the surface geostrophic current which has been included in the geostrophic current. Thus we here only consider the Ekman part due to the wind. The wind induced Ekman current is negligible in the Labrador current system (Han et al., 2010) considering the whole water column but is necessary to be investigated for the upper layer. Assuming the wind's influence is confined within the upper mixed layer, the depth-averaged wind current can be approximated as

$$\vec{u}_{wind} = \frac{1}{\rho_0 f} \left( \frac{\tau_y(x, y, t)}{H_{upper}(x, y, t)}, -\frac{\tau_x(x, y, t)}{H_{upper}(x, y, t)} \right), \quad (4-2)$$

where  $(\tau_x, \tau_y)$  is the sea surface wind stress. Thus the total ocean currents are given as

$$\vec{u} = \vec{u}_{slope} + \vec{u}_{shear} + \vec{u}_{wind}. \quad (4-3)$$

#### 4.2.4 Estimation of the Upper Ocean Heat Budget

In a right-handed coordinates where  $x$  to the east,  $y$  to the north and  $z$  is positive upward, the heat budget averaging over the upper MLD  $H(x, y, t)$  is

$$\left\langle \frac{\partial T(x, y, z, t)}{\partial t} \right\rangle + \left\langle \vec{u} \cdot \nabla T(x, y, z, t) \right\rangle = \left\langle \kappa \nabla^2 T(x, y, z, t) \right\rangle + R \quad (4-4)$$

where  $\langle \bullet \rangle = \frac{1}{H(x, y, t)} \int_{-H(x, y)}^0 \bullet dz$  means the vertical average. The temporal  $\left(\frac{\partial T}{\partial t}\right)$

and the spatial  $(\nabla^2 T)$  variations of the temperature can be derived from SST as an approximation of the MLT.  $\vec{u} \cdot \nabla T$  is the horizontal non-linear advection. Corresponding to the three components of the ocean currents, the advection term in the heat budget is also the sum of three components: the horizontal advection associated with the sea surface slope, the horizontal advection associated with the subsurface density gradient, and the horizontal advection due to wind-driven Ekman transport. Hereafter we call them the slope advection, the shear advection and Ekman advection respectively.  $\kappa \nabla^2 T$  is the horizontal diffusion where  $\kappa = 2000 m^2 / s$  following Dong and Kelly (2004). As our interest here is the role of the horizontal advection, we attribute the contribution of all other processes, including the vertical exchange with the air and bottom layer, as the residual term  $R$  in the heat balance equation. The advection term can be viewed as the remote forcing to the heat content variation while residual term can be considered as the local forcing.

#### **4.2.5 Fast Multi-Dimensional Ensemble Empirical Mode Decomposition (FMEEMD)**

The original Empirical Mode Decomposition (EMD) (Huang et al., 1998) is a useful tool for the nonlinear, nonstationary time series, separating the dataset into a finite number of intrinsic mode functions (IMFs). The method identifies different oscillation cycles based on their characteristic temporal scales. The number of IMFs is determined by the length of the dataset. To eliminate the mode-mixing phenomenon with the original EMD, an improved approach Ensemble Empirical Mode Decomposition (EEMD) (Wu and Huang, 2009) is proposed by adding white noise into the data and treating the mean of a sufficient number of trials as the final result. Afterward, Multidimensional EEMD (MEEMD) (Wu et al., 2009) and Complementary EEMD (CEEMD) (Yeh et al., 2010) are developed respectively. One most recent improvement is the Fast Multidimensional Ensemble Empirical Mode Decomposition (FMEEMD) (Feng et al., 2014). Using principal component analysis (PCA), the multidimensional climate data can be decomposed into principal component (PCs) and corresponding empirical orthogonal functions (EOFs). Then the MEEMD is applied only to a small fractions of PCs so as to address the time consuming and data compression problems when processing gridded climate data. This method is validated by analyzing the extended reconstructed sea surface temperature (ERSST). In this study, we applied the FMEEMD to decompose the continuous remote sensing datasets (e.g., SST and MADT) into oscillations of different time scales.

#### **4.2.6 Temporal Decomposition of the Horizontal Heat Advection**

The horizontal advection term is non-linear and associated with the variations of both variables (i.e., the ocean currents and the water temperature). We apply the

temporal decomposition to each variable in the advection to investigate the interactions among multiply time scales. For simplicity, only the very surface layer (say, 5m) is considered thus SST and surface geostrophic currents derived from MADT can be used without vertical integration (thus the unit of the advection term is °C/s). Only the slope advection due to the sloping sea surface is considered since it is the dominant component as analyzed later. FMEEMD decomposes each variable into a sum of sets of oscillations on different time scales. Combining certain modes gives

$$Advection = \vec{u} \cdot \nabla T = \left( \sum_{i=1}^5 \vec{u}_i \right) \cdot \nabla \left( \sum_{i=1}^5 T_i \right) \quad (4-5)$$

where  $i=1,2,3,4,5$  representing the sub-seasonal (<1 cycle/year and >6 cycle/year) seasonal (1 cycle/year), interannual (0.1-1 cycle/year), long-term (less than 0.1 cycle/year without the mean), and mean components respectively. The modes below 95% significant level in FMEEMD are excluded. Limited by the length of time series (SST: 1981-2014, MADT: 1993-2014) we are not able to distinguish multi-decadal oscillations with period longer than 10 years. Thus the long term component mainly is multi-decadal and longer time scale variations, as the residual by subtracting the sub-seasonal, seasonal, interannual and mean modes from the original data. By applying the temporal decomposition, the advection term is decomposed into 25 components (Table 4.1) among which 24 are oscillations of different magnitudes and 1 component is constant.

The contribution of each temporal component can be quantified based on the variance. If we define a contribution factor

$$C_{ij} = \frac{Var(\vec{u}_i \cdot \nabla T_j)}{\sqrt{\sum_{i=1}^5 \sum_{j=1}^5 Var^2(\vec{u}_i \cdot \nabla T_j)}} \quad (4-6)$$

where  $Var$  is the variance of each mode in the temporal decomposition. This gives

$$\sum_{i=1}^5 \sum_{j=1}^5 C_{ij}^2 = 1 \quad (4-7)$$

thus  $C_{ij}^2$  can be shown in the form of percentage. The meaning of  $C_{ij}^2$  is the square of each component's variance representing the oscillation energy normalized by the squared sum of all variances or total energy. It should be noted that since  $C_{ij}^2$  is using the squared variance, the ratio of the contribution percentages of two components is proportional to the ratio of squared variances.

### 4.3 The Role of the Horizontal Heat Advection in the Heat Budget

The MAB heat budget within the upper mixed layer is reconstructed (Figure 4.1) by using SST to approximate the MLT. The advection term is calculated as described in Section 4.2.3. Strong seasonal oscillations are found for the temporal variation of the temperature and the residual term. The correlation coefficient between the temporal and the residual term can be evaluated at each location, with a mean of 0.83 ( $p < 0.05$ ). The diffusion term is about 2 order smaller than other terms, suggesting that diffusion plays little role in the heat content variation in the shelf thus is negligible. The advection term, though shows seasonal variability somehow, has much smaller amplitude and out of phase with the other terms. For most locations there is no significant correlation between the temporal term and the advection term. Our results suggest that the seasonal variation of the heat content is dominated by the local vertical heat flux rather than the horizontal heat advection, which is consistent with previous studies as reviewed in Section 1.4. We noticed that the values of the  $(-1) \times$  advection term is mostly negative, ranging from  $0.3 \times 10^{-6} \text{ } ^\circ\text{C/s}$  to  $-1 \times 10^{-6} \text{ } ^\circ\text{C/s}$ . The negative values imply that the role of the horizontal advection causes a heat loss to the upper ocean heat content. This is not surprising by recalling that the mean current in

the shelf is from northeast to the southwest (Lentz, 2008a). The horizontal advection transport colder water upstream southward, causing the decrease of the temperature.

FMEEMD, as described in Section 4.2.5, can be applied to each term in the heat budget equation. Using the decomposed modes of different time scales, the interannual (0.1 cycle/year to 1 cycle/year) and the long term ( $<0.1$  cycle/year but without the mean) signals are reconstructed, and the location by location correlation coefficients distribution between the temporal term and the other two variables (the adv. and residual term) can be evaluated (Figure 4.2). The residual (i.e., the vertical heat flux) is no longer the dominant factor in the temporal variation after removing the seasonal cycle. The relationship between the temporal term and the residual is weaker as concerning longer time scales, while the relationship between the temporal term and the advection becomes stronger as time scales become longer. The temporal term can then be explained as the competition/balance between the vertical heat flux and the horizontal heat advection. Neither the vertical or horizontal heat flux could solely dominant the ocean heat content in the shelf. Our results agree with previous studies that the ocean heat content is partially due to surface heat flux (Mountain, 2003) and partially influenced by the horizontal advection (Connolly and Lentz, 2014), but differ from the conclusion of Dong and Kelly (2004) in the Gulf Stream region that the interannual variations in the upper ocean heat content are dominant by the advection-diffusion term. This is very likely because of the much stronger currents in the Gulf Stream region than in the shelf thus the advection plays a much stronger role in their study area through all the time scales.

#### 4.4 Components of the Horizontal Heat Advection

As described in Section 4.2.4, the horizontal heat advection contains slope advection, shear advection and Ekman advection resulting from different driving mechanisms. The domain-averaged three components are shown as in Figure 4.3. The mean value of these components are  $2.2 \times 10^{-7} \text{C/s}$ ,  $-0.6 \times 10^{-7} \text{C/s}$  and  $3.0 \times 10^{-7} \text{C/s}$  respectively, with the variances being  $2.3 \times 10^{-7} \text{C/s}$ ,  $0.09 \times 10^{-7} \text{C/s}$  and  $3.4 \times 10^{-7} \text{C/s}$  respectively. The Ekman advection has the largest mean and variance. This suggests that in the upper layer the wind-induced Ekman currents play an important role in the heat advection. We also tested the advection over the whole water column (figure not shown here), and found that the slope advection then becomes the strongest factor and the shear advection is the secondary. Thus the wind's influence is limited in the Ekman layer. The mean values of the slope and Ekman advection are positive, suggesting that the surface geostrophic currents and the wind-induced currents cause heat loss to the shelf upper layer by either transporting colder water to the shelf or carrying the warmer water away from the shelf, while the shear advection causes heat gain by bring warmer water into the shelf.

The spatial distribution of the relative magnitudes of the three advection components is evaluated by calculating the correlation coefficients between the total advection and each component at different locations (Figure 4.4). Those locations without significant correlation relationship ( $p > 0.05$ ) have been excluded in the figures. The slope advection is highly correlated with the total advection for most of the shelf except the New England shelfbreak and the New Jersey shelf. For the shear advection, we found that the correlation coefficients are mostly negative, especially in the region of Hudson Valley. This is consistent with the negative mean value of the shear advection, which is to the opposite direction of the other two advection components.

For the Ekman advection, the correlation coefficients are high in the New England shelfbreak areas and the New Jersey shelf. The role of the wind will be further discussed in Section 4.6.

#### **4.5 Temporal Components of the Heat Advection**

The temporal decomposition can be applied to the slope advection and Ekman advection respectively. SST is assumed to represent the MLT. The geostrophic currents from MADT is the depth-independent component of the geostrophic currents, which is the dominant factor within the upper MLD together with the Ekman currents. Thus the results here represent the advection within the upper MLD.

For the slope advection, which is associated with the surface geostrophic currents, the domain-averaged time series of the decomposed components are shown in Figure 4.5. One component generated from the temporal-mean temperature and temporal-mean currents is constant ( $2.76 \times 10^{-7} \text{ }^\circ\text{C/s}$ ). Other components are subjected to different variances. To quantify the contribution of each component, we introduce a contribution factor (Section 4.2.6) representing the energy portion and summarized the results in Table 4.1. The largest three components are: the seasonal temperature by the mean current, the mean temperature by the sub-seasonal current, and the seasonal temperature by the sub-seasonal current, which account for 80% of the total energy. In addition to these three components, the secondary components are those containing seasonal or mean temperature, and sub-seasonal or mean current, making up about 19.2% of the total energy. All other components contribute to the rest.

The different variances or energy of the decomposed components can be explained by the spectrum distribution of the temperature and the surface geostrophic currents (Figure 4.6 A and B). The annual component is the dominant factor in SST

(besides the mean). For the surface geostrophic currents, the interannual and annual signals are strong. However, multi-peaks are found for the sub-seasonal portion. The spectral distribution of the SST and surface geostrophic currents are consistent with the energy contribution revealed in Table 4.1 (Column Sum and Row Sum), where the sub-seasonal and mean currents contributes 56.1% and 29.8% of the total variance, while the seasonal and mean SST contributes 75.5% and 17.6% respectively.

The decomposed components are also investigated in the frequency domain. The interaction with the mean of one variable, which is constant, can retain the spectrum of the other variable. For the rest of the components, the interaction between the two variable generates new frequency components. One example is the advection due to seasonal temperature and seasonal geostrophic currents (Figure 4.7 A), the spectrum of which contains two peaks of interannual and semi-annual oscillations respectively, while the amplitude is much lower at 1 cycle/year frequency. The advection associating with the seasonal temperature and seasonal currents is no longer seasonal signal.

Similar analysis can also be applied to the Ekman advection (Table 4.2). For the Ekman advection, the largest components come from the seasonal temperature by the mean currents, and the seasonal temperature by the seasonal currents, contributing 65.6% together to the total energy. The interaction between the seasonal temperature and seasonal currents also generate two peaks (Figure 4.7 B) with the largest semi-annual signal.

## **4.6 Discussion**

In this study, the role of the horizontal advection in the upper ocean heat budget over the MAB is quantitatively investigated. On the seasonal scale the

temperature variation is controlled by the vertical heat flux while on the longer time scales it is the balance between the vertical heat flux and horizontal heat advection that determined the temperature variation, which is consistent with the mean condition over the shelf (Lentz, 2009). In the calculation we used SST to represent the surface mixed layer temperature, and the integration depth is chosen as the time varying MLD determined from SODA data. Regarding the chosen of the MLD and the MLT, a cross-comparison is made for the depth-averaged temporal heat variation with different MLDs (the in-situ monthly climatological MLD, SODA time varying MLD and SODA monthly climatological MLD) and different MLTs (SST and SODA). As shown in the cross-comparison results (Figure 4.8), all curves shows similar seasonal variabilities. With MLT from SST, using different MLDs have almost identical curves. With MLT from SODA data, using time varying MLD and climatological MLD are identical, which are larger than using in-situ climatological MLD in the summer. This indicates that the MLD is mainly a seasonal variation, or to be more accurately, the interannual variability of MLD does not make significant contribute to the upper ocean heat content in the shelf. The temporal variation using SST is higher in the summer and lower in the winter than the SODA data, with standard deviations ranging from  $1.7 \times 10^{-7} - 2.1 \times 10^{-7} \text{ } ^\circ\text{C} / \text{s}$ . This suggests that using SST as MLT has larger annual variation than using the SODA MLT, though it is still not clear which MLT is better. Another comparison is also made by removing the seasonal cycle using FMEEMD. The interannual variability (together with longer time scale variability) are still consistent with different MLTs (with correlation coefficients being larger than 0.7).

The relative contributions of the geostrophic currents and the wind-induced Ekman transport are investigated at different locations. Previous studies found that the role of the wind is subject to regional differences. In the upstream regions, Han and Tang (2001) concluded that the wind-driven Ekman transport is negligible in the Labrador Current volume transport in the western Labrador Sea. However, Han (2005) revealed that the wind forcing contributes significantly to the inshore branch of the Labrador Current but less to the shelf-edge branch over the Newfoundland and Labrador Shelf using model simulation. Li et al. (2014) focused on the Nova Scotian Shelf- Gulf of Maine region and found significant correlation on the interannual time scale among the sea level slope, the alongshelf flow and the alongshore wind stress. Andres et al., (2013) also suggests that the along-shelf wind stress will lead to a sea level variance on the interannual time scale. Within the New Jersey Shelf, the wind forcing has long been discussed related to the buoyant river outflow, coastal upwelling and offshore transport (e.g., Kohut et al., 2004; Glenn et al., 2007; Jiang, 2008; Dzwonkowski et al., 2009; Sha et al., 2015). In the Gulf Stream region, Dong and Kelly (2004) suggested that within the advection term of the heat budget, the largest variation comes from the geostrophic advection anomaly rather than the Ekman advection. What we found in the MAB is that the wind-induced Ekman transport is as large as the surface geostrophic currents in the surface layer especially for the New Jersey shelf and the New England shelfbreak. When considering the whole water column, the wind's role will be the least comparing to the sloping sea surface and the density gradient. Sha et al. (2015) reported that the wind stress is correlated with the sea surface currents retrieved from HF radar on daily basis but confines within the

southern New Jersey shelf. Using monthly-averaged wind stress and absolute geostrophic currents we got consistent pattern here but in a much larger spatial scale.

The interactions among different time scale oscillations in the heat advection are quantitatively assessed. Using temporal decomposition, the horizontal heat advection term, taking the slope advection as an example, can be decomposed into components including one constant mean and oscillations on different time scales. The relative amplitudes of the components depend on the spectrum distribution of the temperature and the ocean currents. The mean and the seasonal signals are the strongest for the temperature, while sub-seasonal and mean components are strongest for the surface geostrophic currents. It is shown here that the sub-seasonal signal of the surface geostrophic currents takes a large portion (56.1%) to the total advection. This is consistent with previous studies that the horizontal heat advection is dominant on time scales of weeks to months. It should be noted that there are new frequency components generated in the non-linear advection term. For example, the interannual variability for the whole horizontal heat advection not only contains the contribution from the interannual temperature by the mean currents and the mean temperature by the interannual currents, but also contains the seasonal temperature by the mean currents, the long term temperature by the seasonal currents, and the long-term temperature by the interannual currents. This implies that the influence of one variable's oscillation is not confined within specific spectral band in the heat flux budget. Moreover, the interaction between the seasonal temperature and seasonal currents can generate semi-annual oscillations. The heat advection can influence the total heat budget and thus modify the variation of the temperature. The interactions

between different time scale variables are one of the possible explanation of the semi-annual cycle of the SST.

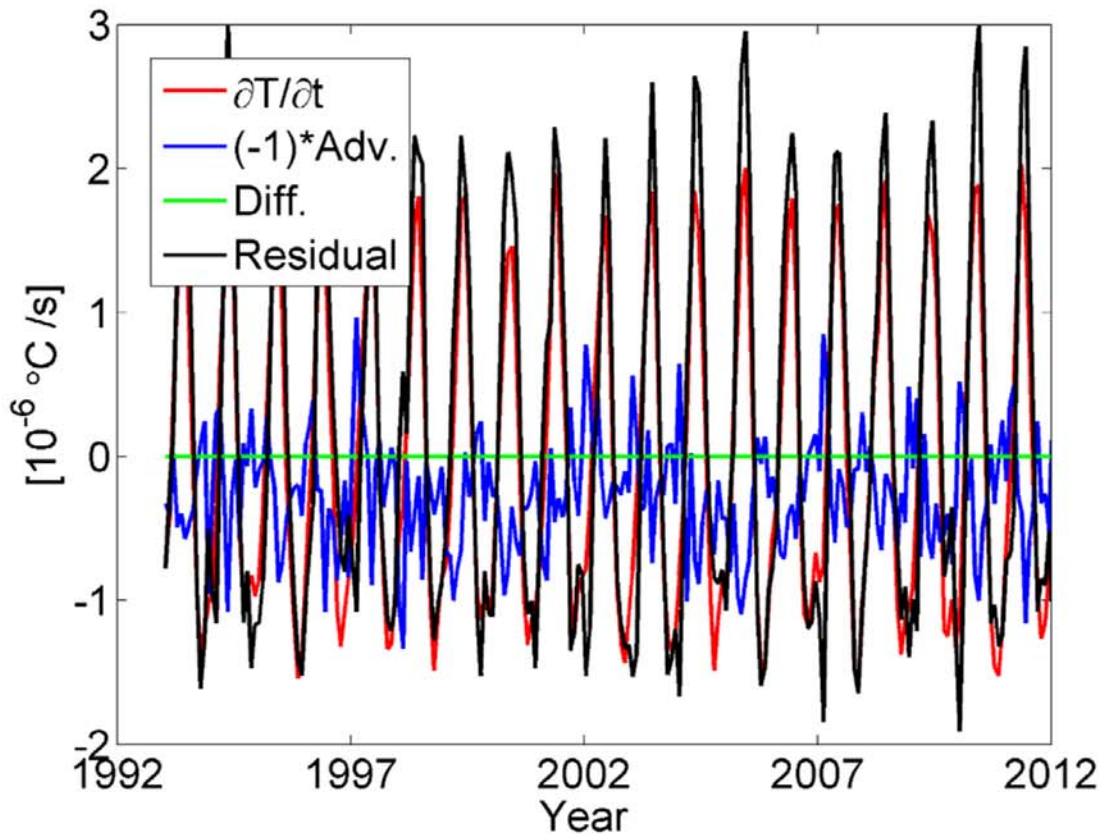


Figure 4.1. The heat budget in the Middle Atlantic Bight averaged over the mixed layer.

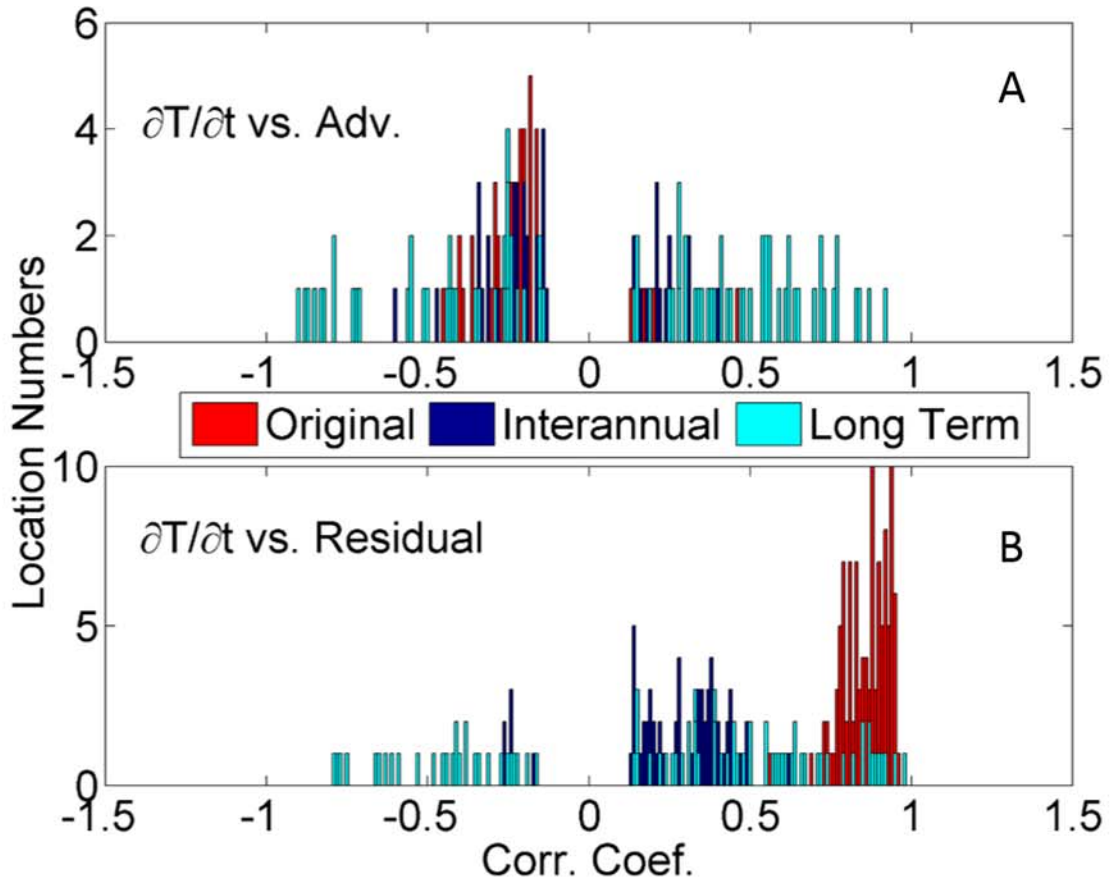


Figure 4.2. The histogram of the correlation coefficients. A. the correlation coefficients between the temporal variation term and the advection term. B. The correlation coefficients between the temporal variation term and the residual term. Non-significant correlations ( $p > 0.05$ ) are removed.

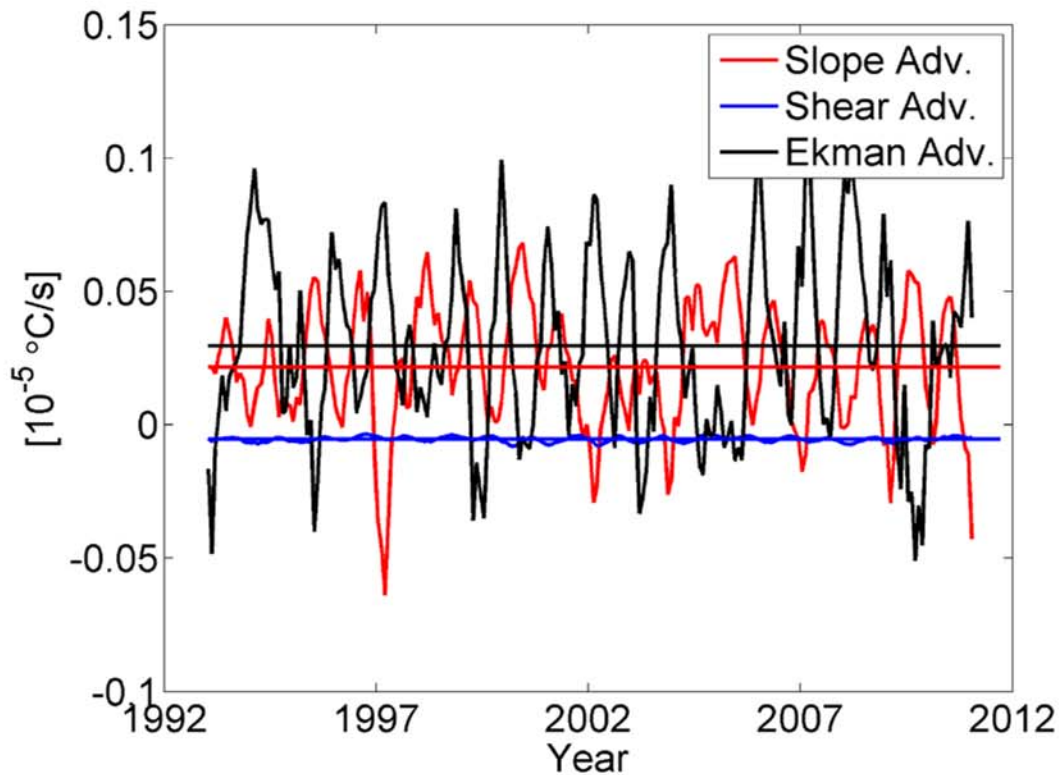
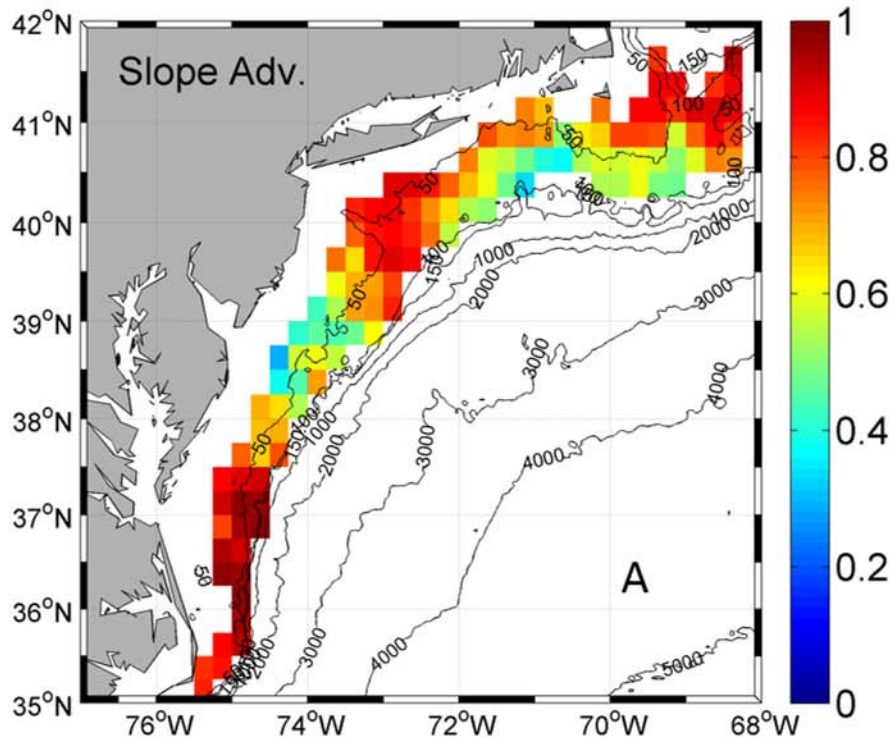
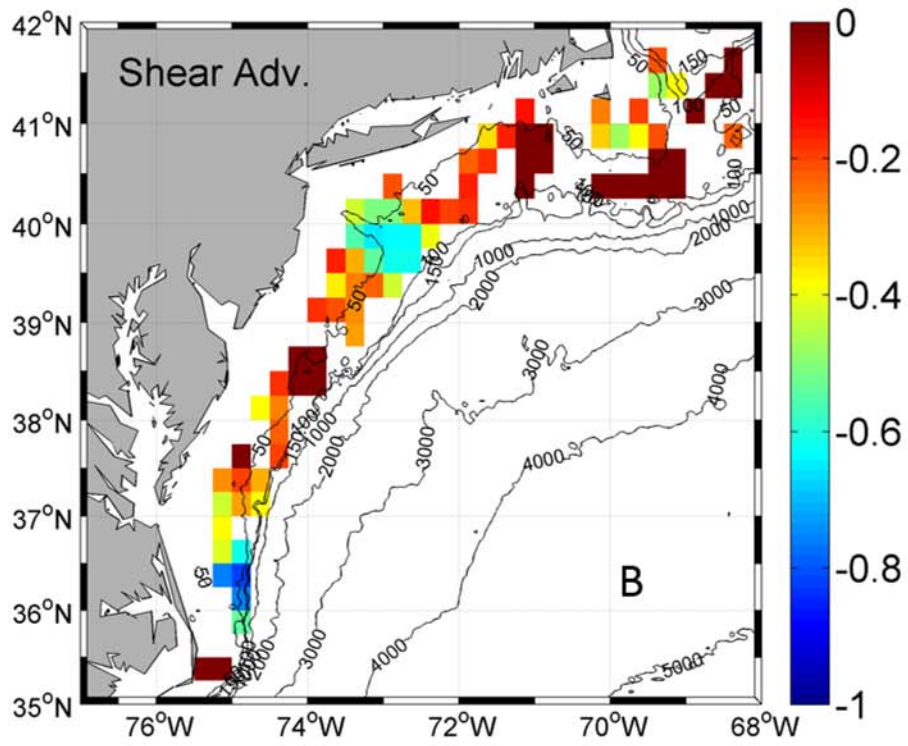


Figure 4.3. Each component of the advection term. The red line is the advection corresponding to the sea surface slope (slope advection). The blue line is the advection corresponding to the subsurface density gradient (Shear Advection). The black line is the advection due to wind-driven Ekman transport (Ekman Advection). The abnormal values of Ekman Advection, which are larger than 2 standard deviation, have been removed.





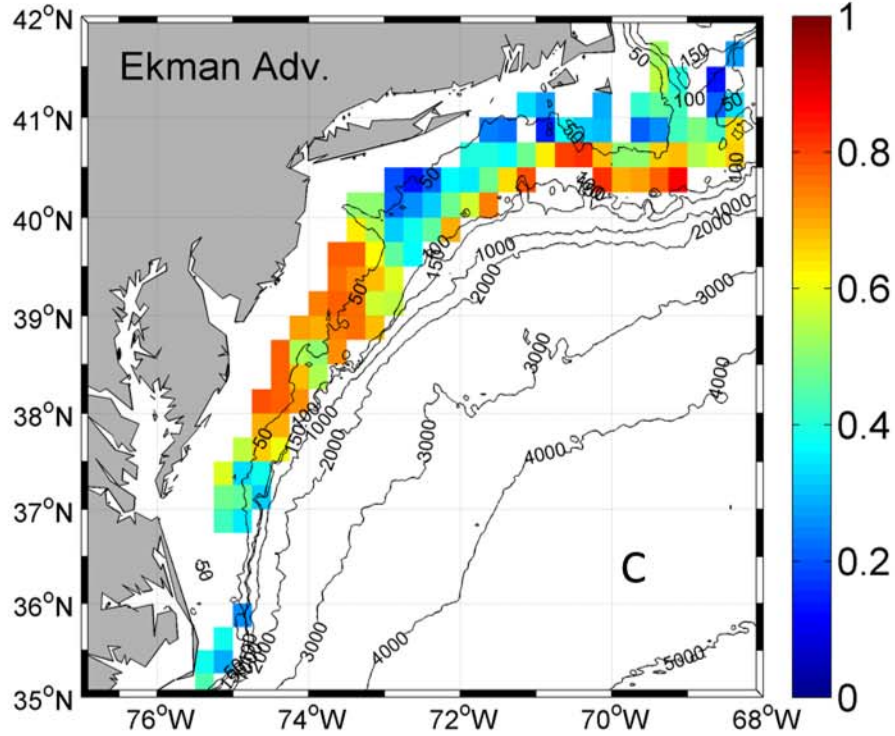


Figure 4.4. Comparison of the contribution in the upper ocean heat budget between the geostrophic currents and Ekman transport. A. the correlation coefficients between the composed advection and the slope advection. B. the correlation coefficients between the composed advection and the shear advection. C. the correlation coefficients between the composed advection and the Ekman advection. Those areas without significant correlation ( $p > 0.05$ ) are masked out in the figures.

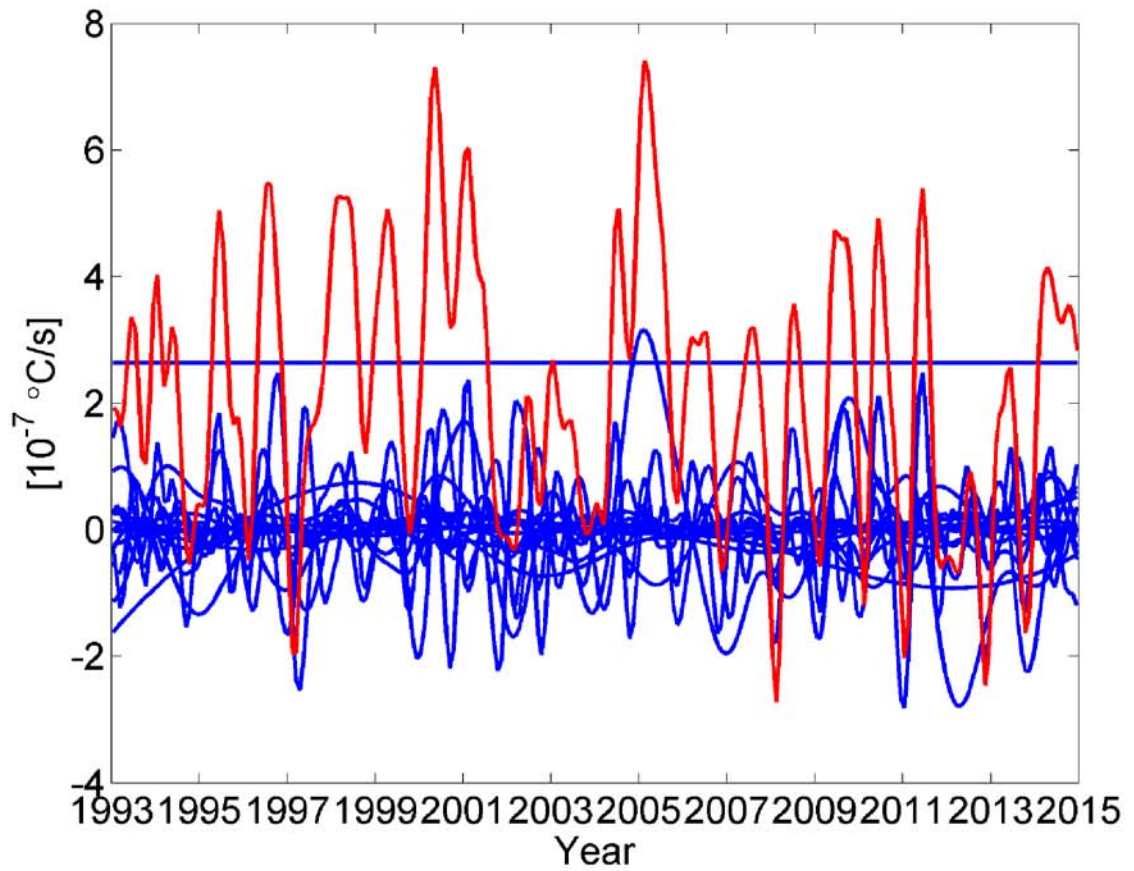
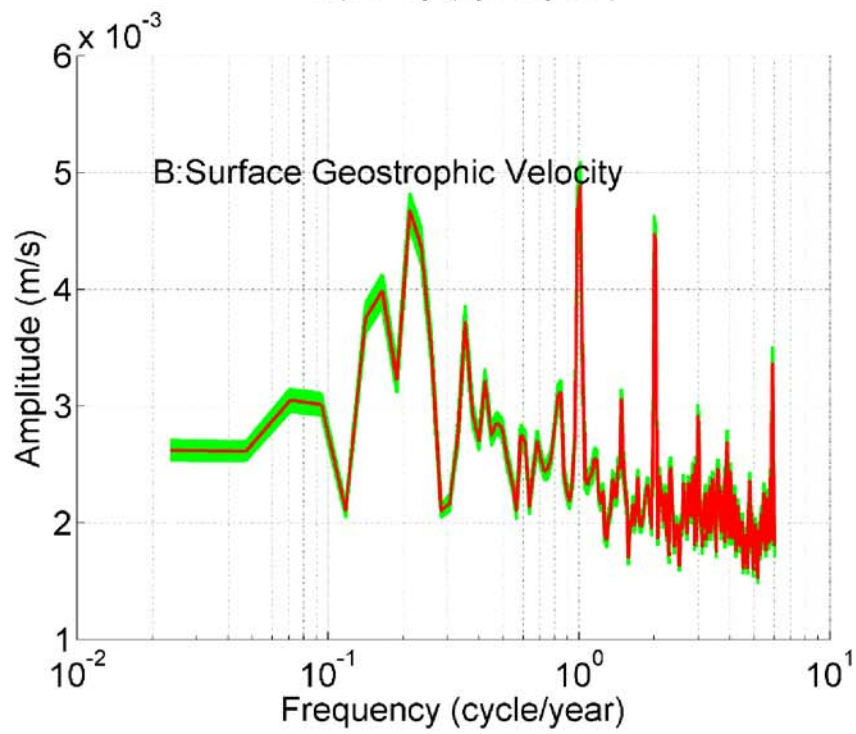
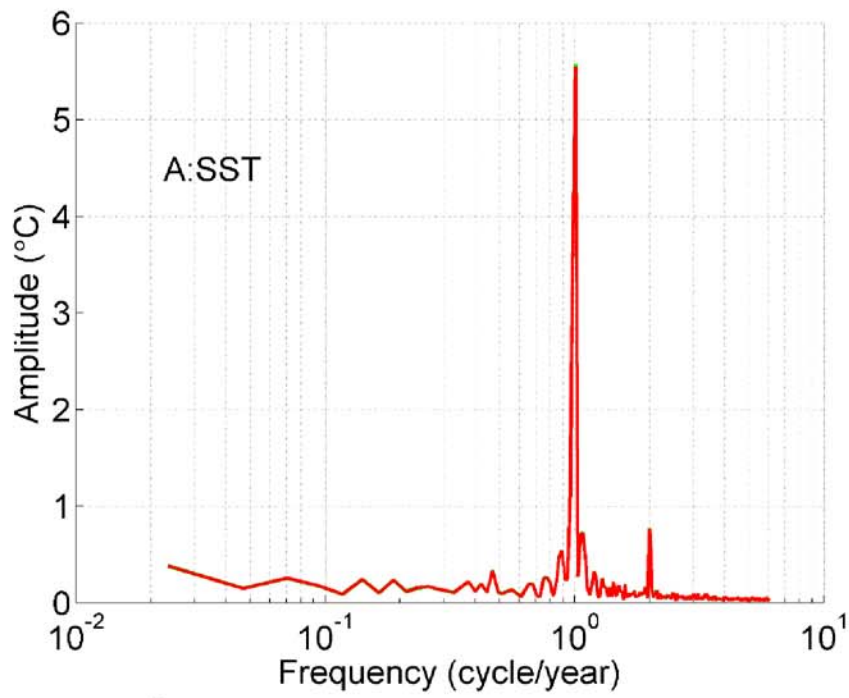


Figure 4.5. Comparison of the 16 (out of 25) advection temporal components. The blue lines are time series of the advection component (domain averaged). The red line is the sum of the components, computed using SST and absolute geostrophic currents. Components involving sub-seasonal and higher frequencies are not shown here.



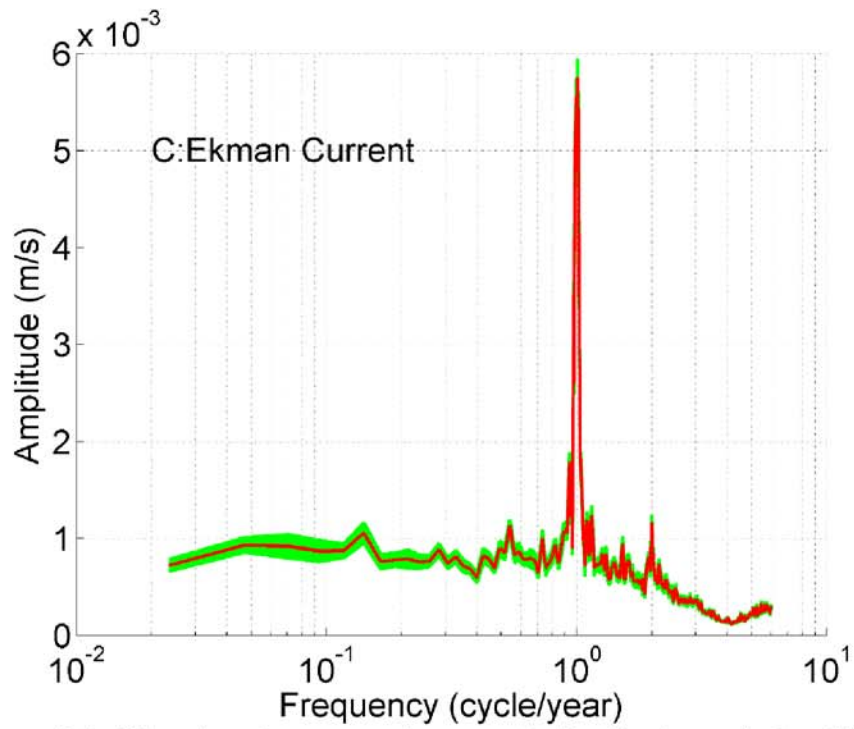
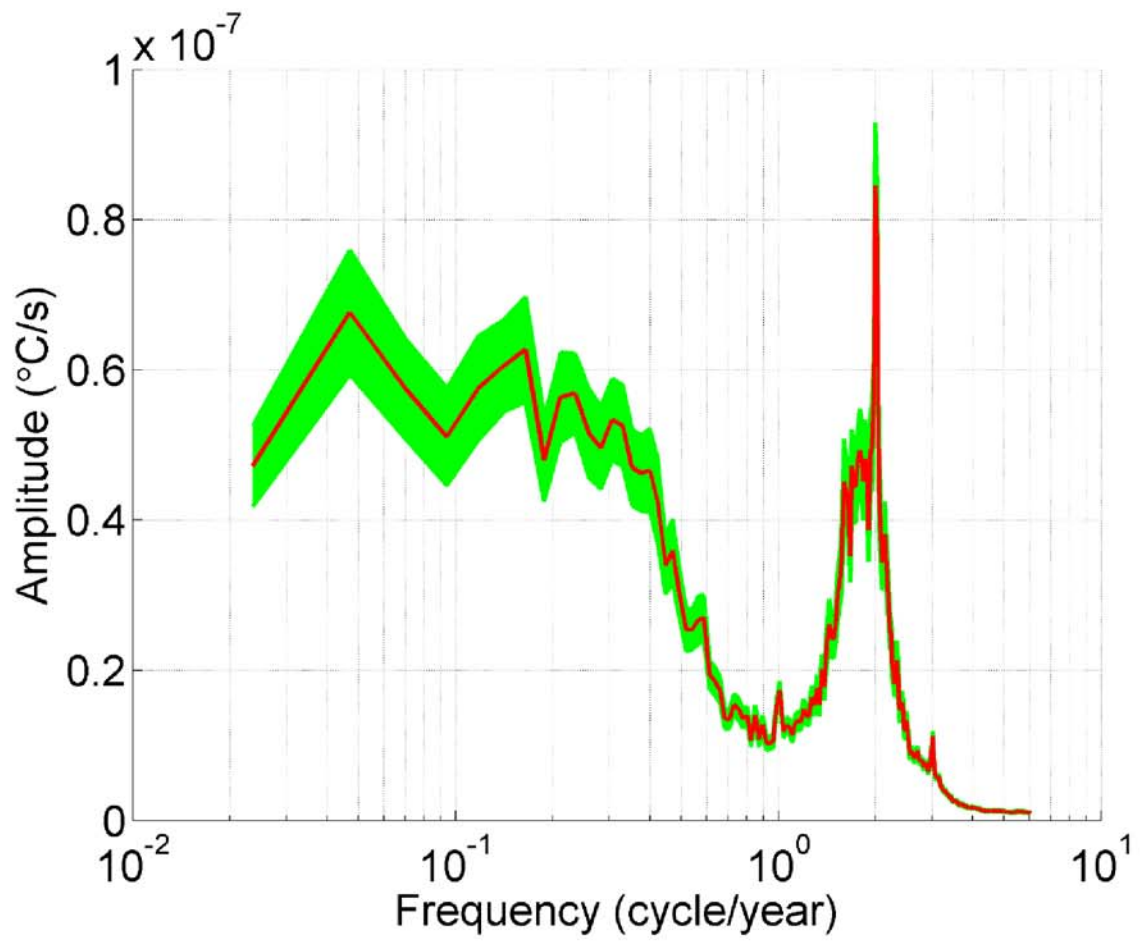


Figure 4.6. The domain-averaged spectral distribution of the SST (A), surface geostrophic current speed (B) and depth-averaged Ekman current speed (C). The green area represents the 95% confidence level of the mean. The mean of each variable has been removed.



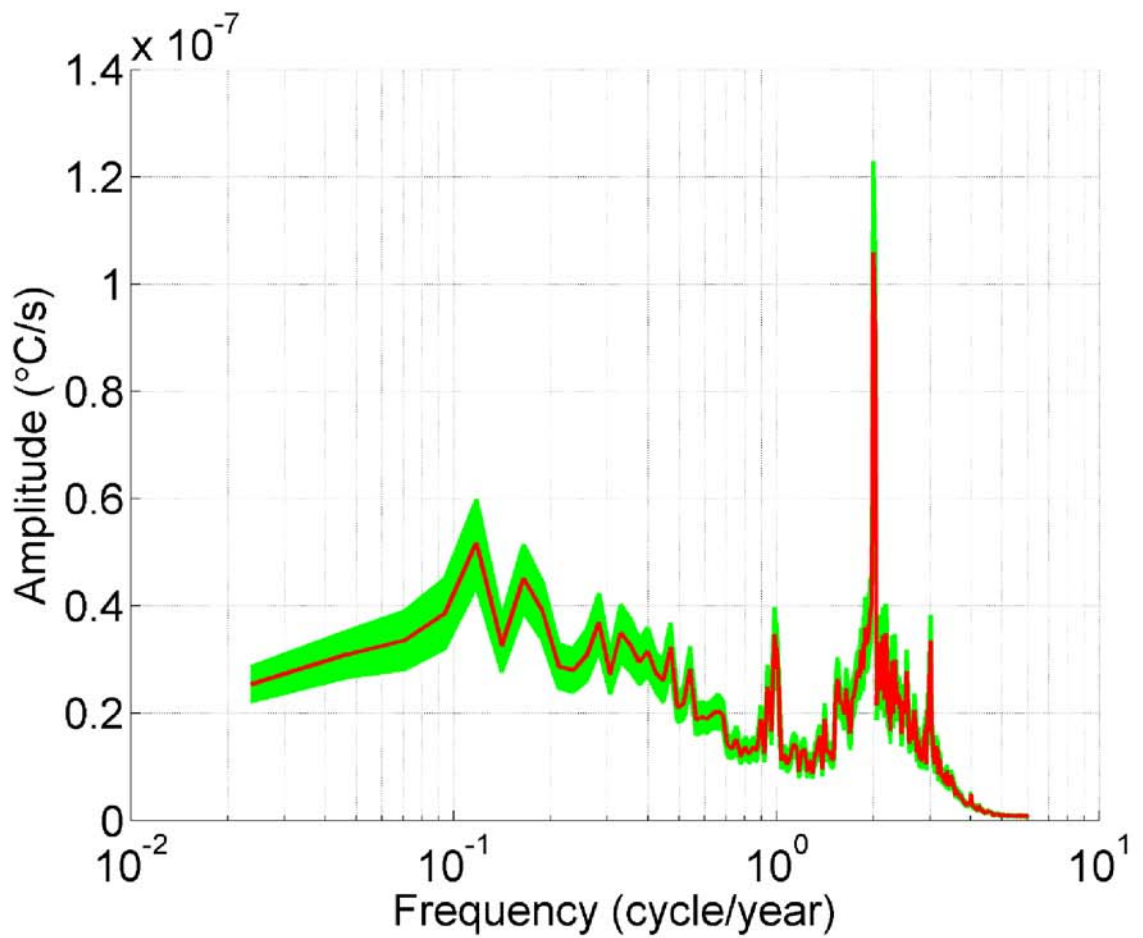


Figure 4.7. The spectral distribution of the advection. A. The advection from seasonal SST and seasonal surface geostrophic currents. B. The advection from seasonal SST and seasonal Ekman currents. The red line is the spatial mean averaging over the study area. The green area represents the 95% confidence level of the mean.

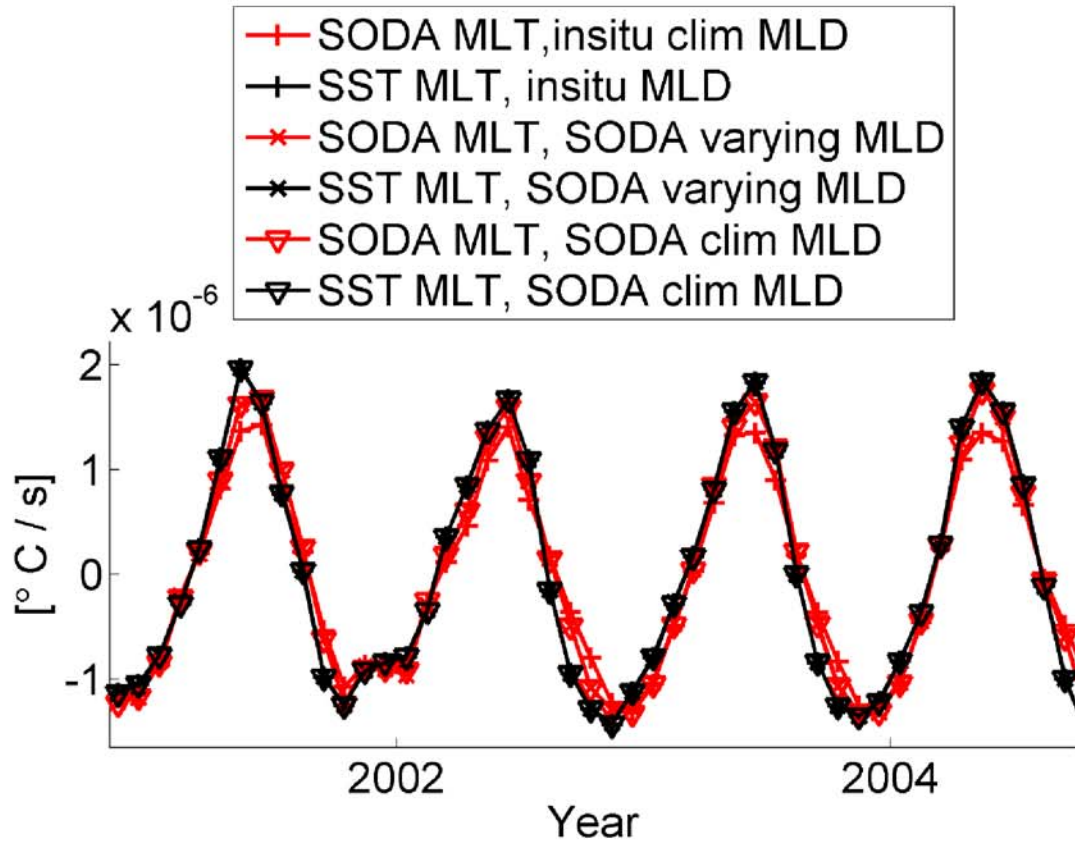


Figure 4.8. Cross-comparison of the temporal heat variation with different choice of MLD and MLT. The mixed layers are insitu monthly climatological MLD, SODA time-varying MLD and SODA monthly climatological MLD respectively. The MLTs are SST and SODA. Note this is the vertical mean thus the unit is  $^{\circ}\text{C}/\text{s}$ .

Table 4.1. The temporal decomposition of the horizontal heat advection associated with the surface geostrophic current. The percentages present the contribution of each component to the total energy.

		Surface Geostrophic Current					Row Sum
		Sub-seasonal	Seasonal	Interannual	Long Term	Mean	
SST	Sub-seasonal	1.3%	0.1%	0.2%	0.1%	1.3%	2.9%
	Seasonal	<b>38.8%</b>	3.7%	4.6%	1.4%	<b>27.0%</b>	75.5%
	Interannual	0.9%	0.1%	0.1%	0.0%	0.7%	1.8%
	Long Term	1.0%	0.1%	0.1%	0.1%	0.8%	2.2%
	Mean	<b>14.1%</b>	1.5%	1.6%	0.5%	0.0%	17.6%
	Column Sum	56.1%	5.5%	6.6%	2.1%	29.8%	

Table 4.2. The temporal decomposition of the horizontal heat advection associated with wind-induced Ekman currents. The percentages present the contribution of each component to the total energy.

		Ekman Currents					Row Sum
		Sub-seasonal	Seasonal	Interannual	Long Term	Mean	
SST	Sub-seasonal	0.1%	0.8%	0.2%	0.1%	0.6%	1.9%
	Seasonal	6.4%	<b>31.2%</b>	9.5%	3.4%	<b>34.4%</b>	84.9%
	Interannual	0.1%	0.7%	0.2%	0.1%	0.5%	1.5%
	Long Term	0.1%	0.5%	0.1%	0.0%	0.3%	1.0%
	Mean	1.3%	7.0%	1.8%	0.6%	0.0%	10.7%
	Column Sum	8.0%	40.2%	11.8%	4.2%	35.8%	

## **Chapter 5**

### **CONCLUSIONS**

The study in this dissertation focuses on several shelf processes in the Middle Atlantic Bight, using multi-sensor data including in-situ measurements, model reanalysis, and satellite observations. This work improves the understanding of how the ocean responds to processes on different time scales, facilitates better interpretation of the observations, and enables further investigations of the continental shelf using multi-sensor data. Specifically, I choose a phytoplankton bloom off the New Jersey as a study case to investigate the detailed roles of multiply factors involved in the evolution of blooms, on time scales of days to weeks in the inner shelf. For the middle and outer shelf, a linkage between the cross-shelf sea level variations and the subsurface cold pool is revealed on the seasonal scale. Moreover, the response of the heat advection to interactions of variables on different time scales are investigated. For each specific process, the detailed conclusions are listed as follows.

#### **5.1 Mechanisms of the Phytoplankton Blooms**

The diagnostic result of the 2011 summer bloom, which is basically the balance between the horizontal advection and the residual term (source/sink and vertical exchange), explains the bloom expansion process: the phytoplankton bloom grows where plenty of nutrients are supplied, and is transported along with currents. The local Chl concentration will keep relatively steady due to the replenishment of local source/sink/vertical exchange.

Different transport and nutrient delivery mechanisms are proposed and examined for sub-regions of the blooms. (1) The northern coastal section of the bloom experienced a high-low-high pattern in Chl time series. The first Chl peak is due to the upwelling along the New Jersey coast and the second Chl peak is the result of the clockwise eddy at the Long Island shore. The Hudson River outflow moving eastward encountered the strong coastal current moving westward and formed a clockwise eddy at the Long Island shore. The subsequent bloom is entrained by the coastal current flowing southward and merged into the southern bloom section. All these occur within the low-discharge condition of the Hudson River. (2) The southern coastal section of the bloom is supported by upwelling events in the southern New Jersey coast. Correlations between the sea surface currents and wind stress are mostly limited within the middle shelf of Area B, while wind induced currents are the dominant factor for the offshore bloom transport. (3) The northeast section of the bloom is fueled by nutrient source upwelled through Ekman pumping. The estimated Ekman pumping in this area has the same magnitude as the coastal upwelling, suggesting the Ekman pumping could also be one of the important nutrient supporting mechanisms.

The bloom conditions in all three sub-region occurred simultaneously, leading to the high Chl concentration in the summer of 2011. The proposed mechanisms could apply to most of bloom events from 2002 to 2013.

## **5.2 The Linkage between the Cross-Shelf Sea Level Variation and the Cold Pool**

This study investigated the relationship between the cross-shelf sea level variation and the cold pool in the Middle Atlantic Bight for the first time. The persistence of the cold pool water generates depressed thermal steric height in the middle shelf. Co-located depression features are found in the annual evolution of the

thermal steric height, total steric height and satellite observed SLA. The modulation of the sea level variations by the cold pool is revealed that the small variation induced by the cold pool overlies with the major seasonal cycle dominated by the solar heat flux. This study provides insights into the composition of the sea level variations on the continental shelf, and thus contributes to the understanding of the response of the sea level variations to mesoscale water masses on the continental shelf.

Temporally, the cold pool pattern is most apparent in July and August as a result of magnitude competition between the thermal and haline steric height. The annual variation of the haline steric height is much smaller than that of the thermal steric height but is of the same magnitude in the early summer. This explains why cold pool features forms from May (Figure 3.3A) but the middle shelf depressed height is found after June especially in August in SLA (Figure 3.5).

EEMD is applied to altimetry SLA to extract the annual cycle components so that the middle shelf depression can be found for single year's data without average. The locations of SLA depression are consistent with the in-situ cold core locations, suggesting the linkage between these two variables and a promising application of altimetry SLA to the cold pool study.

### **5.3 The Role and the Response of the Horizontal Heat Advection**

The role of the horizontal advection in the upper ocean heat budget over the MAB is quantitatively investigated. On seasonal scale the temperature variation is controlled by the vertical heat flux. On the longer time scales, it is the balance between the vertical heat flux and horizontal heat advection that determines the temperature variation.

The relative contributions of the geostrophic currents and the wind-induced Ekman transport are investigated at different locations. The wind-induced Ekman transport is as large as the surface geostrophic currents in the surface layer especially for the New Jersey shelf and the New England shelfbreak. When considering the whole water column, the wind's role will be the least comparing to the sloping sea surface and the density gradient.

The spectrum distribution of the temperature and the ocean currents determined the relative magnitudes of the advection temporal components. The relative magnitudes of temporal components are determined by the spectral distribution of the temperature and currents. Spectral analysis on the temporal components suggests that the variations of the horizontal heat advection on specific time scales are the combined contribution of multiply time scale variations. Through the investigation of the interactions among different temporal components, it is revealed that the variation of the horizontal heat advection is the combined contribution from multiply components of different time scales. This study improves our understanding of the response of advection to different temporal variability.

## REFERENCES

- Abraham, E.R., 1998. The generation of plankton patchiness by turbulent stirring. *Nature* 391, 577–580. doi:10.1038/35361
- Aikman III, F., Ou, H.W., Houghton, R.W., 1988. Current variability across the New England continental shelf-break and slope. *Cont. Shelf Res., Shelf Edge Exchange Processes of the Mid-Atlantic Bight* 8, 625–651. doi:10.1016/0278-4343(88)90069-6
- Andres, M., Gawarkiewicz, G.G., Toole, J.M., 2013. Interannual sea level variability in the western North Atlantic: Regional forcing and remote response. *Geophys. Res. Lett.* 40, 2013GL058013. doi:10.1002/2013GL058013
- Austin, J.A., 1999. The role of the alongshore wind stress in the heat budget of the North Carolina inner shelf. *J. Geophys. Res. Oceans* 104, 18187–18203. doi:10.1029/1998JC900122
- Bane, J.M., Brown, O.B., Evans, R.H., Hamilton, P., 1988. Gulf Stream remote forcing of shelfbreak currents in the Mid-Atlantic Bight. *Geophys. Res. Lett.* 15, 405–407. doi:10.1029/GL015i005p00405
- Beardsley, R.C., Boicourt, W.C., 1981. On estuarine and continental-shelf circulation in the Middle Atlantic Bight. *Evol. Phys. Oceanogr.* 198–233.
- Beardsley, R.C., Chapman, D.C., Brink, K.H., Ramp, S.R., Schlitz, R., 1985. The Nantucket Shoals Flux Experiment (NSFE79). Part I: A Basic Description of the Current and Temperature Variability. *J. Phys. Oceanogr.* 15, 713–748. doi:10.1175/1520-0485(1985)015<0713:TNSFEP>2.0.CO;2
- Beardsley, R.C., Lentz, S.J., Weller, R.A., Limeburner, R., Irish, J.D., Edson, J.B., 2003. Surface forcing on the southern flank of Georges Bank, February–August 1995. *J. Geophys. Res. Oceans* 108, 8007. doi:10.1029/2002JC001359
- Bigelow, H.B., 1933. *Studies of the waters on the continental shelf, Cape Cod to Chesapeake Bay. I. The cycle of temperature.*
- Bignami, F., Hopkins, T.S., 2003. Salt and heat trends in the shelf waters of the southern Middle-Atlantic Bight. *Cont. Shelf Res.* 23, 647–667. doi:10.1016/S0278-4343(03)00023-2
- Bingham, R.J., Hughes, C.W., 2012. Local diagnostics to estimate density-induced sea level variations over topography and along coastlines. *J. Geophys. Res. Oceans* 117, C01013. doi:10.1029/2011JC007276
- Bracco, A., Clayton, S., Pasquero, C., 2009. Horizontal advection, diffusion, and plankton spectra at the sea surface. *J. Geophys. Res. Oceans* 114, C02001. doi:10.1029/2007JC004671

- Bricelj, V.M., Kuenster, S., 1989. Effects of the “brown tide” on the feeding physiology and growth of bay scallops and mussels. *Coast. Estuar. Stud.* 35, 491–509.
- Buckley, M.W., Ponte, R.M., Forget, G., Heimbach, P., 2014. Low-Frequency SST and Upper-Ocean Heat Content Variability in the North Atlantic. *J. Clim.* 27, 4996–5018. doi:10.1175/JCLI-D-13-00316.1
- Burrage, D.M., Garvine, R.W., 1988. Summertime Hydrography at the Shelfbreak Front in the Middle Atlantic Bight. *J. Phys. Oceanogr.* 18, 1309–1319. doi:10.1175/1520-0485(1988)018<1309:SHATSF>2.0.CO;2
- Carton, J.A., Giese, B.S., Grodsky, S.A., 2005. Sea level rise and the warming of the oceans in the Simple Ocean Data Assimilation (SODA) ocean reanalysis. *J. Geophys. Res. Oceans* 110, C09006. doi:10.1029/2004JC002817
- Castelao, R., Glenn, S., Schofield, O., 2010. Temperature, salinity, and density variability in the central Middle Atlantic Bight. *J. Geophys. Res.* 115, C10005. doi:10.1029/2009JC006082
- Chant, R.J., Glenn, S., Kohut, J., 2004. Flow reversals during upwelling conditions on the New Jersey inner shelf. *J. Geophys. Res.* 109, C12S03. doi:10.1029/2003JC001941
- Chant, R.J., Glenn, S.M., Hunter, E., Kohut, J., Chen, R.F., Houghton, R.W., Bosch, J., Schofield, O., 2008. Bulge Formation of a Buoyant River Outflow. *J. Geophys. Res. Oceans* 113, n/a–n/a. doi:10.1029/2007JC004100
- Chant, R., Wilkin, J., Zhang, W., Choi, B.-J., Hunter, E., Castelao, R., Glenn, S., Jurisa, J., Schofield, O., Houghton, R., Kohut, J., Frazer, T., Moline, M., 2008. Dispersal of the Hudson River Plume in the New York Bight: Synthesis of Observational and Numerical Studies During LaTTE. *Oceanography* 21, 148–161.
- Chapman, D.C., Barth, J.A., Beardsley, R.C., Fairbanks, R.G., 1986. On the Continuity of Mean Flow between the Scotian Shelf and the Middle Atlantic Bight. *J. Phys. Oceanogr.* 16, 758–772. doi:10.1175/1520-0485(1986)016<0758:OTCOMF>2.0.CO;2
- Chapman, D.C., Beardsley, R.C., 1989. On the Origin of Shelf Water in the Middle Atlantic Bight. *J. Phys. Oceanogr.* 19, 384–391. doi:10.1175/1520-0485(1989)019<0384:OTOOSW>2.0.CO;2
- Cheney, 1994. TOPEX/POSEIDON: The 2-cm solution - Cheney - 2012 - Journal of Geophysical Research: Oceans (1978–2012) - Wiley Online Library. *J. Geophys. Res. Oceans.*
- Chen, X., Tung, K.-K., 2014. Varying planetary heat sink led to global-warming slowdown and acceleration. *Science* 345, 897–903. doi:10.1126/science.1254937
- Choi, B.-J., Wilkin, J.L., 2007. The Effect of Wind on the Dispersal of the Hudson River Plume. *J. Phys. Oceanogr.* 37, 1878–1897. doi:10.1175/JPO3081.1

- Christensen, M.K., Pringle, J.M., 2012. The frequency and cause of shallow winter mixed layers in the Gulf of Maine. *J. Geophys. Res. Oceans* 117, C01025. doi:10.1029/2011JC007358
- Churchill, J.H., Gawarkiewicz, G.G., 2014. Shelf water and chlorophyll export from the Hatteras slope and outer shelf. *J. Geophys. Res. Oceans* 119, 4291–4304. doi:10.1002/2014JC009809
- Clemente-Colon, P., Yan, X.-H., 1999. Observations of East Coast upwelling conditions in synthetic aperture radar imagery. *Geosci. Remote Sens. IEEE Trans. On* 37, 2239–2248.
- Cole, J.J., Caraco, N.F., 2006. Primary Production and Its Regulation in the Tidal-Freshwater Hudson River, in: *The Hudson River Estuary*. Cambridge University Press.
- Connolly, T.P., Lentz, S.J., 2014. Interannual variability of wintertime temperature on the inner continental shelf of the Middle Atlantic Bight. *J. Geophys. Res. Oceans* 119, 6269–6285. doi:10.1002/2014JC010153
- Csanady, G.T., 1997. On the theories that underlie our understanding of continental shelf circulation. *J. Oceanogr.* 53, 207–230.
- Csanady, G.T., 1982. *Circulation in the Coastal Ocean*. Springer Netherlands.
- Csanady, G.T., 1979. The pressure field along the western margin of the North Atlantic. *J. Geophys. Res. Oceans* 84, 4905–4915. doi:10.1029/JC084iC08p04905
- Csanady, G.T., Hamilton, P., 1988. Circulation of slope water. *Cont. Shelf Res., Shelf Edge Exchange Processes of the Mid-Atlantic Bight* 8, 565–624. doi:10.1016/0278-4343(88)90068-4
- Deser, C., Alexander, M.A., Timlin, M.S., 2003. Understanding the persistence of sea surface temperature anomalies in midlatitudes. *J. Clim.* 16, 57–72.
- Dong, S., Kelly, K.A., 2004. Heat Budget in the Gulf Stream Region: The Importance of Heat Storage and Advection. *J. Phys. Oceanogr.* 34, 1214–1231. doi:10.1175/1520-0485(2004)034<1214:HBITGS>2.0.CO;2
- Dong, S., Kelly, K.A., 2003. Seasonal and interannual variations in geostrophic velocity in the Middle Atlantic Bight. *J. Geophys. Res. Oceans* 108, 3172. doi:10.1029/2002JC001357
- Dzwonkowski, B., 2009. *Surface Current Analysis of Shelf Water in the Central Mid-Atlantic Bight*. University of Delaware, Newark, DE.
- Dzwonkowski, B., Kohut, J.T., Yan, X.-H., 2009. Seasonal differences in wind-driven across-shelf forcing and response relationships in the shelf surface layer of the central Mid-Atlantic Bight. *J. Geophys. Res.* 114, C08018. doi:10.1029/2008JC004888
- Dzwonkowski, B., Lipphardt Jr., B.L., Kohut, J.T., Yan, X.-H., Garvine, R.W., 2010. Synoptic measurements of episodic offshore flow events in the central mid-Atlantic Bight. *Cont. Shelf Res.* 30, 1373–1386.
- Ekman, V.W., 1905. On the influence of the earth's rotation on ocean-currents. *Ark. För Mat. Astron. Och Fys. Bd 2 No 11*.

- Fairbanks, R.G., 1982. The origin of continental shelf and slope water in the New York Bight and Gulf of Maine: Evidence from H<sub>2</sub>18O/H<sub>2</sub>16O ratio measurements. *J. Geophys. Res. Oceans* 87, 5796–5808. doi:10.1029/JC087iC08p05796
- Feng, J., Wu, Z., Liu, G., 2014. Fast Multidimensional Ensemble Empirical Mode Decomposition Using a Data Compression Technique. *J. Clim.* 27, 3492–3504. doi:10.1175/JCLI-D-13-00746.1
- Fewings, M.R., 2007. Cross-shelf circulation and momentum and heat balances over the inner continental shelf near Martha's Vineyard, Massachusetts. Massachusetts Institute of Technology.
- Fewings, M.R., Lentz, S.J., 2011. Summertime cooling of the shallow continental shelf. *J. Geophys. Res. Oceans* 116, C07015. doi:10.1029/2010JC006744
- Figley, W., Pyle, B., Halgren, B., 1976. Socioeconomic impacts. *Oxyg. Deplet. Assoc. Benthic Mortalities N. Y. Bight* 315–322.
- Forsyth, J., Andres, M., Gawarkiewicz, G. g., 2015. Recent accelerated warming of the continental shelf off New Jersey: Observations from the CMV Oleander XBT line. *J. Geophys. Res. Oceans* n/a–n/a. doi:10.1002/2014JC010516
- Frazer, T.K., Keller, S.R., Schofield, O., Glenn, S.M., Kohut, J., Chant, R.J., Oliver, M., Reinfelder, J.R., Moline, M.A., Zhou, M., Chen, R.F., 2006. Coastal Ocean Observatories Enable Biological Investigations in a Buoyant Plume. Presented at the OCEANS 2006, pp. 1–6.
- Fu, L.-L., Davidson, R.A., 1995. A note on the barotropic response of sea level to time-dependent wind forcing. *J. Geophys. Res. Oceans* 100, 24955–24963. doi:10.1029/95JC02259
- Gill, A.E., 1968. Similarity theory and geostrophic adjustment. *Q. J. R. Meteorol. Soc.* 94, 586–588. doi:10.1002/qj.49709440214
- Gill, A.E., Niller, P.P., 1973. The theory of the seasonal variability in the ocean. *Deep Sea Res. Oceanogr. Abstr.* 20, 141–177. doi:10.1016/0011-7471(73)90049-1
- Glenn, S., Arnone, R., Bergmann, T., Bissett, W.P., Crowley, M., Cullen, J., Gryzmski, J., Haidvogel, D., Kohut, J., Moline, M., Oliver, M., Orrico, C., Sherrell, R., Song, T., Weidemann, A., Chant, R., Schofield, O., 2004. Biogeochemical impact of summertime coastal upwelling on the New Jersey Shelf. *J. Geophys. Res.* 109, C12S02. doi:10.1029/2003JC002265
- Glenn, S.M., Crowley, M.F., Haidvogel, D.B., Song, Y.T., 1996. Underwater observatory captures coastal upwelling events off New Jersey. *Eos TransAGU* 77, 233–236. doi:10.1029/96EO00161
- Glenn, S., Schofield, O., Chant, R., Kohut, J., Roarty, H., Bosch, J., Bowers, L., Gong, D., Kerfoot, J., 2007. Wind-driven response of the Hudson River Plume and its effect on dissolved oxygen concentrations. *Environ. Res. Eng. Manag.* 1, 14–18.
- Gong, D., Kohut, J.T., Glenn, S.M., 2010. Seasonal climatology of wind-driven circulation on the New Jersey Shelf. *J. Geophys. Res. Oceans* 115, C04006. doi:10.1029/2009JC005520

- Gordon, A.L., Aikman III, F., 1981. Salinity maximum in the pycnocline of the Middle Atlantic Bight. *Limnol Ocean.* 26, 123–130.
- Grodsky, S.A., Carton, J.A., Liu, H., 2008. Comparison of bulk sea surface and mixed layer temperatures. *J. Geophys. Res.* 113. doi:10.1029/2008JC004871
- Gulev, S.K., Latif, M., Keenlyside, N., Park, W., Koltermann, K.P., 2013. North Atlantic Ocean control on surface heat flux on multidecadal timescales. *Nature* 499, 464–467. doi:10.1038/nature12268
- Halliwell, G.R., 1998. Simulation of North Atlantic Decadal/Multidecadal Winter SST Anomalies Driven by Basin-Scale Atmospheric Circulation Anomalies. *J. Phys. Oceanogr.* 28, 5–21. doi:10.1175/1520-0485(1998)028<0005:SONADM>2.0.CO;2
- Han, G., 2005. Wind-driven barotropic circulation off Newfoundland and Labrador. *Cont. Shelf Res.* 25, 2084–2106. doi:10.1016/j.csr.2005.04.015
- Han, G., Chen, N., Ma, Z., 2014. Is there a north-south phase shift in the surface Labrador Current transport on the interannual-to-decadal scale? *J. Geophys. Res. Oceans* 119, 276–287. doi:10.1002/2013JC009102
- Han, G., Ohashi, K., Chen, N., Myers, P.G., Nunes, N., Fischer, J., 2010. Decline and partial rebound of the Labrador Current 1993–2004: Monitoring ocean currents from altimetric and conductivity-temperature-depth data. *J. Geophys. Res. Oceans* 115, n/a–n/a. doi:10.1029/2009JC006091
- Han, G., Tang, C.L., 2001. Interannual variations of volume transport in the western Labrador Sea based on TOPEX/Poseidon and WOCE data. *J. Phys. Oceanogr.* 31, 199–211.
- Helland-Hansen, B., 1934. The Sognefjord section: Oceanographic Observations in the northernmost part of the North Sea and the southern part of the Norwegian Sea, in: James Johnstone Memorial Volume. Liverpool University Press, Liverpool, U.K., pp. 257–274.
- He, R., Chen, K., Fennel, K., Gawarkiewicz, G.G., D. J. McGillicuddy Jr., 2011a. Seasonal and interannual variability of physical and biological dynamics at the Shelfbreak Front of the Middle Atlantic Bight: nutrient supply mechanisms. *Biogeosciences Discuss.* 8, 1555–1590. doi:10.5194/bgd-8-1555-2011
- He, R., Chen, K., Fennel, K., Gawarkiewicz, G.G., McGillicuddy Jr, D.J., 2011b. Seasonal and interannual variability of physical and biological dynamics at the shelfbreak front of the Middle Atlantic Bight: nutrient supply mechanisms. *Biogeosciences* 8, 2935–2946. doi:10.5194/bg-8-2935-2011
- He, R., Weisberg, R.H., 2003. West Florida shelf circulation and temperature budget for the 1998 fall transition. *Cont. Shelf Res.* 23, 777–800. doi:10.1016/S0278-4343(03)00028-1
- He, R., Weisberg, R.H., 2002. West Florida shelf circulation and temperature budget for the 1999 spring transition. *Cont. Shelf Res.* 22, 719–748. doi:10.1016/S0278-4343(01)00085-1

- Hoagland, P., Scatista, S., 2006. The economic effects of harmful algal blooms, in: Graneli, E., Turner, J.T. (Eds.), *Ecological Studies 189: Ecology of Harmful Algae*. Springer-Verlag, Berlin., pp. 391–402.
- Houghton, R.W., Schlitz, R., Beardsley, R.C., Butman, B., Chamberlin, J.L., 1982. The Middle Atlantic Bight Cold Pool: Evolution of the Temperature Structure During Summer 1979. *J. Phys. Oceanogr.* 12, 1019–1029. doi:10.1175/1520-0485(1982)012<1019:TMABCP>2.0.CO;2
- Houghton, R.W., Visbeck, M., 1998. Upwelling and convergence in the Middle Atlantic Bight Shelfbreak Front. *Geophys. Res. Lett.* 25, 2765–2768. doi:10.1029/98GL02105
- Howarth, R.W., Levinton, J.S., 2006. Wastewater and Watershed Influences on Primary Productivity and Oxygen Dynamics in the Lower Hudson River Estuary; *The Hudson River Estuary*. publisherNameCambridge University Press.
- Howarth, R.W., Swaney, D.P., Butler, T.J., Marino, R., 2000. Climatic Control on Eutrophication of the Hudson River Estuary. *Ecosystems* 3, 210–215.
- Huang, N.E., Shen, Z., Long, S.R., Wu, M.C., Shih, H.H., Zheng, Q., Yen, N.-C., Tung, C.C., Liu, H.H., 1998. The empirical mode decomposition and the Hilbert spectrum for nonlinear and non-stationary time series analysis. *Proc. R. Soc. Lond. Ser. Math. Phys. Eng. Sci.* 454, 903–995. doi:10.1098/rspa.1998.0193
- Ienna, F., Jo, Y.-H., Yan, X.-H., 2014. A New Method for Tracking Meddies by Satellite Altimetry. *J. Atmospheric Ocean. Technol.* 31, 1434–1445. doi:10.1175/JTECH-D-13-00080.1
- Jiang, L., 2008. A comprehensive study on coastal upwelling using observations, models and proxies.
- Jiang, L., Breaker, L.C., Yan, X.-H., 2010. A model for estimating cross-shore surface transport with application to the New Jersey Shelf. *J. Geophys. Res.* 115, C04017. doi:10.1029/2009JC005998
- Kaplan, D.M., Largier, J., 2006. HF radar-derived origin and destination of surface waters off Bodega Bay, California. *Deep Sea Res. Part II Top. Stud. Oceanogr.* 53, 2906–2930. doi:10.1016/j.dsr2.2006.07.012
- Ketchum, B.H., Corwin, N., 1964. THE PERSISTENCE OF “WINTER” WATER ON THE CONTINENTAL SHELF SOUTH OF LONG ISLAND, NEW YORK’. *LIMNOLOGY* 9.
- Klemas, V., Yan, X.-H., 2014. Subsurface and deeper ocean remote sensing from satellites: An overview and new results. *Prog. Oceanogr.* 122, 1–9. doi:10.1016/j.pocean.2013.11.010
- Kohut, J., Roarty, H., Randall-Goodwin, E., Glenn, S., Lichtenwalner, C.S., 2012. Evaluation of two algorithms for a network of coastal HF radars in the Mid-Atlantic Bight. *Ocean Dyn.* 62, 953–968. doi:10.1007/s10236-012-0533-9
- Kohut, J.T., Glenn, S.M., Chant, R.J., 2004. Seasonal current variability on the New Jersey inner shelf. *J. Geophys. Res.* 109, C07S07. doi:10.1029/2003JC001963

- Kohut, J.T., Roarty, H.J., Glenn, S.M., 2006. Characterizing Observed Environmental Variability With HF Doppler Radar Surface Current Mappers and Acoustic Doppler Current Profilers: Environmental Variability in the Coastal Ocean. *IEEE J. Ocean. Eng.* 31, 876–884. doi:10.1109/JOE.2006.886095
- Kushnir, Y., 1994. Interdecadal Variations in North Atlantic Sea Surface Temperature and Associated Atmospheric Conditions. *J. Clim.* 7, 141–157. doi:10.1175/1520-0442(1994)007<0141:IVINAS>2.0.CO;2
- Lee, Y.J., Lwiza, K., 2005. Interannual variability of temperature and salinity in shallow water: Long Island Sound, New York. *J. Geophys. Res. Oceans* 110, C09022. doi:10.1029/2004JC002507
- Lentz, S., 2004. The Response of Buoyant Coastal Plumes to Upwelling-Favorable Winds\*. *J. Phys. Oceanogr.* 34, 2458–2469. doi:10.1175/JPO2647.1
- Lentz, S., 2001. The Influence of Stratification on the Wind-Driven Cross-Shelf Circulation over the North Carolina Shelf\*. *J. Phys. Oceanogr.* 31, 2749–2760. doi:10.1175/1520-0485(2001)031<2749:TIOSOT>2.0.CO;2
- Lentz, S.J., 2009. The Mean Along-Isobath Heat and Salt Balances over the Middle Atlantic Bight Continental Shelf. *J. Phys. Oceanogr.* 40, 934–948. doi:10.1175/2009JPO4214.1
- Lentz, S.J., 2008a. Observations and a Model of the Mean Circulation over the Middle Atlantic Bight Continental Shelf. *J. Phys. Oceanogr.* 38, 1203–1221. doi:10.1175/2007JPO3768.1
- Lentz, S.J., 2008b. Seasonal Variations in the Circulation over the Middle Atlantic Bight Continental Shelf. *J. Phys. Oceanogr.* 38, 1486–1500. doi:10.1175/2007JPO3767.1
- Lentz, S.J., 2003. A climatology of salty intrusions over the continental shelf from Georges Bank to Cape Hatteras. *J. Geophys. Res.* 108. doi:10.1029/2003JC001859
- Lentz, S.J., Butman, B., Harris, C., 2014. The vertical structure of the circulation and dynamics in Hudson Shelf Valley. *J. Geophys. Res. Oceans* 119, 3694–3713. doi:10.1002/2014JC009883
- Lentz, S.J., Shearman, R.K., Plueddemann, A.J., 2010. Heat and salt balances over the New England continental shelf, August 1996 to June 1997. *J. Geophys. Res.* 115. doi:10.1029/2009JC006073
- Levitus, S., Antonov, J.I., Boyer, T.P., Baranova, O.K., Garcia, H.E., Locarnini, R.A., Mishonov, A.V., Reagan, J.R., Seidov, D., Yarosh, E.S., Zweng, M.M., 2012. World ocean heat content and thermosteric sea level change (0–2000 m), 1955–2010. *Geophys. Res. Lett.* 39, L10603. doi:10.1029/2012GL051106
- Li, Y., Ji, R., Fratantoni, P.S., Chen, C., Hare, J.A., Davis, C.S., Beardsley, R.C., 2014. Wind-induced interannual variability of sea level slope, along-shelf flow, and surface salinity on the Northwest Atlantic shelf. *J. Geophys. Res. Oceans* 119, 2462–2479. doi:10.1002/2013JC009385
- Macías, D., Franks, P.J.S., Ohman, M.D., Landry, M.R., 2012. Modeling the effects of coastal wind- and wind-stress curl-driven upwellings on plankton dynamics in

- the Southern California current system. *J. Mar. Syst.* 94, 107–119. doi:10.1016/j.jmarsys.2011.11.011
- Malone, T.C., Hopkins, T.S., Falkowski, P.G., Whitedge, T.E., 1983. Production and transport of phytoplankton biomass over the continental shelf of the new york bight. *Cont. Shelf Res.* 1, 305–337. doi:10.1016/0278-4343(83)90001-8
- Marra, J., Houghton, R.W., Garside, C., 1990. Phytoplankton growth at the shelf-break front in the Middle Atlantic Bight. *J. Mar. Res.* 48, 851–868.
- Moline, M.A., Blackwell, S.M., Chant, R., Oliver, M.J., Bergmann, T., Glenn, S., Schofield, O.M.E., 2004. Episodic physical forcing and the structure of phytoplankton communities in the coastal waters of New Jersey. *J. Geophys. Res. Oceans* 109, n/a–n/a. doi:10.1029/2003JC001985
- Moline, M., Frazer, T., Chant, R., Glenn, S., Jacoby, C., Reinfelder, J., Yost, J., Zhou, M., Schofield, O., 2008. Biological Responses in a Dynamic Buoyant River Plume. *Oceanography* 21, 70–89. doi:10.5670/oceanog.2008.06
- Mountain, D.G., 2003. Variability in the properties of Shelf Water in the Middle Atlantic Bight, 1977–1999. *J. Geophys. Res. Oceans* 108, n/a–n/a. doi:10.1029/2001JC001044
- Mountain, D.G., Strout, G.A., Beardsley, R.C., 1996. Surface heat flux in the Gulf of Maine. *Deep Sea Res. Part II Top. Stud. Oceanogr.* 43, 1533–1546. doi:10.1016/S0967-0645(96)00057-4
- Narváez, D.A., Munroe, D.M., Hofmann, E.E., Klinck, J.M., Powell, E.N., Mann, R., Curchitser, E., 2014. Long-term dynamics in Atlantic surfclam (*Spisula solidissima*) populations: The role of bottom water temperature. *J. Mar. Syst.* doi:10.1016/j.jmarsys.2014.08.007
- Oliver, M.J., Schofield, O., Bergmann, T., Glenn, S., Orrico, C., Moline, M., 2004. Deriving in situ phytoplankton absorption for bio-optical productivity models in turbid waters. *J. Geophys. Res. Oceans* 109, C07S11. doi:10.1029/2002JC001627
- Pickett, M.H., 2003. Ekman transport and pumping in the California Current based on the U.S. Navy’s high-resolution atmospheric model (COAMPS). *J. Geophys. Res.* 108. doi:10.1029/2003JC001902
- Reynolds, R.W., Smith, T.M., Liu, C., Chelton, D.B., Casey, K.S., Schlax, M.G., 2007. Daily High-Resolution-Blended Analyses for Sea Surface Temperature. *J. Clim.* 20, 5473–5496. doi:10.1175/2007JCLI1824.1
- Roarty, H., Glenn, S., Kohut, J., Gong, D., Handel, E., Rivera, E., Garner, T., Atkinson, L., Brown, W., Jakubiak, C., others, 2010. Operation and application of a regional high-frequency radar network in the Mid-Atlantic Bight. *Mar. Technol. Soc. J.* 44, 133–145.
- Ryan, J.P., Yoder, J.A., Barth, J.A., Cornillon, P.C., 1999. Chlorophyll enhancement and mixing associated with meanders of the shelf break front in the Mid-Atlantic Bight. *J. Geophys. Res. Oceans* 104, 23479–23493. doi:10.1029/1999JC900174

- Sanders, T.M., Garvine, R.W., 2001. Fresh water delivery to the continental shelf and subsequent mixing: An observational study. *J. Geophys. Res. Oceans* 106, 27087–27101. doi:10.1029/2001JC000802
- Schofield, O., Chant, R., Cahill, B., Castelao, R., Gong, D., Kahl, A., Kohut, J., Montes-Hugo, M., Ramadurai, R., Ramey, P., Yi, X., Glenn, S., 2008. The Decadal View of the Mid-Atlantic Bight from the COOLroom: Is Our Coastal System Changing? *Oceanography* 21, 108–117. doi:10.5670/oceanog.2008.08
- Schofield, O., Moline, M., Cahill, B., Frazer, T., Kahl, A., Oliver, M., Reinfelder, J., Glenn, S., Chant, R., 2013. Phytoplankton productivity in a turbid buoyant coastal plume. *Cont. Shelf Res.* 63, S138–S148. doi:10.1016/j.csr.2013.02.005
- Sha, J., Jo, Y.-H., Oliver, M.J., Kohut, J.T., Shatley, M., Liu, W.T., Yan, X.-H., 2015. A case study of large phytoplankton blooms off the New Jersey coast with multi-sensor observations. *Cont. Shelf Res.* 107, 79–91. doi:10.1016/j.csr.2015.07.006
- Shearman, R.K., Lentz, S.J., 2009. Long-Term Sea Surface Temperature Variability along the U.S. East Coast. *J. Phys. Oceanogr.* 40, 1004–1017. doi:10.1175/2009JPO4300.1
- Sheng, J., Thompson, K.R., 1996. A robust method for diagnosing regional shelf circulation from scattered density profiles. *J. Geophys. Res. Oceans* 101, 25647–25659. doi:10.1029/96JC01331
- Siegel, D.A., Doney, S.C., Yoder, J.A., 2002. The North Atlantic Spring Phytoplankton Bloom and Sverdrup’s Critical Depth Hypothesis. *Science* 296, 730–733.
- Smagorinsky, J., 1963. General circulation experiments with the primitive equations. *Mon. Weather Rev.* 91, 99–164. doi:10.1175/1520-0493(1963)091<0099:GCEWTP>2.3.CO;2
- Smith, R.L., 1968. Upwelling. *Oceanogr. Mar. Biol. Annu. Rev.* 6, 11–46.
- Smith, S.D., 1988. Coefficients for Sea Surface Wind Stress, Heat Flux, and Wind Profiles as a Function of Wind Speed and Temperature. *J. Geophys. Res.* 93, 15467–15472. doi:10.1029/JC093iC12p15467
- Song, Y.T., Haidvogel, D.B., Glenn, S.M., 2001. Effects of topographic variability on the formation of upwelling centers off New Jersey: A theoretical model. *J. Geophys. Res.* 106, 9223–9240. doi:10.1029/2000JC000244
- Stammer, D., 1997. Steric and wind-induced changes in TOPEX/POSEIDON large-scale sea surface topography observations. *J. Geophys. Res. Oceans* 102, 20987–21009. doi:10.1029/97JC01475
- Stoddard, A., O’Reilly, J., Whitley, T., Malone, T., Hebard, J., 1986. The Application and Development of a Compatible Historical Data Base for the Analysis of Water Quality Management Issues in the New York Bight. Presented at the OCEANS ’86, pp. 1030–1035.
- Sullivan, M.C., Cowen, R.K., Steves, B.P., 2005. Evidence for atmosphere–ocean forcing of yellowtail flounder (*Limanda ferruginea*) recruitment in the Middle

- Atlantic Bight. *Fish. Oceanogr.* 14, 386–399. doi:10.1111/j.1365-2419.2005.00343.x
- Ullman, D.S., O'Donnell, J., Kohut, J., Fake, T., Allen, A., 2006. Trajectory prediction using HF radar surface currents: Monte Carlo simulations of prediction uncertainties. *J. Geophys. Res.* 111. doi:10.1029/2006JC003715
- Vivier, F., Kelly, K.A., Thompson, L., 1999. Contributions of wind forcing, waves, and surface heating to sea surface height observations in the Pacific Ocean. *J. Geophys. Res. Oceans* 104, 20767–20788. doi:10.1029/1999JC900096
- Warsh, C., 1987. NOAA's Northeast Monitoring Program (NEMP): A report on progress of the first five years (1979-84) and a plan for the future, in: NOAA Tech. Memo. NMFS-F/NEC-44. National Oceanic and Atmospheric Administration, National Marine Fisheries Service, Northeast Fisheries Center, pp. 9–20.
- Wilkin, J.L., 2006. The Summertime Heat Budget and Circulation of Southeast New England Shelf Waters. *J. Phys. Oceanogr.* 36, 1997–2011. doi:10.1175/JPO2968.1
- Winant, C.D., Dorman, C.E., 1997. Seasonal patterns of surface wind stress and heat flux over the Southern California Bight. *J. Geophys. Res. Oceans* 102, 5641–5653. doi:10.1029/96JC02801
- Wood, A.M., Sherry, N.D., Huyer, A., 1996. Mixing of chlorophyll from the Middle Atlantic Bight cold pool into the Gulf Stream at Cape Hatteras in July 1993.
- Wu, Z., Huang, N.E., 2009. ENSEMBLE EMPIRICAL MODE DECOMPOSITION: A NOISE-ASSISTED DATA ANALYSIS METHOD. *Adv. Adapt. Data Anal.* 01, 1–41. doi:10.1142/S1793536909000047
- Wu, Z., Huang, N.E., Chen, X., 2009. THE MULTI-DIMENSIONAL ENSEMBLE EMPIRICAL MODE DECOMPOSITION METHOD. *Adv. Adapt. Data Anal.* 01, 339–372. doi:10.1142/S1793536909000187
- Xu, F.-H., Oey, L.-Y., 2011. The Origin of Along-Shelf Pressure Gradient in the Middle Atlantic Bight. *J. Phys. Oceanogr.* 41, 1720–1740. doi:10.1175/2011JPO4589.1
- Xu, Y., Chant, R., Gong, D., Castelao, R., Glenn, S., Schofield, O., 2011. Seasonal variability of chlorophyll a in the Mid-Atlantic Bight. *Cont. Shelf Res.* 31, 1640–1650.
- Yankovsky, A.E., Chapman, D.C., 1997. A Simple Theory for the Fate of Buoyant Coastal Discharges\*. *J. Phys. Oceanogr.* 27, 1386–1401. doi:10.1175/1520-0485(1997)027<1386:ASTFTF>2.0.CO;2
- Yankovsky, A.E., Garvine, R.W., 1998. Subinertial Dynamics on the Inner New Jersey Shelf during the Upwelling Season. *J. Phys. Oceanogr.* 28, 2444–2458. doi:10.1175/1520-0485(1998)028<2444:SDOTIN>2.0.CO;2
- Yan, X.-H., Jo, Y.-H., Liu, W.T., He, M.-X., 2006. A New Study of the Mediterranean Outflow, Air–Sea Interactions, and Meddies Using Multisensor Data. *J. Phys. Oceanogr.* 36, 691–710. doi:10.1175/JPO2873.1

- Yan, X.-H., Pan, J., Jo, Y.-H., He, M.-X., Liu, W.T., Jiang, L., 2004. Role of winds in estimation of ocean heat storage anomaly using satellite data. *J. Geophys. Res. Oceans* 109, n/a–n/a. doi:10.1029/2003JC002202
- Yeh, J.-R., Shieh, J.-S., Huang, N.E., 2010. Complementary ensemble empirical mode decomposition: a novel noise enhanced data analysis method. *Adv. Adapt. Data Anal.* 02, 135–156. doi:10.1142/S1793536910000422
- Yoder, J.A., Schollaert, S.E., O'Reilly, J.E., 2002. Climatological Phytoplankton Chlorophyll and Sea Surface Temperature Patterns in Continental Shelf and Slope Waters off the Northeast U.S. Coast. *Limnol. Oceanogr.* 47, 672–682.
- Zhang, C., Hu, C., Shang, S., Müller-Karger, F.E., Li, Y., Dai, M., Huang, B., Ning, X., Hong, H., 2006. Bridging between SeaWiFS and MODIS for continuity of chlorophyll-a concentration assessments off Southeastern China. *Remote Sens. Environ.* 102, 250–263. doi:10.1016/j.rse.2006.02.015
- Zhang, H.-M., Bates, J.J., Reynolds, R.W., 2006. Assessment of composite global sampling: Sea surface wind speed. *Geophys. Res. Lett.* 33, L17714. doi:10.1029/2006GL027086
- Zhang, W.G., Wilkin, J.L., Chant, R.J., 2009. Modeling the Pathways and Mean Dynamics of River Plume Dispersal in the New York Bight. *J. Phys. Oceanogr.* 39, 1167–1183. doi:10.1175/2008JPO4082.1
- Zhang, W.G., Wilkin, J.L., Schofield, O.M.E., 2010. Simulation of Water Age and Residence Time in New York Bight. *J. Phys. Oceanogr.* 40, 965–982. doi:10.1175/2009JPO4249.1

## Appendixes

### PERMISSIONS FROM JOURNAL OF GEOPHYSICAL RESEARCH: OCEANS

This Agreement between Jin Sha ("You") and John Wiley and Sons ("John Wiley and Sons") consists of your license details and the terms and conditions

License Number	3738250695647
License date	Oct 29, 2015
Licensed Content Publisher	John Wiley and Sons
Licensed Content Publication	Journal of Geophysical Research: Oceans
Licensed Content Title	The modulation of the seasonal cross-shelf sea level variation by the cold pool in the Middle Atlantic Bight
Licensed Content Author	Jin Sha, Young-Heon Jo, Xiao-Hai Yan, W. T. Liu
Licensed Content Date	Oct 15, 2015
Pages	1
Type of use	Dissertation/Thesis
Requestor type	Author of this Wiley article
Format	Electronic
Portion	Full article
Will you be translating?	No
Title of your thesis / dissertation	A study of oceanic responses to mesoscale processes in the Middle Atlantic Bight
Expected completion date	Oct 2015
Expected size (number of pages)	130
Requestor Location	Jin Sha

215 Robinson Hall

NEWARK, DE 19716

United States

Attn: Jin Sha

Billing Type

Invoice

Jin Sha

215 Robinson Hall

Billing Address

NEWARK, DE 19716

United States

Attn: Jin Sha

Total

0.00 USD

## PERMISSIONS FROM CONTINENTAL SHELF RESEARCH

### ELSEVIER LICENSE TERMS AND CONDITIONS

Oct 29, 2015

This is a License Agreement between Jin Sha ("You") and Elsevier ("Elsevier") provided by Copyright Clearance Center ("CCC"). The license consists of your order details, the terms and conditions provided by Elsevier, and the payment terms and conditions.

Supplier	Elsevier Limited The Boulevard, Langford Lane Kidlington, Oxford, OX5 1GB, UK
Registered Company Number	1982084
Customer name	Jin Sha
Customer address	215 Robinson Hall NEWARK, DE 19716
License number	3738260230384
License date	Oct 29, 2015
Licensed content publisher	Elsevier
Licensed content publication	Continental Shelf Research
Licensed content title	A case study of large phytoplankton blooms off the New Jersey coast with multi-sensor observations
Licensed content author	Jin Sha, Young-Heon Jo, Matthew J. Oliver, Josh T. Kohut, Matthew Shatley, W. Timothy Liu, Xiao-Hai Yan
Licensed content date	15 September 2015
Licensed content volume number	107
Licensed content issue number	n/a
Number of pages	13
Start Page	79
End Page	91

Type of Use	reuse in a thesis/dissertation
Intended publisher of new work	other
Portion	full article
Format	electronic
Are you the author of this Elsevier article?	Yes
Will you be translating?	No
Title of your thesis/dissertation	A study of oceanic responses to mesoscale processes in the Middle Atlantic Bight
Expected completion date	Oct 2015
Estimated size (number of pages)	130
Elsevier VAT number	GB 494 6272 12
Permissions price	0.00 USD
VAT/Local Sales Tax	0.00 USD / 0.00 GBP
Total	0.00 USD